

---

Electronic Thesis and Dissertation Repository

---

10-26-2022 10:00 AM

# A Fast Voxel-based 3D Dose Convolution Method for Personalized Targeted Radionuclide Therapy of Prostate Cancer Patients

Chidera Opara, *The University of Western Ontario*

Supervisor: Lee, Ting Yim, *The University of Western Ontario*

Co-Supervisor: Hajdok, George, *The University of Western Ontario*

A thesis submitted in partial fulfillment of the requirements for the Master of Science degree in Medical Biophysics

© Chidera Opara 2022

Follow this and additional works at: <https://ir.lib.uwo.ca/etd>



Part of the [Medicine and Health Sciences Commons](#)

---

## Recommended Citation

Opara, Chidera, "A Fast Voxel-based 3D Dose Convolution Method for Personalized Targeted Radionuclide Therapy of Prostate Cancer Patients" (2022). *Electronic Thesis and Dissertation Repository*. 8972. <https://ir.lib.uwo.ca/etd/8972>

This Dissertation/Thesis is brought to you for free and open access by Scholarship@Western. It has been accepted for inclusion in Electronic Thesis and Dissertation Repository by an authorized administrator of Scholarship@Western. For more information, please contact [wlsadmin@uwo.ca](mailto:wlsadmin@uwo.ca).

# Abstract

Targeted radionuclide therapy (TRT) is an effective treatment for metastatic prostate cancer. This thesis develops a convolution-based dosimetric method for TRT and validates its performance against a Monte Carlo (MC) simulation method, `egs_mird`, developed in our laboratory.

The research completed includes: 1) validating `egs_mird` by generating dose point kernels (DPKs) for  $^{90}\text{Y}$ ,  $^{131}\text{I}$  and  $^{177}\text{Lu}$  and comparing them with MCNP4C, PENELOPE and GEANT4 DPK in literature, and 2) comparing TRT dosimetry of prostate cancer patients obtained using the convolution method and `egs_mird`.

`egs_mird` DPKs for  $^{90}\text{Y}$  and  $^{131}\text{I}$  agreed with those from other MC codes. The discrepancy between  $^{177}\text{Lu}$  DPK and literature was due to differences in emission spectra used in the MC simulation. The mean doses in the prostate and critical organs as evaluated by the convolution method were 5-7% lower than `egs_mird` due to density inhomogeneities.

## Keywords

Dose Point Kernel (DPK), 3D Dose Convolution, Monte Carlo Simulation, Targeted Radionuclide Therapy (TRT), Prostate Cancer, [ $^{177}\text{Lu}$ ]PSMA-617, Time-Integrated Activity (TIA), Patient-specific, Dosimetry, Positron Emission Tomography (PET), Computed Tomography (CT), Fluorodeoxyglucose (FDG), Flourocholine (FCH), Prostate-Specific Membrane Antigen (PSMA), `egs_mird`, EGSnrc, [ $^{18}\text{F}$ ]DCFPyL

## Lay Abstract

Prostate cancer (PCa) is the most commonly diagnosed cancer in men and the second leading cause of cancer-related deaths in Canada. Besides standard treatment methods such as surgery, hormone therapy, and chemotherapy, targeted radionuclide therapy (TRT) is a newer effective method to treat PCa that has spread to other parts of the body. TRT is a form of “internal” radiotherapy where the radiation is guided to the tumor by molecules that specifically target cancer cells. As in radiotherapy TRT requires an accurate calculation of the radiation dose to the tumor and surrounding healthy tissues to maximize the success of killing the tumor and minimize the chances of complications. Current TRT dose calculation uses a whole tumor/organ approach which is not accurate. The more accurate approach, called Monte Carlo simulation, requires a long calculation time so it is not practicable in clinical use. This thesis develops a new dose calculation method, called 3D convolution, which is faster and has similar accuracy as the MC simulation method.

The accuracy of the 3D convolution method was first tested in the idealized situation of calculating the dose in a material of the same density surrounding a radiation source. The 3D convolution results agreed with those obtained with MC simulation. Then dose calculations in PCa patients were compared. The mean dose in the prostate and healthy organs as evaluated by the 3D convolution method was 5-7% lower than the MC simulation. The likely explanation for this discrepancy is that MC simulation is able to account for density variations within the human body whereas the 3D convolution method assumes no density variations.

## Co-Authorship Statement

Chapter one and two. I did the literature review, wrote the first draft of the chapters, and revised the chapters with comments and suggested changes from my supervisors.

Chapter three was the validation of the in-house Monte Carlo (MC) simulation code, `egs_mird`. I designed the tests with help from my supervisors and Dr. Martin Martinov who wrote the MC code. The test involving comparing `egs_mird` DPKs with those from literature was included in the manuscript “Fast beta-emitter Monte Carlo simulations and full patient dose calculations of targeted radionuclide therapy: introducing `egs_mird`”. Published in *Medical Physics*. Published online July 15, 2022. doi:10.1002/mp.15786. I interpreted the results of the tests and wrote the first draft of this chapter and revised the chapter under the guidance of my supervisors.

Chapter four compares the dose distributions of prostate cancer patients calculated by the convolution method and `egs_mird`. The patient studies were from an archived database generated by the clinical trial (NCT04009174) on men with untreated, biopsy-proven, localized prostate cancer. The study protocol was approved by the institutional Research Ethics Board. I analyzed the studies to obtain the required information for dose calculations as described in this Chapter. I interpreted the results of the dose comparisons and wrote the first draft of this chapter and revised the chapter under the guidance of my supervisors.

## Acknowledgments

My thesis would not have been possible without the direct and indirect guidance and support of many individuals.

First and foremost, I am highly and forever indebted to my supervisors, Dr. Ting-Yim Lee and Dr. George Hajdok for their profound support and guidance throughout my study. The sacrifice of your time in meetings and conversations were vital in inspiring me and challenging my mind. You taught me how to interpret results with cautious optimism, communicate effectively and think critically, which have made me a better scientist. It was indeed a privilege to work with you.

This endeavor would not be possible without my advisory committee members, Dr. Rowan Thomson, Dr. Stewart Gaede, and Dr. Martin Martinov. Thank you for your guidance and the value of your expertise invested in me during this research. It was wonderful to have you as my advisory committee member. My experience with Monte Carlo and its applications would have been limited without Dr. Martin Martinov's input. I'm indeed grateful.

Thanks to my lab members, Dr. Xiaogang Chen, Kevin Jaeyoung Chung, Heather Young, Danny De Sarno, Olivia Tong, Dr Thanh Tai Duong and Anne Leaist for the insightful discussions and for making my time at Robarts enjoyable. To Heather Young, thank you for helping me with image segmentation and mentorship. Words cannot express my gratitude to Anne Leaist. Thank you for your profound help with all the administrative work in the lab. You made my graduate career so much easier by helping me to focus on my research.

To the Medical Biophysics graduate chair, Dr. Charles Alexander McKenzie, I am grateful for your mentorship and support. Thanks to Kathleen Petts and Elizabeth Oliveira for helping me with administrative work in the department. Thanks to Dr. Udunna Anazodo and Dr Francis Fezeu for their mentorship and support.

Most importantly, I thank my family and friends. To my mom and siblings, thank you for your constant love, encouragement and support during challenging times. Lastly, I thank God Almighty for always being with me.

# Table of Contents

Abstract.....	ii
Lay Abstract.....	iii
Co-Authorship Statement.....	iv
Acknowledgments.....	v
Table of Contents.....	vi
List of Tables.....	x
List of Figures.....	xii
List of Abbreviations.....	xvi
List of Appendices.....	xviii
Chapter 1.....	1
1 Introduction.....	1
1.1 Prostate Cancer Epidemiology.....	1
1.2 Mechanism.....	2
1.3 Prostate Cancer Symptoms, Screening and Diagnosis.....	3
1.4 Prostate Cancer Staging and Grading.....	4
1.5 Prostate Cancer Imaging Modalities.....	8
1.5.1 Computed Tomography.....	8
1.5.2 Multiparametric MRI.....	9
1.5.3 Positron Emission Tomography/Computed Tomography.....	10
1.5.4 PET/MRI.....	11
1.6 Prostate Cancer Treatment Modalities.....	11
1.6.1 Local Treatment Options.....	11
1.6.2 Systemic Treatment Options.....	13
1.7 Targeted Radionuclide Therapy.....	14

1.7.1	Targeted Radionuclide Therapy: Overview .....	15
1.7.2	Targeted Radionuclide Therapy Radionuclides, Carrier Molecules and Tumor Targeting .....	18
1.7.3	Targeted Radionuclide Therapy for Prostate Cancer .....	19
1.7.4	TRT for Prostate Cancer: Current Limitations and Possible Solutions ....	22
Chapter 2 .....		27
2	Dose Calculation Methods in Targeted Radionuclide Therapy .....	27
2.1	Approaches to Dosimetry in Targeted Radionuclide Therapy .....	27
2.2	Definition: Absorbed Dose .....	28
2.3	Dose Calculation Method .....	29
2.3.1	Organ S-value Dosimetry .....	29
2.3.2	Dose Point Kernel Convolution .....	31
2.3.3	Full Monte Carlo Simulation .....	32
2.3.4	Quantification of Time-Integrated Activity from PET/SPECT Images ...	36
2.4	Thesis Objectives and Outline .....	39
2.4.1	Chapter 3: egs_mird MC code validation .....	39
2.4.2	Chapter 4: Three-dimensional Voxel-level Dose Point Kernel Convolution Code .....	40
2.4.3	Chapter 5: Conclusion and Future Direction .....	40
Chapter 3 .....		41
3	egs_mird Validation .....	41
3.1	egs_mird Monte Carlo Code .....	41
3.1.1	egs_mird Monte Carlo Code .....	41
3.2	Methods .....	46
3.2.1	Internal Consistency Test .....	46
3.2.2	External Consistency Test .....	48
3.3	Results .....	49

3.3.1	Internal Consistency Test.....	49
3.3.2	External Consistency Test.....	52
3.4	Discussion.....	54
3.5	Conclusion .....	56
Chapter 4.....		57
4	Three-Dimensional Voxel-Level Dose Point Convolution Code .....	57
4.1	Motivation.....	57
4.2	Methods.....	58
4.2.1	Dynamic PET and CT Study.....	58
4.2.2	Conversion of PET and CT Data for DPK Convolution and Monte Carlo Simulation.....	59
4.2.3	Absorbed Dose Calculation Comparison between Analytical Calculation, DPK Convolution and Monte Carlo Simulation.....	61
4.2.4	Patient-Specific 3D Dose Convolution and Monte Carlo Simulation .....	62
4.3	Results.....	64
4.3.1	Absorbed Dose Comparison between Analytical Calculation, DPK Convolution and Monte Carlo Simulation.....	64
4.3.2	Patient-Specific 3D Dose Convolution and Monte Carlo Simulation .....	67
4.4	Discussion.....	86
4.5	Conclusion .....	89
Chapter 5.....		90
5	Conclusion and Future Directions.....	90
5.1	Summary.....	90
5.2	DPK Convolution Density Correction .....	91
5.3	Estimation of Biological Effective Dose .....	92
5.4	Estimation of Time-Integrated Activity.....	93
5.4.1	Exponential Extrapolation .....	94



5.4.2 From Kinetic Modelling .....	94
References .....	96
Appendices .....	116
Curriculum Vitae .....	124

## List of Tables

Table 1.1: Prostate cancer stage grouping by TNM classification. <sup>38-42</sup> .....	5
Table 1.2: The Gleason grading system for prostate cancer. <sup>38-42</sup> .....	7
Table 1.3: Prostate cancer stage groups. <sup>38-42</sup> Abbreviations: T – Primary tumor; N -Regional lymph node; M – Distant metastasis; PSA - Prostate-specific antigen; G - Gleason group. ....	7
Table 1.4: List of TRT clinical trials for the treatment of different neuroendocrine tumors..	17
Table 1.5: List of radionuclides used in targeted radionuclide therapy, their half-life, particle energy, maximum particle energy, and penetration range in tissue. <sup>94,118-121</sup> .....	19
Table 1.6: List of radiolabeled ligands used for PSMA targeting in targeted radionuclide therapy for prostate cancer.....	21
Table 1.7: List of clinical trials for the treatment of prostate cancer. ....	25
Table 3.1: Cristy and Eckermann's elemental composition. <sup>237</sup> .....	48
Table 3.2: Energy deposition profile of <sup>177</sup> Lu in volumes of different sizes as estimated from DPK of 1 mm and 2 mm voxel resolution. ....	50
Table 3.3: egs_mird Monte Carlo simulation using 1 mm and 2 mm voxel resolution of total energy deposition from a <sup>177</sup> Lu radionuclide source. For comparison, energy deposited for a simulation with no transport is also included. ....	51
Table 3.4: Simulations of total energy deposition of monoenergetic 120 keV and 500 keV photon and monoenergetic 500 keV electron in (65 cm) <sup>3</sup> and (100 cm) <sup>3</sup> phantom sizes. ....	51
Table 3.5: Theoretical calculation to estimate the absorbed dose from electron capture and Auger electron not considered in vxIPen MC simulation of the decay of <sup>177</sup> Lu radionuclide source. ....	56
Table 4.1: The media assignment scheme used to assign the media described in Table 4.2 to different structures defined for the patient CT.....	60

Table 4.2: The density and atomic composition of all elements used in this work with their accompanying source in the literature. DPK Tissue also includes trace amounts of Mg, Si, Fe, Zn, Rb, Zr, and Pb not listed on the table. .... 60

Table 4.3: Average area under the DVH curve for the prostate and other organs at risk like the rectum, and bone marrow for the different dose calculation methods..... 74

Table 4.4: Total dose under the DVH curve for the prostate and other organs at risk like the rectum, and bone marrow. .... 79

Table 4.5: Area under the DVH curve for the prostate and other organs at risk like the rectum, and bone marrow for the different dose calculation methods..... 85

## List of Figures

Figure 1.1: An illustration of the different Gleason grades. (Reprinted with permission from Macmillan Publishers Ltd: Modern Pathology <sup>43</sup> , copyright (2004).).....	6
Figure 2.1: (A) DPK formalism and (B) Voxel S value formalism in the distribution of energy from radionuclide.....	31
Figure 2.2: Time-integrated activity quantification workflow .....	37
Figure 3.1: Schematic diagram of DPK phantom. The source, <sup>177</sup> Lu radionuclide source was positioned at the center voxel. The DPK phantom was filled with prostate media with a density of 1.03 g/cm <sup>3</sup> . .....	47
Figure 3.2: <sup>177</sup> Lu DPKs generated with eggs_mird for 1 mm (in blue) and 2 mm (in red) voxel resolution.....	50
Figure 3.3: Comparison of <sup>90</sup> Y DPKs generated using eggs_mird (black circle) to other DPKs from the literature. ....	53
Figure 3.4: Comparison of <sup>131</sup> I DPKs generated using eggs_mird (black circle) to other DPKs from the literature. ....	53
Figure 3.5: Comparison of <sup>177</sup> Lu DPKs generated using eggs_mird (black circle) to other DPKs from the literature. A magnified scale of the DPK profile at the center voxel is shown. ....	54
Figure 4.1: 3D Fast Fourier Transform dose convolution workflow.....	63
Figure 4.2: Dose point kernel (DK) of a radionuclide source emitting a 500 keV monoenergetic electron plotted along the x-(green), y-(blue) and z-axis (pink) for no radiation transport. The profiles along the x- and the y-axis overlap completely. ....	65
Figure 4.3: Dose profiles of the absorbed dose distributions in a phantom containing a 500 keV monoenergetic electron source at a uniform voxel TIA of 1 Bq.s calculated by DPK convolution and noVR MC with no radiation transport. ....	65

Figure 4.4: DPK with radiation transport of a 500 keV monoenergetic electron source plotted along the x-(green), y-(blue) and z-axis (pink). ..... 66

Figure 4.5: Dose profiles of the absorbed dose distributions in a phantom containing a 500 keV monoenergetic electron source at a uniform voxel TIA of 1 Bq.s calculated by DPK convolution and noVR MC with radiation transport. .... 67

Figure 4.6: A cross-sectional slice from the [<sup>18</sup>F]DCFPyL PET/CT study of a patient (IGPC-02-036) showing (a) media assignment, (b) density map, and TIA map for (c) full activity and (d) noCalc denoting no activity in calcifications. .... 68

Figure 4.7: Dose map from simulated <sup>177</sup>Lu TRT of the same cross-sectional slice as Figure 4.7. in  $U = \mu\text{Gy} \cdot \text{GBq}^{-1} \cdot \text{s}^{-1}$  units. The dose maps were computed using DPK convolution (top) and noVR egs\_mird simulation (middle), an egs\_mird simulation with tracklength scoring (bottom). The left and right images show dose maps with (full) and without (noCalc) activity in the calcifications, respectively. A magnified image of the prostate is shown for each dose map. .... 69

Figure 4.8: X- and Y-dose profile of the density corrected DPK convolution (red) and noVR MC (blue) dose maps calculated using full activity TIA in calcifications of Figure 4.8 are shown here. The DPK simulation-derived uncertainties were convolved with the time-integrated activity to generate error bars on the DPK plot while noVR uncertainties were derived from MC simulation. The black arrows point to calcified regions. .... 70

Figure 4.9: (A) X-dose profile of the density corrected DPK convolution (red) and noVR MC (blue) dose maps with no activity in calcifications. (B) Y-dose profile of the same dose maps as (A). (C) X-dose profiles of density corrected DPK convolution maps with full (blue) and no (red) activity in the calcifications. (D) Y-dose profiles of the same dose maps as in (C). The black arrows point to calcifications with no assumed activity in them. .... 71

Figure 4.10: Comparison of (A) X- and (B) Y-dose profiles in DPK convolution dose maps with (blue) and without (red) density correction. The maps were generated with full activity in the calcifications. The black arrows point to the calcified region. .... 72

Figure 4.11: Dose-volume histograms derived from dose distribution calculated with density corrected DPK convolution calculations, noVR MC and TL MC using TIA matrices with full and no activity in calcifications for (A) prostate, (B) bladder, (C) rectum, and (D) bone marrow. .... 73

Figure 4.12: Organ-level absorbed doses estimated using DPK convolution with and without density correction compared to noVR MC. .... 74

Figure 4.13: A cross-sectional slice from the [<sup>18</sup>F]-DCFPyL PET/CT study of a patient without calcifications in the prostate showing (a) media assignment, (b) density map, and (c) TIA map. .... 75

Figure 4.14: Dose maps of a patient without calcification in the prostate from simulated <sup>177</sup>Lu TRT. The maps were computed using DPK convolution (left) and noVR egs\_mird simulation (middle), an egs\_mird simulation with tracklength scoring (right). A magnified image of the prostate is shown for each dose map. Dose values are expressed in units of  $U = \mu\text{Gy} \cdot \text{GBq}^{-1} \cdot \text{s}^{-1}$ . .... 75

Figure 4.15: (A) The dose map of a cross-sectional slice superimposed on its corresponding CT image with distance scales shown for the x- and y-axis. The x-dose profiles of the <sup>177</sup>Lu DPK convolution (red) and noVR MC (blue) are shown in (B) and the y-dose profiles in (C). The error bars on the dose profiles were obtained with the uncertainties in the dose maps. These uncertainties were calculated as described in the text. .... 76

Figure 4.16: The difference in dose profiles between DPK convolution maps calculated using density correction (blue) and without density correction (red) using the activity TIA map from [<sup>18</sup>F]DCFPyL. The dose is in units of  $\mu\text{Gy} \cdot \text{GBq}^{-1} \cdot \text{s}^{-1}$ . .... 77

Figure 4.17: Dose volume histograms from dose distributions calculated by DPK convolution and MC with noVR and with TL dose scoring. There were differences between the DPK convolution and MC DVHs but the MC DVHs were the same. .... 78

Figure 4.18: Organ-level absorbed doses estimated using DPK convolution with and without density correction compared to noVR MC. .... 79

Figure 4.19: A cross-sectional slice from the [<sup>18</sup>F]FCH PET and CT study of a patient (IGPC-02-028) showing (a) media assignment, (b) density map, and TIA map for (c) full activity and (d) noCalc denoting no activity in calcifications. .... 80

Figure 4.20: Dose map from simulated <sup>177</sup>Lu TRT of the same cross-sectional slice as Figure 4.19 in  $U = \mu\text{Gy} \cdot \text{GBq}^{-1} \cdot \text{s}^{-1}$  units. The dose maps were computed using DPK convolution (top) and noVR egs\_mird simulation (middle), an egs\_mird simulation with tracklength scoring (bottom). The left and right images show dose maps with (full) and without (noCalc) activity in the calcifications, respectively. A magnified image of the prostate is shown for each dose map. .... 81

Figure 4.21: X- and Y-dose profile of the density corrected DPK convolution (red) and noVR MC (blue) dose maps with full activity in calcifications of Figure 4.19 are shown here. The DPK simulation-derived uncertainties were convolved with the time-integrated activity to generate error bars on the DPK plot while noVR uncertainties were derived from MC simulation. .... 82

Figure 4.22: (A) X-dose profile of the density corrected DPK convolution (red) and noVR MC (blue) dose maps with no activity in calcifications. (B) Y-dose profile of the same dose maps as (A). (C) X-dose profiles of density corrected DPK convolution maps with full (blue) and no (red) activity in the calcifications. (D) Y-dose profiles of the same dose maps as in (C). The black arrows point to calcifications with no assumed activity in them. .... 83

Figure 4.23: Comparison of (A) X- and (B) Y-dose profiles in DPK convolution dose maps with (blue) and without (red) density correction. The maps were generated with full activity in the calcifications. The black arrows point to calcification. .... 84

Figure 4.24: Dose-volume histograms derived from dose distribution calculated with density corrected DPK convolution calculations, noVR MC and TL MC using TIA matrices with full and no activity in calcifications for (A) prostate, (B) bladder, (C) rectum, and (D) bone marrow. .... 85

Figure 4.25: Organ-level absorbed doses estimated using DPK convolution with and without density correction compared to noVR MC. .... 86

## List of Abbreviations

3D	Three-dimensional
ADT	Androgen deprivation therapy
AS	Active surveillance
BED	Biological effective dose
BMD	Bone mineral density
CI	Confidence interval
CRPC	Castration recurrent prostate cancer
CT	Computed tomography
DNA	Deoxyribonucleic acid
DPK	Dose point kernel
DRE	Digital rectal exam
DVH	Dose volume histogram
DWI	Diffusion-weighted images
EBRT	External beam radiotherapy
FCH	Fluorocholine
FDA	Food and Drug Administration
FDG	Fluorodeoxyglucose
FFT	Fast Fourier transform
HDR	High dose rate
Gy	Gray
HDR	High dose rate
HU	Hounsfield unit
LDR	Low dose rate
LET	Linear Energy Transfer
MC	Monte Carlo
mCRPC	metastatic castration-resistant prostate cancer
MIRD	Medical internal radiation dose
mp	Multiparametric
MRI	Magnetic resonance imaging
PCa	Prostate cancer
PI-RADS	The Prostate Imaging - Reporting and Data System
PSA	Prostate-specific antigen



PSMA	Prostate-specific membrane antigen
RBE	Radiobiological effectiveness
TIA	Time-integrated activity
TL	Tracklength
TNM	Tumour-node-metastasis
TRT	Targeted radionuclide therapy
TRUS	Trans-rectal ultrasound
VR	Variance reduction
VSV	Voxel S-value

## List of Appendices

Appendix A: Copyright Agreement.....	116
Appendix B: Dose Point Kernel Input File.....	120
Appendix C: egs_mird Input File for Patient simulation.....	121

## Chapter 1

### 1 Introduction

#### 1.1 Prostate Cancer Epidemiology

Cancer is characterized by abnormal cell division; derived from multipotent stem cells. But, an alternative hypothesis holds whereby normal stem cells undergo changes and become malignant.<sup>1</sup> Progenitor cells for cancer cells may exhibit the same characteristics as normal cells.<sup>2</sup>

The prostate is a small gland located directly below and posterior to the bladder, and is an essential component of a man's reproductive and urinary systems.<sup>3</sup> Prostate cancer is a disease that has been around for a long time and its history dates back more than a century. In the early years, prostate cancer was denoted a “rare disease”.<sup>4</sup> Many years later, it has become a common disease in men. According to the Canadian Cancer Society in 2019, prostate cancer is the most prevalent cancer among Canadian older males accounting for about 1 in 5 (20%) new cases followed by: lung (13%), colorectal (13%), bladder (8%) and non-Hodgkin lymphoma (5%) cancers. 10% die from prostate cancer among other cancers in men.<sup>5-7</sup>

Risk factors and mortality rate of prostate cancer differ according to geographical areas, environmental exposure, typical western diets (such as consumption of dairy products, red and processed meats, high calcium and high-fat diets), age, and genetic susceptibility.<sup>8-10</sup> There have also been reports of infections, obesity, metabolic syndrome, sexual behavior, and lifestyle, such as exercise, affecting the disease.<sup>11,12</sup> As compared to other cancers, the risk of prostate cancer increases with age.<sup>6</sup> At age 50, the lifetime chance of histological evidence of prostate cancer is 42%, but the risk of having a clinically significant illness is only 9.5%, and the risk of dying from prostate cancer is just 2.9%.<sup>13,14</sup> Early-onset prostate cancer is characterized by a small number of genetic alterations that are mutation-driven. This condition is very favorable for the development and growth of prostate cancer as small breaks in the genome can make the cells susceptible to cancer.<sup>15</sup>

Research has shown that only 0.6% of people between 35 and 44 years were diagnosed with cancer, but between 65 and 74 years of age, the prevalence was higher. Malik et al. found a direct association between age and prostate cancer, as the cancer rate increases 40-fold over the age of 80 compared to age 50. Other studies found contradictory conclusions about race. A cohort study involving 306,100 patients showed no association between black ethnicity and disease. However, according to Nettey et al.,<sup>16</sup> the frequency of prostate cancer was higher in black men as compared to other people who were not black. Their meta-analysis also showed a higher median incidence rate of cancer 19.5/100,000 in the African region compared to Asians, Europeans, or the American population. Additionally, the registry database which covers 28% of the US population showed a high incidence of prostate cancer (38.3/100,000 persons per year) in the African-descents as compared to white (17.3), Asian Americans (11.2/100,000) or Hispanics (18.9) population.<sup>17</sup>

## 1.2 Mechanism

The exact mechanism of prostate cancer is not yet known. However, two plausible hypotheses are changes in the expression of growth factors or steroid hormones. The growth and proliferation of healthy prostate tissue and androgen-dependent prostate cancer are regulated by androgen hormones, such as testosterone, for growth and survival.<sup>18</sup> The growth factors leading to prostate cancer development include: vascular endothelial growth factor (VEGF), transforming growth factor- $\beta$  (TGF $\beta$ ) and insulin-like growth factors (IGFs), especially IGF-1.<sup>19</sup> The prostate is a hormone-sensitive organ, and its functions are stimulated by the activation of steroid hormones which are responsible for the initial development of prostate cancer in 70% of cases.<sup>20</sup>

Testosterone affects genes, called proto-oncogenes, which are responsible for the encoding of several growth factors and serine proteases, including prostate-specific antigen (PSA) and protein C.<sup>21</sup> Testosterone facilitates the expression of apoptotic genes, and hence affects the apoptotic processes and stages of cancer. According to Dobbs et al. estrogen and its receptors play an important role in the development and progression of prostate cancer. The prostate gland has membrane-associated estrogen receptors, G protein-coupled receptor 30 (GPR30), and nuclear estrogen receptors.<sup>22</sup> The activation of

estrogen receptor-alpha causes prostate carcinogenesis whereas the GPR30 refers to the non-genomic action of estrogens.<sup>23</sup> So, these may not only affect the receptors, but also the DNA and mutagenic activity.

A castration-resistant prostate cancer results when androgen-deficient prostate cancer cells develop alternate pathways to compensate for androgen deficiency.<sup>24</sup> Cancer cells may develop pathways hypersensitive to androgen, which are dependent on low levels of androgen to grow.<sup>25</sup> Other factors contributing to the development of prostate cancer include chromosomal alterations and altered expression of oncogenes.<sup>26</sup>

### 1.3 Prostate Cancer Symptoms, Screening and Diagnosis

In the early stages of prostate cancer, there are generally no signs or symptoms. Patients may suffer symptoms such as reduced urine flow, urinary incontinence, inability to urinate, blood in the urine, discomfort or burning sensation during urination, or constant pain in the lower back, upper thighs, or pelvis as their malignancy progresses.<sup>25</sup> These symptoms are frequently misinterpreted by patients as being innocuous, non-specific, or comparable to symptoms associated with other less severe diseases. As a result, it is critical to begin screening for early prostate cancer as soon as possible, because it is considerably more treatable at this stage.<sup>27</sup>

Prostate cancer is diagnosed in more than half of the countries of the world, and is the fifth-largest cause of death in men.<sup>28</sup> Men at  $\geq 60$  of age are often advised to undertake routine screening, to catch the disease before reaching an advanced stage when symptoms typically present. Early-stage disease may not require treatment due to its indolent nature.

Approximately 74% of prostate cancers are diagnosed as Stage (I or II) in Canada, which increases the likelihood of survival (93%) at five years after diagnosis.<sup>6</sup> Prostate cancer is often diagnosed by two screening tests: the digital rectal examination (DRE) and prostate-specific antigen (PSA) blood test. PSA is a protein secreted by epithelial cells of the prostate gland. The PSA test measures the level of PSA in the blood. However, PSA levels can also be raised by benign prostatic hyperplasia, asymptomatic inflammation, prostatitis (an infected prostate), or simply age.<sup>29</sup> The DRE involves the physician

inserting a gloved finger into the rectum, and palpating the prostate gland to determine whether it has increased in size.<sup>30</sup> In the prostate, tumors commonly develop along the rectal wall, whereby hard areas or asymmetry may indicate disease.

A pivotal study from 1994 found that a PSA threshold of 4.0 ng/mL was effective in selecting patients for biopsy to determine whether prostate cancer is present.<sup>31,32</sup> A PSA level of 4–10 ng/mL is considered marginal and indicates a 25% chance of prostate cancer; while a PSA of more than 10 indicates a risk of more than 50%.<sup>33,34</sup> Among the Canadian Task Force on Preventive Health Care (an independent group of clinicians and methodologists that recommends primary and secondary disease prevention maneuvers) investigated the overall effect between the possible benefits and harms of PSA screening with or without digital rectal examination. The task force concluded that PSA screening does not reduce mortality among men of any age conclusively, but it carries an increased risk of harm.<sup>35</sup> PSA screening can lead to false-positive results, prostate biopsy harm, and overdiagnosis.<sup>35</sup> There is an increased risk of false-positive results indicating prostate cancer when there is none due to urinary tract and prostate infections increasing PSA levels. A biopsy is usually recommended for men with high PSA test results. There are several complications associated with prostate biopsy, including hematuria, infection, hospital admission and death. In overdiagnosis, cancer is correctly detected but does not cause symptoms or death. Thus, the task force recommends that the PSA test be avoided in the screening for prostate cancer.<sup>35</sup> Transrectal ultrasound (TRUS) and multi-parametric magnetic resonance imaging (mpMRI)-guided biopsy are two of the most common methods for detecting prostate cancer.<sup>36</sup> In patients with prostate cancer, the mpMRI had a higher detection rate than TRUS.<sup>37</sup> Both TRUS and mpMRI-guided biopsy utilizes imaging guidance and a needle to remove tissue to detect prostate disease.<sup>36</sup>

## 1.4 Prostate Cancer Staging and Grading

A biopsy confirms the presence of prostate cancer, but staging cancer is important to determine if it has spread beyond the prostate. Additionally, staging helps determine which treatment to choose based on the risk of disease spread.

**Table 1.1:** Prostate cancer stage grouping by TNM classification.<sup>38-42</sup>

<b>TNM classification</b>	<b>Label</b>	<b>Representation</b>
Primary Tumour (T)	TX	Primary tumor cannot be assessed
	T0	No evidence of primary tumor
	T1	Clinically inapparent tumor that is not palpable
	T1a	Tumor incidental histologic finding in 5% or less of tissue resected
	T1b	Tumor incidental histologic findings in more than 5% of tissue resected
	T1c	Tumor incidental by needle biopsy found in one or both sides, but not palpable
	T2	Tumor is palpable and confined within the prostate
	T2a	Tumor involves one-half of one side or less
	T2b	Tumor involves more than one-half of one side but not both sides
	T2c	Tumor involves both sides
	T3	Extraprostatic tumor that is not fixed or does not invade adjacent structures
	T3a	Extraprostatic extension (unilateral or bilateral)
	T3b	Tumor invades seminal vesicles
	T4	Tumor is fixed or invades adjacent structures other than seminal vesicles such as the external sphincter, rectum, bladder, levator muscles, and/or pelvic wall
Regional Lymph Nodes (N)	NX	Regional Lymph Nodes
	N0	No positive regional nodes
	N1	Metastasis in a single lymph node 2cm or less in the greatest dimension
	N2	Metastasis in a single lymph node 2cm but no more than 5cm in greatest dimension Multiple lymph nodes, none more than 5cm in greatest dimension
	N3	Metastasis in a lymph node no more than 5cm in the greatest dimension
Distant Metastasis (M)	MX	Distant Metastasis
	M0	No distant metastasis
	M1	Distant metastasis
	M1a	Nonregional lymph nodes metastasis
	M1b	Distant bone(s) metastasis
	M1c	Other site(s) with or without bone disease

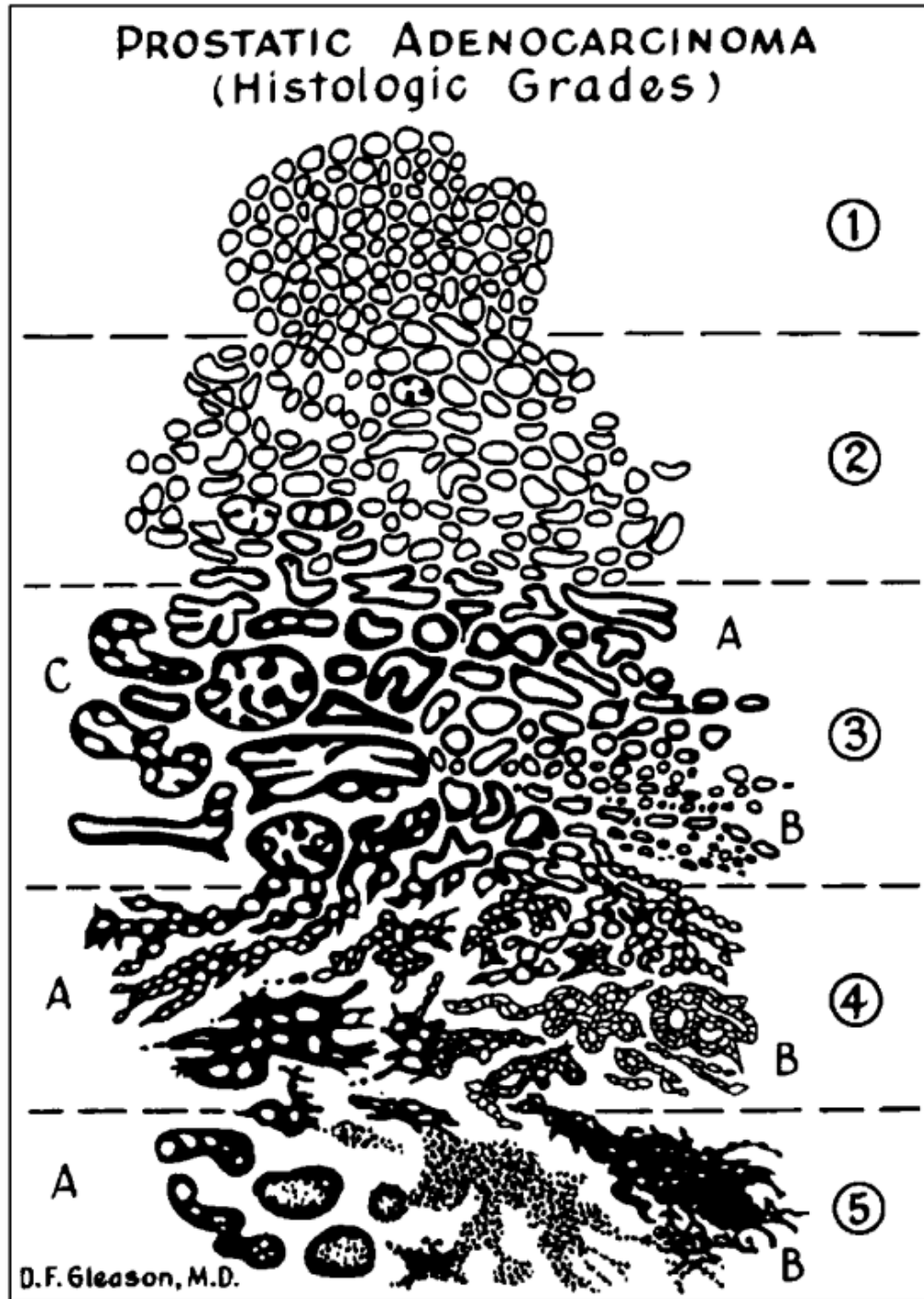


**Figure 1.1:** An illustration of the different Gleason grades. (Reprinted with permission from Macmillan Publishers Ltd: Modern Pathology<sup>43</sup>, copyright (2004).)



**Table 1.2:** The Gleason grading system for prostate cancer.<sup>38-42</sup>

Gleason group	Gleason sum	Representation
1	Gleason Score $\leq 3+3$	The cancerous prostate cells closely resemble normal prostate cells. The glands are small, well-formed, and closely packed.
2	Gleason Score 3+4	The glands are larger and have more tissue between them
3	Gleason Score 4+3	The tissue still has recognizable glands, but the cells are darker. Some cells have left the glands and have started to invade the surrounding tissue.
4	Gleason Score 4+4	The tissue has few recognizable glands. Many cells are invading the surrounding tissue
5	Gleason Score 4+5, 5+4, or 5+5	The tissue does not have recognizable glands. There are often just sheets of cells throughout the surrounding tissue.

**Table 1.3:** Prostate cancer stage groups.<sup>38-42</sup> Abbreviations: T – Primary tumor; N - Regional lymph node; M – Distant metastasis; PSA - Prostate-specific antigen; G - Gleason group.

Stage	T	N	M	PSA	G
Stage I	cT1a-c, cT2a	N0	M0	<10	1
	pT2	N0	M0	< 10	1
Stage IIA	cT1a-c, cT2a	N0	M0	$\geq 10 < 20$	1
	cT2b-c	N0	M0	< 20	1
Stage IIB	T1-2	N0	M0	< 20	2
Stage IIC	T1-2	N0	M0	< 20	3
	T1-2	N0	M0	< 20	4
Stage IIIA	T1-2	N0	M0	$\geq 20$	1 to 4
Stage IIIB	T3-4	N0	M0	Any	1 to 4
Stage IIIC	Any T	N0	M0	Any	5
Stage IVA	Any T	N1	M0	Any	Any
Stage IVB	Any T	N0	M1	Any	Any

A prostate cancer stage grouping is based on TNM, PSA level, and Gleason group-based classification.<sup>44-46</sup> The TNM stage was developed by the American Joint Committee on Cancer and International Union Against Cancer.<sup>46</sup> It is used to identify the extent of a

primary tumor (T), affected lymph nodes in the region (N), and to determine whether metastatic spread has occurred (M).

There are four main stages (I, II, III and IV).<sup>47</sup> The early stages of the disease have a better prognosis than the latter stages. The most advanced stage of the disease is Stage IV. Only a small portion of the prostate is malignant in Stage I, most cells are benign, and the gland feels normal. In Stage II, the inspecting finger can feel a lump in the prostate, and a bigger portion of the prostate is afflicted. The tumor has progressed beyond the prostate in Stage III, and it has spread to lymph nodes or surrounding organs in Stage IV. Table 1.1 shows prostate cancer stage grouping by TNM classification and national comprehensive cancer network (NCCN) staging.

Tumors are graded to make more accurate prognostic predictions. The Gleason Grading System is the most widely used system for grading tumors based on their appearance under a microscope.<sup>38-42</sup> Table 1.2 and Figure 1.1 illustrate the Gleason grading system for prostate cancer. A sample of prostate tissue is taken and prepared on slides during the biopsy procedure. The two most prevalent tumor patterns each receive two grade scores, which are summed to produce a final Gleason sum. Gleason sums range from 2 to 10 and Gleason scores range from 1 to 5; with 1 as prostate tissue showing a small sign of cancer, and 5 as prostate tissue with the most aggressive sign of cancer.<sup>48,49</sup> Furthermore, a tumor with a Gleason sum of 8, 9, or 10 can kill within a short time, whereas a tumor with a Gleason sum of 6 or below may not make a difference clinically.<sup>50,51</sup> Prostate cancer stage groups are shown in Table 1.3.

## 1.5 Prostate Cancer Imaging Modalities

### 1.5.1 Computed Tomography

Conventional computed tomography (CT) is not utilized for the detection and staging of early prostate cancer because of the poor contrast between different nearby soft tissues within the pelvic anatomical region and the lack of molecular information.<sup>52</sup> Moreover, CT is still currently recommended in patients with intermediate- to high-risk prostate cancer and is frequently used to assess nodal and distant metastases.<sup>53</sup> In a recent meta-analysis, researchers found that CT scans had a pooled sensitivity of only 42% for

predicting lymph node involvement.<sup>54</sup> The use of CT for prostate cancer is constrained to distant staging, radiation therapy treatment planning, and PET/CT. CT is not only used to provide anatomical information when co-registered with positron emission tomography (PET) but is also used to perform attenuation and scatter correction to improve the quality of PET images.<sup>55</sup>

### 1.5.2 Multiparametric MRI

Multiparametric MRI (mpMRI) is an imaging method for prostate diagnostic procedures that combines a mix of parametric MRI techniques. Anatomic (T1-weighted and multiplanar T2-weighted images) and functional sequences (diffusion-weighted imaging with apparent diffusion coefficient maps and dynamic contrast-enhanced imaging) all are used in mpMRI.<sup>56</sup> The functional sequences improve the MRI's sensitivity and positive predictive value, while T1-weighted imaging is mainly utilized to assess lymph nodes and bone structures in the region. T2-weighted imaging is a critical sequence in prostate mpMRI because it provides a highly defined anatomical image of the prostate gland's zonal architecture with high soft-tissue contrast.<sup>57</sup> The diffusion of water molecules in tissues can be measured using the diffusion-weighted imaging technique. The dynamic contrast-enhanced imaging technique is used to analyze contrast agent absorption and washout by malignant and non-malignant prostatic tissue, thus providing insight into the microvascular characteristics of tissues.<sup>58</sup>

The acquisition of high-quality images and the deployment of MRI, in combination with the interpreting radiologist's expertise, are critical for optimal prostate mpMRI. The Prostate Imaging Reporting and Data System (PI-RADS) was first proposed in 2012 to address differences in MRI, imaging acquisition protocols, image interpretation, and reporting among centers.<sup>57</sup> PI-RADS is not designed to increase the overall detection rate of all types of prostate cancer. Rather, it is designed to detect clinically significant prostate cancer, which is defined as tumors that are likely to shorten a patient's life expectancy.<sup>57</sup>

### 1.5.3 Positron Emission Tomography/Computed Tomography

Positron emission tomography/computed tomography (PET/CT) imaging is an imaging technique that uses a single device to acquire both metabolic and anatomical imaging in a single diagnostic session. Metabolic imaging is performed using the injection of targeted radio-labelled tracers. There are now several radiotracers in use, and they have found applications in various clinical contexts for detecting cancer. The most common PET tracer is fluorine 18-fluorodeoxyglucose ( $[^{18}\text{F}]\text{FDG}$ ), which is a glucose analog that evaluates glucose transport and metabolism. Researchers have identified and exploited the Warburg effect as a biomarker for malignancy.<sup>59</sup> The Warburg effect is the metabolism of glucose in cancer cells caused by anaerobic glycolysis. When FDG enters a cell, it is phosphorylated into FDG-6-phosphate by hexokinase, which is irreversibly linked to cells.<sup>60</sup> FDG uptake is higher in benign hyperplasia, prostatitis, and inflammation than in normal cells.<sup>61,62</sup> Despite widespread usage of  $[^{18}\text{F}]\text{FDG}$ ,  $[^{18}\text{F}]\text{FDG}$  PET/CT is not recommended for use in the diagnosis of prostate cancer.<sup>63-65</sup> A study has demonstrated that  $[^{18}\text{F}]\text{FDG}$  PET/CT have low sensitivity and specificity for the assessment of prostate cancer due to low tumor-to-background signal and urine excretion of  $[^{18}\text{F}]\text{FDG}$ .<sup>64,66</sup> The urinary excretion of  $^{18}\text{F}$ -FDG masks uptake in the prostate gland and loco-regional lymph nodes.

The use of carbon-11 ( $^{11}\text{C}$ )- or fluorine-18 ( $^{18}\text{F}$ )-labeled choline in imaging is based on an increase in phosphatidylcholine uptake and turnover in cancer cells, which is an important component of phospholipids in the cellular membrane.<sup>67</sup> The advantage of  $^{11}\text{C}$  over  $^{18}\text{F}$  is it has a lower urine excretion rate, which makes it easier to evaluate the prostate, and reduces patient radiation exposure.<sup>68</sup> Because of its low sensitivity, choline PET/CT has a role function in prostate cancer diagnosis and initial staging. Instead, it is mostly used for restaging in cases of biochemical recurrence.<sup>68,69</sup> Because prostate-specific membrane antigen (PSMA)-targeting offers so much potential, many institutions are focusing their efforts on prostate cancer imaging using PET/CT with prostate-specific membrane antigen (PSMA)-targeting.

### 1.5.4 PET/MRI

Higher soft tissue contrast and reduced radiation dosage to the patient are the main advantages of PET/MRI over PET/CT.<sup>70</sup> Major challenges to PET/MRI systems in clinical practice include MR-attenuation correction and the validation of quantitative uptake metrics.<sup>71</sup> A PET/MRI technique has also shown improvements in <sup>18</sup>F-fluorocholine PET specificity relative to PET/CT, which is currently limited by the overlap between malignant and benign diseases. In several studies, PSMA PET/MRI are used together to identify prostate lesions more effectively.<sup>72-76</sup>

## 1.6 Prostate Cancer Treatment Modalities

### 1.6.1 Local Treatment Options

The standard treatment options for localized prostate cancer include some combination of: active surveillance, radical prostatectomy, radiotherapy such as external-beam radiotherapy (EBRT) and brachytherapy, depending on disease staging.

#### 1.6.1.1 Active Surveillance

Active surveillance (AS) is a therapeutic strategy in which patients with NCCN very low or low-risk or low-grade tumors are constantly monitored and only treated if cancer progresses. Patients are closely followed to avoid unneeded therapy until disease advancement or if the patient specifically requests it.<sup>77</sup> Patients with clinically localized prostate cancer, PSA levels less than 10 ng/mL, 2 or fewer positive biopsies, and Gleason scores of 6 or less are candidates for AS.<sup>78</sup> The disadvantages of AS include the presence of an undetected larger or higher-grade tumor that might have been missed at the time of biopsy. Furthermore, not all patients can live happily with a tumor that has not been treated. Based on recently published Toronto experiences with AS, only 30% of 453 patients under AS required and received treatment within 6.8 years of follow-up.<sup>78,79</sup> Results were unsuccessful with a PSA relapse-free survival rate of less than 50% at 3 years corresponding to the 30% of the AS group receiving treatment.<sup>78</sup> Among men under AS, erectile dysfunction and urinary obstruction are common disorders.<sup>80</sup>

### 1.6.1.2 Radical Prostatectomy

Radical prostatectomy treatment is very effective in treating early-stage or NCCN intermediate-risk or selected high-risk prostate cancer. Radical prostatectomy involves removing the prostate gland, seminal vesicles, and the ampulla of the vas deferens. When the prostate is removed and the cancer has not spread, the PSA level can be zero. Patients with properly localized prostate cancer are likely to benefit from radical prostatectomy treatment due to the possibility of a cure. However, in patients with high-grade prostate cancer, tumors that have spread outside the prostate gland, and when the tumor is not completely removed, may not be a complete cure and the disease can recur.<sup>50</sup> Among the risks associated with radical prostatectomy are erectile dysfunction and urine incontinence, blood clots, anesthetic responses, blood loss, and infection.<sup>81</sup>

### 1.6.1.3 External Beam Radiotherapy

Prostate cancer has been treated with external beam radiotherapy since the 1930s, when low-energy orthovoltage x-rays were used as the radiation source. Modern external beam radiotherapy uses a megavoltage linear accelerator to deliver ionizing radiation to treat prostate cancer. The standard dose or dose escalation for external beam radiotherapy is 78 or 79 Gy.<sup>50</sup> Hypo-fractionated regimens have become popular over the last several years. Patients who are considering external beam radiotherapy should have a Gleason score of 7 or a PSA level of 20 ng/mL.<sup>50</sup> Side effects of external beam radiotherapy include bowel problems and urine symptoms including irritative voiding, incontinence, urinary retention, and erectile dysfunction.<sup>82-85</sup>

### 1.6.1.4 Brachytherapy

Brachytherapy treatment is an internal form of radiation therapy that involves inserting radioactive sources (seeds) directly into the prostate. Radioactive seeds emit radiation around the area where they are placed, and can be left temporarily for a short time (high-dose rate) or permanently for a longer time (low-dose rate).<sup>86,87</sup> Transrectal ultrasound-based volume studies are performed before starting therapy to determine the number of needles with radioactive seeds, the isotope, and the strength of isotopes required. A transperineal approach is used for implanting radioactive needles under the guidance of a

transrectal ultrasound or magnetic resonance imaging.<sup>88</sup> For low-dose rate (LDR) brachytherapy, most patients receive 115 - 120 Gy for palladium-103 (<sup>103</sup>Pd) or 145 Gy for iodine-125 (<sup>125</sup>I) with postoperative dosimetry. Iridium-192 (<sup>192</sup>Ir) is a seed for high-dose-rate (HDR) brachytherapy. HDR delivers about 38 Gy in four fractions.<sup>89</sup> Serious complications can potentially arise with brachytherapy, including superficial urethral necrosis and rectal fistula.<sup>90,91</sup>

## 1.6.2 Systemic Treatment Options

Most patients with localized prostate cancer later develop metastatic disease, emphasizing the importance of effective treatment strategies at the early stage of the disease.<sup>92</sup> Systemic therapies offer a promising strategy for improving the clinical outcomes of patients with high-risk localized prostate cancer.<sup>92</sup> Systemic therapies, including androgen deprivation therapy and chemotherapy, are standard-of-care in most solid and metastatic tumors. Advanced prostate cancer has been known under several names over the years, including hormone-resistant prostate cancer and androgen-insensitive prostate cancer.<sup>93</sup> Castration recurrent prostate cancer (CRPC) has been introduced with the realization that intracrine/paracrine androgen production plays a significant role in the resistance of prostate cancer cells to testosterone suppression therapy.<sup>93</sup> Advanced CRPC is a multi-faceted condition that requires multi-disciplinary care while maintaining a high standard of living, and supportive care remains the top priority.<sup>93</sup>

### 1.6.2.1 Chemotherapy

Chemotherapy refers to the administration of cytotoxic chemicals that kill cells to eradicate the tumor or, reduce it, and in turn, the symptoms associated with it and possibly extend a patient's life.<sup>94</sup> Cytotoxic drugs are usually given intravenously. Chemotherapy is a treatment option for prostate cancer and studies have proven its effectiveness in the palliation of symptoms in patients with metastatic disease.<sup>95</sup> Chemotherapy drugs include cabazitaxel, mitoxantrone, taxane, docetaxel and others.<sup>96,97</sup> Chemotherapy drugs have shown different toxicity profiles such as neutropenia,

neutropenic infection, diarrhea, hematuria, peripheral neuropathy, stomatitis, peripheral edema, alopecia, and nail disorders.<sup>97</sup>

### 1.6.2.2 Androgen Deprivation Therapy

Androgen deprivation therapy (ADT) is a hormone-based therapy for patients with advanced prostate cancers and selected patients with localized prostate cancers. ADT has been evaluated in clinical trials for patients with metastatic and advanced locoregional diseases, but the risk-benefit ratio, especially in earlier stages, remains unclear.<sup>98</sup> Research has shown that ADT can cause bone, endocrine, sexual, and cognitive dysfunctions as well as adverse effects on body composition and health.<sup>99</sup> ADT increases the risk of developing diabetes, a cardiovascular event, and a decrease in bone mineral density (BMD).<sup>100,101</sup> ADT studies have shown that BMD declines as early as 6 months into treatment. BMD decreased by 3% and 2.7% for the lumbar spine and the femoral neck at 6 months, by 4.6% and 3.9% at 12 months, and by 7.1% and 6.6% at 18 months, respectively.<sup>101</sup> The results of another study showed a mean bone loss of 3.3% at the hip and 5.3% at the distal radius one year after ADT.<sup>101</sup> Before patients begin ADT, they should be fully informed about the risks and the potential benefits of therapy.

## 1.7 Targeted Radionuclide Therapy

Targeted radionuclide therapy (TRT) is a systemic treatment just like chemotherapy and androgen deprivation therapy. It involves the administration of a radioactive substance into the bloodstream of patients. However, it differs from chemotherapy by specifically targeting tumor cells and sparing normal tissues with a reduction in potential side effects. TRT differs from traditional radiotherapy in that radiation is not from an external source. Rather, it is an internal exposure to radiation from the intravenously administered radiolabeled targeted molecule. The radionuclide is usually incorporated into a carrier molecule, forming a magic bullet in Paul Ehrlich's words, with a high affinity for cancer cells via receptors, antigens, or enzymes.<sup>102</sup> TRT differs from external beam radiotherapy (EBRT) in that it requires detailed knowledge about tumor biology rather than tumor location.



The desired tumoricidal effect of TRT is from ionizing radiation emitted by the radionuclide. The radionuclide (e.g.,  $^{18}\text{F}$ ,  $^{68}\text{Ga}$ ) used in SPECT and PET molecular imaging emits gamma rays which have strong penetrating power in tissue, up to centimeters. On the other hand, TRT radionuclides emit particulate radiations such as alpha particles, beta particles, or Auger electrons. These radiations have a lower penetrating power relative to gamma radiation. Beta particles have a longer range than alpha particles. Beta particles have a range of tens in cell diameters, but alpha particles have a much shorter range to destroy cancer cells surrounding the radionuclide. While particulate radiation is preferred for TRT, only emitted gamma rays can be used for imaging. This leads to the concept of a ‘theranostic’ pair<sup>103,104</sup>, where the same targeting molecule is labeled with a gamma-emitting radionuclide (e.g.,  $^{177}\text{Lu}$ ,  $^{131}\text{I}$ ) for SPECT imaging and with a particulate emitting one for TRT.

### 1.7.1 Targeted Radionuclide Therapy: Overview

Significant advancements have been made in TRT. Initially, this therapeutic technique started with the use of radioactive isotopes of iodine ( $^{131}\text{I}$ ,  $^{128}\text{I}$ ) with a NaI-targeted molecule in studying thyroid physiology and treatment of thyroid carcinoma.<sup>105–107</sup> Other targeted molecules have been labeled with radioactive iodine and applied in the treatment of other diseases. Such is the case of  $^{131}\text{I}$  metaiodobenzylguanidine (MIBG) for the treatment of metastatic and/or recurrent pheochromocytoma or paraganglioma which eventually led to the Food and Drug Administration (FDA) approval (Azedra®).<sup>108</sup> TRT applications using  $^{131}\text{I}$  has been used in patients with low-grade and transformed Non-Hodgkin’s Lymphoma which is usually incurable. The approach utilized  $^{131}\text{I}$ -tositumomab and unlabeled tositumomab in five clinical trials, which produced a significant response rate.<sup>109</sup>

Researchers have also developed an interest in other radionuclides with better physical characteristics such as the energy of the emitted radiation (e.g., beta particle) and half-life. This led to the use of Yttrium-90 ( $^{90}\text{Y}$ ) which has higher beta energy and a shorter half-life than  $^{131}\text{I}$ . The higher beta energy is important to treat larger tumors, and the shorter half-life for the shorter biological half-life of the targeting radiolabeled molecule. There was no gamma-emitting radioisotope of Yttrium (Y), and this resulted in the

development of Indium ( $^{111}\text{In}$ ), which was then used to assess the kinetics of the labeled immunoglobulin.<sup>110,111</sup>

A list of TRT clinical trials for the treatment of different cancers, radiolabeled ligand and their treatment doses can be found in Table 1.4. TRT has found application in neuroendocrine tumors because of the overexpression of somatostatin receptor. This led to the development of octreotide, an octapeptide, which is a somatostatin receptor ligand analog. Different radiolabeled analogs of octreotide were developed ranging from  $^{123}\text{I}$ -tyrosine-3 octreotide to the different analogs of the  $^{90}\text{Y}$  octreotide analog.

**Table 1.4:** List of TRT clinical trials for the treatment of different neuroendocrine tumors.

Trial Identification	Study Phase	No. of Patients	Disease	Radioligand	Treatment Dose	Study Location	Start - End date (MM/DD/YYYY)
NCT04790708	Not applicable	250	Neuroendocrine Tumors	Lutetium-177 [ <sup>177</sup> Lu]DOTATOC	5 cycles of 3,7 - 5,55 gigabequerel (GBq) of [ <sup>177</sup> Lu]DOTATOC every 8-10 weeks. Cumulative activity: 18,5 - 27,75 GBq	University Hospital of Ferrara, Ferrara, Italy	July 2, 2018 - June 30, 2023
				Yttrium-90 [ <sup>90</sup> Y]DOTATOC	5 cycles of 1,85 - 2,775 GBq of [ <sup>90</sup> Y]DOTATOC every 8-10 weeks. Cumulative activity: 9,25 - 13,875 GBq		
NCT03648073	Phase 1, Phase 2	30	Hepatocellular Carcinoma	177Lu-edotreotide PRRT and Everolimus Other: Amino-Acid Solution	<sup>177</sup> Lu-edotreotide [ <sup>90</sup> Y]DOTATOC. A maximum of four cycles of 7.5 ± 0.7 GBq 177Lu-edotreotide, each. 4 cycles, 90 days apart (total duration: 270 days/9 months)	University of Alabama at Birmingham Medical Center, Birmingham, Alabama, United States	1/30/2019 - December 31, 2022
NCT04029428	phase 2	150	Neuroendocrine Tumors	[ <sup>177</sup> Lu]DOTATOC	Four administrations of 5,55GBq up to 7,4 GBq [ <sup>177</sup> Lu]DOTATOC administered at 8-week intervals.	Centrum Diagnostyczno-Lecznicze Gammed, Warszawa, Poland	11/2/2004 - January 1, 2021
NCT00416949	Early Phase 1	10	Neuroendocrine Tumors	[ <sup>177</sup> Lu]DOTATATE	Experimental: 28 GBq [ <sup>177</sup> Lu]DOTATATE 5 cycles of 5.5 GBq (150 mCi) each, up to the total cumulative activity of 28 GBq (750 mCi) [ <sup>177</sup> Lu]DOTATATE Experimental: 22 GBq [ <sup>177</sup> Lu]DOTATATE 6 cycles of 3.7 GBq (100 mCi) each, up to the total cumulative activity of 22 GBq (600 mCi) [ <sup>177</sup> Lu]DOTATATE	The Holden Comprehensive Cancer Center, Iowa City, Iowa, United States	10/11/2018 - December 2025
NCT04385992	Phase 2	30	Neuroendocrine Tumors	<sup>177</sup> Lu Octreotate (Lutate)	7.8GBq <sup>177</sup> Lu Octreotate (Lutate) given intravenously (IV) on day 1 every 8 weeks for 4 cycles.	Ospedale San Raffaele, Milano, Italy	11/29/2019 - November 30, 2021
NCT04194125	Phase 2	25	Neuroendocrine Tumors	[ <sup>90</sup> Y]DOTATOC	Maximum cumulative [ <sup>90</sup> Y]DOTATOC activity of 11.1 GBq (300 mCi), divided into 4 cycles (1.8 - 2.8 GBq for each cycle) with an interval of 6 - 8 weeks between cycles.	Centrum Diagnostyczno-Lecznicze Gammed, Warszawa, Poland	February 1, 2019 - January 31, 2022
NCT02736500	Phase 1	37	Neuroendocrine Tumors	Sunitinib and <sup>177</sup> Lu-DOTA0-Tyr3-Octreotate	177Lu-DOTA0-Tyr3-Octreotate or OCLU 7.4 GBq per injection (max: 4 injections) and Active Comparator: Sunitinib	Giovanni Paganelli, Meldola, FC, Italy Lisa Bodei, Milan, Italy	9/2/2015 - June 2021
NCT02358356	Phase 2	72	Midgut and Pancreatic Neuroendocrine Tumors	<sup>177</sup> Lu-Octreotate or LuTate or <sup>177</sup> Lu-[DOTA0,Tyr3]octreotate or [ <sup>177</sup> Lu]DOTATATE	4-cycle induction course (23 Gy) and for each subsequent cycle (6 Gy)	Australia	11/1/2015 - December 2020

The overall response rate observed with the  $^{90}\text{Y}$  octreotide analog was superior to that of  $^{123}\text{I}$ . Despite promising results obtained with the  $^{90}\text{Y}$  analog, the search for alternative radionuclides continued, which led to the development of lutetium-177 ( $^{177}\text{Lu}$ ). This radionuclide has lower beta energy and a longer half-life compared to the  $^{90}\text{Y}$  analog. This suggests that a greater fraction of the beta energy will be absorbed by the target tissue, and less radiation exposure to the surrounding tissues, is an advantage for smaller tumors. Also, this radionuclide emits gamma radiation which can be used for imaging purposes.<sup>112-114</sup>

### 1.7.2 Targeted Radionuclide Therapy Radionuclides, Carrier Molecules and Tumor Targeting

Radionuclides for targeted radiotherapy must possess certain qualities. Radiation emitted by radionuclides must inflict damage, mainly DNA double-strand breaks, to kill cancer cells, while minimizing any damage to bystander normal cells. As such, the radionuclide can be an alpha, beta, or Auger electron emitter, as these types of particles deposit energy concentrated with higher density than gamma rays, and hence produce more double-strand breaks. The radionuclide selection however should be selected based on the energy of the emitted particle, and the tumor size to be treated.<sup>115</sup> Table 1.5 shows a list of radionuclides used in targeted radionuclide therapy, their half-life, particle energy, maximum particle energy, and penetration range in tissue.

The physical half-life of the radionuclide should correspond to the kinetics of the carrier in vivo. It should be long enough to accommodate the time of synthesis, delivery to the site of administration, injection, and residency time within the tumor. The optimum half-life ranges from six hours to seven days although  $^{89}\text{Sr}$  is an exception which has a half-life of 50 days.<sup>116</sup> The preferred TRT radionuclides must also possess a high grade of chemical purity and be devoid of traces of metal impurities. Finally, a radionuclide must be able to bind to a wide variety of carrier molecules and its preparation must be cost-effective to ensure universal accessibility.<sup>117</sup>

**Table 1.5:** List of radionuclides used in targeted radionuclide therapy, their half-life, particle energy, maximum particle energy, and penetration range in tissue.<sup>94,118–121</sup>

Isotope	Abbreviation	Emitted particles $\beta^-$ : Beta, $\gamma$ : Gamma $\alpha$ : Alpha EC: Electron capture	Half-life	Max. particle energy (keV)	Tissue penetration depth (mm)
Lutetium-177	<sup>177</sup> Lu	$\beta^-$ , Auger, EC	6.65 days	497	1.600
Iodine-131	<sup>131</sup> I	$\beta^-/\gamma$	8.02 days	971	2.300
Yttrium-90	<sup>90</sup> Y	$\beta^-$	2.67 days	2280	12.000
Terbium-161	<sup>161</sup> Tb	$\beta^-$ /Auger and EC	6.89 days	154	0.030
Bismuth-213	<sup>213</sup> Bi	$\alpha/\beta^-$	45.6 min	8381	0.084
Actinium-225	<sup>225</sup> Ac	$\alpha$	10.0 days	28000	0.061
Radium-223	<sup>223</sup> Ra	$\alpha$	11.43 days	28200	0.080
Astatine-211	<sup>211</sup> As	$\alpha$	7.2 days	5870	0.067
Indium-111	<sup>111</sup> In	Auger/ $\gamma$	2.8 days	0.35	4.000 nm
Lead-212	<sup>212</sup> Pb	$\alpha, \beta^-$ , EC	10.6 h	6051	0.080

Just as a radionuclide must meet certain requirements, carrier molecules too must also possess attributes for their use in TRT. This includes high affinity, and specificity for the target, lack of toxicity or immunogenicity. Most carrier molecules are antibodies and peptides, which are resistant to self-radiolysis. Carrier molecules should be well-preserved under storage conditions and when in contact with biological liquids, and pure chemically. Furthermore, carrier molecules should be simple, cost-effective production and have a high binding affinity to a variety of radionuclides.<sup>117</sup>

An ideal TRT target (antigen, receptor, and others) must possess an even expression and distribution over the entire cell surface of a malignant tumor, and have a low or negligible expression in normal cells to minimize unwanted side effects and uptake in the cancer site, with negligible washout from blood flow.<sup>117</sup>

### 1.7.3 Targeted Radionuclide Therapy for Prostate Cancer

Advancements have been continuously made in the treatment of prostate cancer. The 5-year survival rate for local and regional prostate cancer is approximately 98%.<sup>122</sup> However, the rate drops to 30% for patients with metastases, despite advances in current treatment options such as surgery, hormone therapy, anti-androgen therapy, and chemotherapy.<sup>122</sup> Thus, the need for other therapeutic choices, like TRT are needed.

In 1987, Horoszewicz et al. discovered a new type II transmembrane enzymatic protein marker on the prostate carcinoma cell line called LNCaP.<sup>123</sup> This marker was later called prostate-specific membrane antigen (PSMA). PSMA is overexpressed in prostate cancer cells and can be detected in the serum of patients. PSMA is overexpressed in 90% to 100% of prostate cancer cases, and it correlates highly with disease progression, with high PSMA expression in hormone-resistant tumors and metastatic disease.<sup>124</sup> PSMA is an excellent target for diagnostic imaging and therapy.<sup>125</sup> PSMA inhibitors or ligands have been developed based on small peptide molecules modified with urea and labeled with different radionuclides.<sup>126–128</sup> Diagnostic radionuclides include <sup>99m</sup>Tc and <sup>111</sup>I for single-photon emission computed tomography (SPECT) and PET isotopes (<sup>68</sup>Ga, <sup>18</sup>F and <sup>89</sup>Zr), while therapeutic radionuclides include <sup>177</sup>Lu, <sup>225</sup>Ac, <sup>131</sup>I and <sup>90</sup>Y.<sup>129</sup> The list of radiolabeled ligands used for PSMA targeting in targeted radionuclide therapy for prostate cancer is reported in Table 1.6. These radiolabeled targeted tracers are administered intravenously, and accumulate at the tumor sites from binding to PSMA.

The preliminary results of PSMA-targeted radionuclide treatment have accelerated preclinical research into potential clinical studies. A list of TRT clinical trials using PSMA-targeting is shown in Table 1.7. PSMA has been found to possess an intracellular and extracellular epitope for an antibody. In vivo characterization of the intracellular epitope of PSMA has been done with a 7E11 monoclonal antibody.<sup>130</sup> In vitro characterization (pharmacokinetics, biodistribution, affinity, and specificity) has been carried out using murine monoclonal antibodies J415, J533, and J591, of which J591 was the most promising.<sup>131</sup> <sup>90</sup>Y and <sup>177</sup>Lu were labeled J591. Subsequently, <sup>90</sup>Y and <sup>177</sup>Lu were labeled DOTA-J591 and were evaluated in nude mice with human prostate cancer xenografts. Both <sup>90</sup>Y and <sup>177</sup>Lu labeled J591 were found to decrease tumor size and prolong survival.<sup>130,132</sup> Clinical trials were conducted on <sup>177</sup>Lu and <sup>90</sup>Y radiolabeled J591 to compare their efficacy and hematological toxicity. The <sup>177</sup>Lu was chosen as the preferred candidate. Even though <sup>90</sup>Y had a significant antitumor effect, <sup>90</sup>Y was not chosen because had hematological adverse effects.<sup>133–135</sup>

The Food and Drug Administration (FDA) has approved <sup>18</sup>F labeled PSMA ligand such as 3-(3-[1-carboxy-5-[(6-[<sup>18</sup>F]fluoro-pyridine-3-carbonyl)-pentyl]-ureido)-pentanedioic

acid, commonly called [ $^{18}\text{F}$ ]DCFPyL, to be used for imaging prostate cancer.<sup>136</sup> [ $^{18}\text{F}$ ]DCFPyL produced high image quality and demonstrated excellent sensitivity when imaging small prostate lesions.<sup>137</sup>

**Table 1.6:** List of radiolabeled ligands used for PSMA targeting in targeted radionuclide therapy for prostate cancer.

Ligand	Radionuclides	Radioligand	References
PSMA-617	Lutetium-177	[ $^{177}\text{Lu}$ ]PSMA-617	138
	Actinium-225	[ $^{225}\text{Ac}$ ]PSMA-617	139
	Indium-111	[ $^{111}\text{In}$ ]PSMA-617	140
	Gallium-68	[ $^{68}\text{Ga}$ ]PSMA-617	141
	Yttrium-90	[ $^{90}\text{Y}$ ]PSMA-617	142
PSMA-11	Gallium-68	[ $^{68}\text{Ga}$ ]PSMA-11	143
PSMA-1007,	Fluorine-18	[ $^{18}\text{F}$ ]PSMA-1007	144
DCFPyL	Fluorine-18	[ $^{18}\text{F}$ ]DCFPyL	145,146
PSMA-I&T	Lutetium-177	[ $^{177}\text{Lu}$ ]PSMA-I&T	147
	Actinium-225	[ $^{225}\text{Ac}$ ]PSMA-I&T	148
	Indium-111	[ $^{111}\text{In}$ ]PSMA-I&T	149
	Gallium-68	[ $^{68}\text{Ga}$ ]PSMA-I&T	150
MIP-1095	Iodine-123	[ $^{123}\text{I}$ ]MIP-1095	151
	Iodine-131	[ $^{131}\text{I}$ ]MIP-1095	151
MIP-1072	Iodine-123	[ $^{123}\text{I}$ ]MIP-1072	152
CTT1057	Fluorine-18	[ $^{18}\text{F}$ ]CTT1057	153
FSU-880	Fluorine-18	[ $^{18}\text{F}$ ]FSU-880	154
JK-PSMA-7	Fluorine-18	[ $^{18}\text{F}$ ]JK-PSMA-7	155
MIP-1404/-1405	Technetium-99m	[ $^{99\text{m}}\text{Tc}$ ]MIP-1404-1405	156
PSMA I&S	Technetium-99m	[ $^{99\text{m}}\text{Tc}$ ]PSMA I&S	157
CTT1400	Lutetium-177	[ $^{177}\text{Lu}$ ]CTT1400	158
AIF-PSMA-11	Fluorine-18	[ $^{18}\text{F}$ ]AIF-PSMA-11	159
rhPSMA-7.3	Fluorine-18	[ $^{18}\text{F}$ ]rhPSMA-7.3	160
RPS-027	Iodine-131	[ $^{131}\text{I}$ ]RPS-027	161
	Astatine-211	[ $^{211}\text{At}$ ]RPS-027	161
DCIBzL	Iodine-123	[ $^{123}\text{I}$ ]DCIBzL	157
	Iodine-131	[ $^{131}\text{I}$ ]DCIBzL	162
CTT1402	Lutetium-177	[ $^{177}\text{Lu}$ ]CTT1402	163

Also, <sup>68</sup>Ga-labelled PSMA ligand Glu-urea-Lys(Ahx)-HBED-CC ([<sup>68</sup>Ga]PSMA-11), shows outstanding affinity to PSMA and, a highly selective uptake in imaging prostate cancer, lymph node metastases and distant metastases are available and approved by FDA December 2020.<sup>164,165</sup> <sup>68</sup>Ga-PSMA PET/CT has been shown to be able to detect prostate carcinoma relapses and metastases with significantly improved contrast compared to [<sup>18</sup>F]FCH PET/CT.<sup>166</sup>

The VISION clinical trial (NCT03511664) is a randomized phase 3 clinical trial of [<sup>177</sup>Lu]PSMA-617 in the treatment of patients with progressive PSMA-positive metastatic castration-resistant prostate cancer that were previously treated with at least one androgen-receptor-pathway inhibitor and one or two taxane regimens and who had PSMA-positive gallium-68 [<sup>68</sup>Ga]PSMA-11 positron-emission tomographic-computed tomographic scans.<sup>167</sup> All patients receive a fixed amount of 7.4 gigabequerels (GBq) of [<sup>177</sup>Lu]PSMA-617 intravenously every 6 weeks (+/- 1 week) for a maximum of 6 cycles regardless of their body weight.<sup>167</sup> [<sup>177</sup>Lu]PSMA-617 increased imaging-based progression-free survival and overall survival when added to standard care. Compared to standard care, imaging-based progression-free survival increased from 3.7 to 8.7 months with a decrease in the hazard ratio for death at 0.40; 99.2% confidence interval [CI] of 0.57 to 0.29, P<0.001. The overall survival increased with a median from 11.3 months to 15.3 months with a decrease in the hazard ratio for death at 0.62; 95% CI, from 0.74 to 0.52 with P<0.001.<sup>167</sup>

Therapeutic improvement can be achieved by personalizing TRT treatments based on a patient's body mass and dosimetry.

#### 1.7.4 TRT for Prostate Cancer: Current Limitations and Possible Solutions

TRT has demonstrated promising outcomes in the treatment of PCa and has advantages including target (PSMA) specificity, therapeutic efficacy, low toxicity to normal surrounding healthy tissues, locoregional control, and excellent palliation of symptoms.<sup>168</sup> However, the challenges that come with TRT include the isolation of patients, the limited availability of radiopharmaceuticals and isolation beds, and the



storage of radioactive waste. To achieve the goals of TRT, a multidisciplinary approach is required, including the design and production of carrier molecules and radionuclides.<sup>168</sup> Radionuclides have to be shipped in from production sites at a distance from cancer centers with transport issues to be resolved. To produce therapeutic radionuclides, more powerful accelerators are needed with higher energy and complexity than the cyclotrons available in Positron emission tomography (PET) centers. Even the smaller cyclotrons available at PET centers are expensive and not readily available at some locations, but when it comes to larger cyclotrons, things get even more complicated.<sup>169,170</sup>

For PCa, complications from TRT are generally limited to the haematopoietic tissue and serious side effects are observed. According to published studies, 91% of patients receiving [<sup>177</sup>Lu]PSMA-617 and 100% of patients receiving [<sup>225</sup>Ac]J591 experienced at least one adverse event, such as pain, fatigue, dry mouth, nausea, and hematologic toxicity.<sup>171,172</sup> <sup>177</sup>Lu PSMA therapy has been associated with low-grade toxicities in all published studies:<sup>173</sup> about 30% of men experience dry mouth after treatment. Fatigue is a common side effect for up to 25% of men treated. There has also been some nausea reported in up to 10% of men, particularly during the first 24–48 hours following injection. As of now, no studies have reported renal toxicity, although it seems likely that this would be a longer-term complication if it were to occur.<sup>174,175</sup> It has been reported that men with a high burden of skeletal metastases and borderline bone marrow function may develop haematological toxicity after <sup>177</sup>Lu PSMA therapy. This is more of an innocent bystander effect than a direct radiation effect on bone marrow.<sup>176</sup> A bystander effect is a biological effect (response) that occurs when non-irradiated neighbors (cells) respond to radiation. These biological responses include DNA damage, mutation, and apoptosis. 10%–25% of males with substantial bone metastases had haemoglobin or platelet levels that dropped by Grade 1–2. No signs of marrow damage/toxicity were present in men with low amounts of skeletal metastases.<sup>176</sup>

Dosimetry calculations are likewise required for individual patients. Since its establishment in the 1950s, TRT has been concerned with issues of precise absorbed dose calculation.<sup>177</sup> Mainly because the distribution of the radiopharmaceutical in the target is non-uniform, calculating the dose delivered to a target remains difficult.<sup>178</sup> The FDA

approved the MIRD schema for absorbed dose calculation of radiotracers used in TRT, but it is not patient-specific.<sup>177</sup>

Patients with metastatic castration-resistant prostate cancer (mCRPC) may benefit from TRT with [<sup>177</sup>Lu]PSMA-617. Paganelli et al.,<sup>179</sup> conducted a prospective single-arm, open-label phase II study to determine the safety and initial response to a minimal effective injected activity/cycle of [<sup>177</sup>Lu]PSMA-617 in mCRPC patients. MIRD formalism (OLINDA/EXM software, v 1.0) was used to calculate the adsorbed dose. A unit-density sphere model was employed for submandibular and lacrimal glands and tumor lesion evaluation, while an adult male phantom was used for kidney, liver, red marrow, and whole-body assessment. This dose calculation method is limited for reasons discussed later (see §2.3.1). More accurate dosimetry of other ligands or other radionuclides can be re-evaluated to adjust the treatment protocol to minimize treatment complications.<sup>180</sup> Improved patient-specific absorbed dose estimations will lead to better toxicity control and clinical outcomes for prostate cancer and other solid tumors in the future. The goal of this thesis is to develop a patient-specific absorbed dose calculation method to address the TRT dosimetry challenges.

**Table 1.7:** List of clinical trials for the treatment of prostate cancer.

Trial Identification	Study Phase	No. of Patients	Disease	Radioligand	Treatment Dose	Study Location	Start - End date (MM/DD/YYYY)
NCT04597411	Phase 1	30	Prostatic Neoplasms, Castration-Resistant	[ <sup>177</sup> Lu]PSMA-I&T	Single dose 2.0-8.0 GBq treated once every 8-12 weeks.	St. Vincent's Hospital Research Office-Translational Research Center, Darlinghurst, Australia Steve Biko Hospital-Department of Nuclear Medicine, Pretoria, South Africa	April 1, 2021 - February 20, 2023
NCT03874884	Phase 1	52	Metastatic Castration Resistant Prostate Cancer	[ <sup>177</sup> Lu]PSMA-617	Patients received fixed 7.4 GBq of lutetium Lu 177-PSMA-617 every 6 weeks	St Vincent's Hospital Sydney, Sydney, New South Wales, Australia Peter MacCallum Cancer Centre, Melbourne, Victoria, Australia	July 9, 2019 - October 2022
NCT04796467	Early Phase 1	30	Prostate Cancer	[ <sup>177</sup> Lu]PSMA-617, [ <sup>177</sup> Lu]J591 and [ <sup>68</sup> Ga]PSMA-HBED-CC	[ <sup>177</sup> Lu]PSMA-617 [1.85 GBq (50 mCi) - 9.25 GBq (250 mCi)] x2 doses, 2 weeks apart, [ <sup>177</sup> Lu]J591 [1.35 GBq/m <sup>2</sup> or 36.5 mCi/m <sup>2</sup> ] x2 doses, 2 weeks apart, [ <sup>68</sup> Ga]PSMA-HBED-CC [185 ±74 MBq or 5 ±2 mCi]	Peking Union Medical College Hospital, Beijing, Beijing, China	October 1, 2020 - October 1, 2022
NCT04188587	Phase 2	30	Metastatic Castration-resistant Prostate Cancer	[ <sup>177</sup> Lu]PSMA-617	5 GBq of 177Lu-PSMA in 2 cycles, separated by 6 weeks.	Nanjing First Hospital, Nanjing, Jiangsu, China	January 1, 2019 - August 2020
NCT03805594	Phase 1	43	Metastatic Prostate Carcinoma Prostate Adenocarcinoma Stage IV	[ <sup>177</sup> Lu]PSMA-617 and [ <sup>68</sup> Ga]PSMA-HBED-CC	[ <sup>177</sup> Lu]PSMA-617 [50mCi (1.85GBq) - 300mCi (11.1GBq)] intravenous X2 doses, 2 weeks apart (Visit 1 and 2) [ <sup>68</sup> Ga]PSMA-HBED-CC [5 ±2mCi or 185 ±74MBq] intravenous during screening and at 12 weeks with standard imaging	University of California, San Francisco, San Francisco, California, United States	January 15, 2019 - April 19, 2022
NCT03545165	Phase 1 and Phase 2	6	Prostate Cancer	[ <sup>177</sup> Lu]PSMA	<sup>177</sup> Lu-PSMA 3.7-5-5 GBq Intravenous Slowly in 15-30 ' Day 1/ every 8-12 weeks Four cycles every 8-12 weeks	Weill Cornell Medical College, New York, New York, United States	April 18, 2018 - July 15, 2020

NCT04430192	Phase 1 and Phase 2	20	Prostatic Neoplasms	[ <sup>177</sup> Lu]PSMA-617	6-8.5GBq once every 6 weeks until progressive disease, prohibitive toxicity or a maximum of 6 cycles.	Peter MacCallum Cancer Centre, Melbourne, Victoria, Australia	August 6, 2020 - June 30, 2023
NCT03042468	Phase 1 and Phase 2	46	Prostate Cancer	[ <sup>177</sup> Lu]PSMA-617	7.5 GBq (± 10%) <sup>177</sup> Lu-PSMA every 6 weeks x 2 cycles. Docetaxel 75 mg/m <sup>2</sup> commencing 6 weeks later, every 3 weeks x 6 cycles	Tulane Cancer Center Clinic, New Orleans, Louisiana, United States Weill Cornell Medical College, New York, New York, United States	December 2016 - September 2022
NCT03454750	Phase 2	210	Metastatic Castration Resistant Prostate	[ <sup>177</sup> Lu]PSMA-617	7.4GBq (± 10%) every 6 weeks; maximum 6 cycles	Istituto Scientifico Romagnolo per lo Studio e la Cura dei Tumori (IRST), Meldola, FC, Italy	April 19, 2017 - August 2022
NCT03392428	Phase 2	201	Cancer of the Prostate Metastatic Cancer	<sup>177</sup> Lu-DOTA-rosopatab	76 mCi each (equivalent to a 45 mCi/m <sup>2</sup> dose in a standard 1.7m <sup>2</sup> individual) of [ <sup>177</sup> Lu]DOTA-rosopatab, given 14 days apart, plus best SoC Other Name: [ <sup>177</sup> Lu]TLX591	Australia: Liverpool, St Vincent's, Royal North Shore, Calvary Mater Newcastle, Royal Brisbane and Womens, Royal Adelaide, Austin, Fiona Stanley, Monash Moorabbin, Sir Charles Gairdner Hospital, and Peter MacCallum Cancer Centre	January 29, 2018 - June 13, 2022
NCT04343885	Phase 2	140	Metastatic Hormone Naïve Prostate Cancer	[ <sup>177</sup> Lu]Ludotadipep	Dose is sequentially elevated starting from a low dose to a high dose (50±5 mCi, 75±8 mCi, 100±10 mCi, 125±13 mCi, 150±15 mCi).	Australia: Liverpool, St Vincent's, Royal North Shore, Calvary Mater Newcastle, Royal Brisbane and Womens, Royal Adelaide, Austin, Fiona Stanley, Monash Moorabbin, Sir Charles Gairdner Hospital, and Peter MacCallum Cancer Centre	April 21, 2020 - April 2024
NCT04663997	Phase 2	200	Prostate Cancer	[ <sup>177</sup> Lu]EB-PSMA-617	All patients were intravenous injected with single dose 0.80-1.1 GBq (21.5-30 mCi) of [ <sup>177</sup> Lu]EB-PSMA-617, then monitored at 2, 24, 72, 120 and 168 hours post-injection.	BCCA - Vancouver Cancer Centre, Vancouver, British Columbia, Canada	December 17, 2020 - July 31, 2025
NCT04876651	Phase 3	387	Metastatic Prostate Cancer	[ <sup>177</sup> Lu]DOTA-TLX591-CHO	Two single IV infusions of 76 mCi (2.8 GBq) each (equivalent to a 45 mCi/m <sup>2</sup> administered activity in a standard 1.7m <sup>2</sup> individual) of [ <sup>177</sup> Lu]DOTA-TLX591-CHO, given 14 days apart.	Diagnostic Nuclear Imaging at Hollywood Private Hospital, Perth, Western Australia, Australia GenesisCare SJOG Medical Centre, Murdoch WA, Perth, Western Australia, Australia	July 15, 2021 - June 1, 2026

## Chapter 2

### 2 Dose Calculation Methods in Targeted Radionuclide Therapy

Direct assessment of absorbed dose distributions in vivo from administered radiopharmaceuticals in targeted radionuclide therapy is challenging.<sup>178</sup> To achieve the highest possible therapeutic effect, targeted radionuclide therapy aims to deliver the highest possible absorbed dose to the tumor while sparing healthy tissues.<sup>181</sup> Furthermore, patient-specific targeted radionuclide therapy is becoming increasingly critical to ensure effective treatment, especially with the growth of targeted radionuclide therapy applications.<sup>182</sup> The 3D absorbed dose distribution is important in clinical practice since low dose regions within the target (tumor) might lead to lesion recurrence, while high radiation regions can cause tissue necrosis. Studies have shown that normal organs have varied levels of radiation tolerance and are exposed to non-uniform dose distributions, resulting in a range of toxicities.<sup>183</sup>

#### 2.1 Approaches to Dosimetry in Targeted Radionuclide Therapy

Dosimetry protocol in radionuclide therapy requires the estimation of dose from each treatment cycle. For dosimetric calculations, quantitative imaging, such as single-photon emission computed tomography (SPECT) or positron emission tomography (PET) is used to estimate non-invasively the 3D activity distribution of the therapeutic agent in a patient including the blood compartment at regular intervals over the residence time of the radionuclide.<sup>184,185</sup> This residence time can be several weeks depending on the physical and biological half-life of the radionuclide and targeting molecule respectively.

PET has a better diagnostic accuracy compared to SPECT because PET has a higher sensitivity (i.e., the ability to detect and record a higher percentage of the emitted events) than SPECT. SPECT needs physical collimators to reject scattered photons or photons that are not within a small angular range resulting in lower sensitivity.<sup>186</sup> The nature of positron annihilation allows the emission of two opposite annihilation photons at the

same event. Thus, physical collimators are not needed, but rather a coincidence-detection which allows a much larger angle of acceptance at each detector position, thereby significantly increasing the gain in sensitivity for PET. SPECT has more issues with artifacts and attenuation compared to PET.

The activity versus time profile from quantitative imaging is then integrated to arrive at the time-integrated activity (TIA) which will be used in radiation dose calculation as discussed in the following. Dosimetry for each treatment cycle is important as it will be used to plan the subsequent treatment cycle of fractionated radionuclide therapy: whether to give another cycle of the same activity, adjust the activity to be administered, or stop treatment if the planned dose threshold is reached.<sup>187,188</sup> Dosimetry is therefore used to track cumulative radiation dose to correlate with treatment response and normal organ toxicity.

## 2.2 Definition: Absorbed Dose

The absorbed dose,  $D$  is defined as the energy,  $dE$ , deposited by ionizing radiation in the target media of mass  $dm$  is given in Equation 2.1.

$$D = \frac{dE}{dm} \quad 2.1$$

The standard international (SI) unit of radiation dose is gray (Gy), defined as 1 Joule of energy absorbed per kilogram mass.<sup>189</sup>

Targeted radionuclide therapy absorbed dose calculations are used to assess the associated deterministic effect (for cancer cure) and stochastic risks (for radiation-induced cancer) as well as the efficacy of treatment (tumor dose).<sup>190</sup> Historically, the approach published by the Medical Internal Radiation Dose (MIRD) Committee in the 1960s is used to calculate absorbed doses.<sup>183,191</sup> For determining the absorbed dose to target organs, the general MIRD equation is

$$D(r_T) = \sum_S \tilde{A}(r_S) S(r_T \leftarrow r_S) \quad 2.2$$

where  $\tilde{A}(r_S)$  is the time-integrated activity of the radionuclide source and  $S(r_T \leftarrow r_S)$  also known as S-value is the dose deposited in the target  $r_T$  per unit of cumulated (time-integrated) activity in the source  $r_S$ .

Time-integrated activity is the total number of decays of a radionuclide source integrated over five times the effective half-life.<sup>192,193</sup> The effective half-life ( $T_e$ ) is defined as  $\frac{1}{T_e} = \frac{1}{T_p} + \frac{1}{T_b}$  where  $T_p$  refers to the physical half-life, and  $T_b$  to the biological half-life. The time-integrated activity  $\tilde{A}(r_S)$  is often normalized by the administered activity to form the time-integrated activity coefficient.<sup>192</sup> S-value is defined in Equation 2.3.

$$S(r_T \leftarrow r_S) = \sum_i \frac{n_i E_i \varphi_i(r_T \leftarrow r_S)}{m_T} \quad 2.3$$

where  $m_T$  is the mass of the target,  $n_i$  and  $E_i$  are the frequency and energy of each radiation type  $i$ , respectively, specifying the physical properties of the radionuclide, and  $\varphi_i(r_T \leftarrow r_S)$  is the absorbed fraction of energy emitted from the source that is deposited in the target for each radiation type emitted by the radionuclide of relevance.

## 2.3 Dose Calculation Method

The absorbed dose in targeted radionuclide therapy can be calculated using three methods: Organ S-value dosimetry, dose point kernel convolution and full Monte Carlo (MC) simulation.<sup>194,195</sup>

### 2.3.1 Organ S-value Dosimetry

The organ S-value method uses the MIRD formalism to estimate the average absorbed dose from internally distributed radionuclides in a volume of interest such as a whole organ or the tumor volume.<sup>196</sup> The absorbed dose of each organ is dependent on the physical properties of the radionuclide, the injected activity, and the kinetics of radioactivity uptake and clearance inside the tumor and normal tissue.<sup>196–198</sup> The average absorbed dose in the target organ,  $D(r_T)$  is calculated using Equation 2.4.

$$D(\mathit{organ}_T) = \sum_S \tilde{A}(\mathit{organ}_S) S(\mathit{organ}_T \leftarrow \mathit{organ}_S) \quad 2.4$$

where  $\tilde{A}(\mathit{organ}_S)$  is the average time-integrated (cumulative) activity of the source organ, and  $S(\mathit{organ}_T \leftarrow \mathit{organ}_S)$  is the average dose deposited in a target organ ( $\mathit{organ}_T$ ) per average cumulated activity in the source organ ( $\mathit{organ}_S$ ). Several dosimetry applications have been created using the MIRD formalism for dose calculation. The most extensively used organ-level dose software package is Organ Level Internal Dose Assessment/Exponential Modeling (OLINDA/EXM).<sup>199–201</sup> OLINDA/EXM allows inputs such as the organ time-integrated activity and organ-level S-values  $S(\mathit{organ}_T \leftarrow \mathit{organ}_S)$  to calculate the average absorbed dose for each organ. S-values is precalculated by Monte Carlo simulation in standard phantoms representing the average geometry/anatomy of male or female. In these simulations, activity is assumed to be uniformly distributed in source organs, and the dose is assumed to be uniformly deposited throughout each target organ which is also assumed to be uniform in its radiation interaction properties including density.<sup>193,202</sup>

The main drawback of the organ S-value method used in OLINDA/EXM is that a patient-specific absorbed dose estimate is not available since the  $\mathit{organ}_S$  values are based on standard phantoms rather than patient geometry/anatomy.<sup>193,203</sup> Specifically, by assuming uniform activity distributions, OLINDA/EXM can estimate dose in tumors in the form of uniform density spheres of varied sizes based on the organ S-value. This approach does not provide voxelized 3D dose distribution in tumors.<sup>204</sup>

Differences in mean absorbed doses estimated using OLINDA/EXM compared to doses computed using full Monte Carlo simulations based on patient CT scans have been reported as high as 31% for tumors and 97% for normal tissues in studies.<sup>205</sup> Researchers have extended the MIRD schema to calculate absorbed doses at the voxel level using voxel S-values (which is the same as dose point kernel convolution, §2.3.2) since organ-level dosimetry has limitations as discussed above.



### 2.3.2 Dose Point Kernel Convolution

Although MC simulation is the most accurate method for voxel-based absorbed dose calculations at the present, it is time-consuming, computationally expensive, and generally hard to implement.<sup>206,207</sup> As a result, numerous groups have proposed fast, voxel-based dosimetry methods based on dose point kernel (DPK) convolution or voxel S value (VSV) superposition techniques, which have been shown to overcome the limitations of the full MC method in clinical dosimetry.<sup>208,209</sup>

The dose-point kernel is the spatial distribution of absorbed dose around an isotropic point source of radiation in a homogeneous infinite medium, typically water.<sup>210–212</sup> Based on the principle of reciprocity, the superposition of VSV is the same as DPK convolution, therefore dose calculation using convolution (superposition) of DPK is the same as superposition (convolution) with VSV.<sup>204</sup>

A schematic diagram of DPK formalism and voxel S-value formalism is shown in Figure 2.1. DPK formalism distributes center pixel (0) energy to neighboring pixel (1 – 8). With an activity distribution, a superposition of DPK is required to calculate dose distribution.  $DPK(0 \rightarrow K)$  where  $K = 1$  to  $8$  is the fraction of center pixel energy deposited in pixel  $K$ . Voxel S value formalism distributes energy from neighboring pixel (1' – 8') to centre pixel (0').  $S(0' \rightarrow K')$  where  $K' = 1'$  to  $8'$  is the fraction of neighboring pixel energy that is deposited in center pixel 0'. With an activity distribution, a superposition of the voxel S value is required to calculate dose distribution.



**Figure 2.1:** (A) DPK formalism and (B) Voxel S value formalism in the distribution of energy from radionuclide.

Based on the patient-specific PET/SPECT images, the absorbed dose distribution is then determined by convolving the time-integrated activity distribution with the DPK or VSV calculated by MC simulation.<sup>204,213</sup> The voxel dose  $D_{voxel_j}$  (Gy) is given in Equation 2.5:

$$D_{voxel_j} = \tilde{A} \otimes DPK = \sum_{i=0}^n \tilde{A}_{voxel_i} \times DPK(voxel_i \rightarrow voxel_j) \quad 2.5$$

where  $D_{voxel_j}$  is the absorbed dose in  $j$ th target voxel,  $\tilde{A}_{voxel_i}$  is the time-integrated activity in the  $i$ th source voxel and  $DPK(voxel_i \rightarrow voxel_j)$  is the DPK in the  $j$ th voxel per unit decay in the  $i$ th voxel. The  $\tilde{A}_{voxel_i}$  value in each voxel can be derived from the PET or SPECT image (see §2.3.4).

### 2.3.3 Full Monte Carlo Simulation

The Monte Carlo (MC) simulation originated in Los Alamos in the 1940s when physicists working on particle transport problems began solving them using something which they termed the Monte Carlo method.<sup>214</sup> The MC method is a computational approach that uses random number sampling to perform numerical calculations of ionizing radiation interactions (transport) with matter. The MC dose calculation methods use general-purpose MC codes like Geant4, MCNP, EGSnrc, or EGS to model voxelized dose distributions within tumor, as well as in normal healthy tissues.<sup>215-219</sup>

To simulate radiation transport, MC codes leverage known physics of photon and particle interactions with tissue media.<sup>220</sup> MC simulations simulate ionizing radiation (photons and charge particles) traveling through a patient geometry (often referred to as a phantom) by using interaction cross-section data for different media (tissues).

The simulation procedure can be summarized as follows: A primary decay of ionizing radiation, sampled at the source, travels a certain distance, determined by the probability distribution based on the total interaction cross-section, to the site of a collision and scatters into another energy and/or direction, based on the differential cross-sections. The procedure is repeated until the ionizing radiation has been completely absorbed or has left the geometry under consideration. Any secondary particles (such as knock-on electrons

and bremsstrahlung photons) generated with significant kinetic energy are simulated as well. The energy deposited at each interaction site over the paths travel by both the primary and secondary radiation is tallied. In most MC codes, radiation (both primary and secondary) transport is performed down to an energy cutoff threshold of 1 keV or less. When the radiation reaches the cutoff energy threshold or is generated at or below this threshold, radiation transport stops. The estimated remaining energy is deposited at the stopping site in the phantom as low energy radiation below the cutoff threshold is unlikely to escape from the scoring region due to its short range.

The dose distribution in the phantom is derived from the total tallied dose normalized by all simulation histories or the total time-integrated activity over the entire phantom (discussed in §2.3.3.1). The statistical uncertainty of the calculation depends on  $N$ , the number of particle histories simulated and typically decreases with  $N^{-1/2}$ .<sup>221</sup> This may lead to long calculation times depending on the desired precision and/or the complexity and size of the geometry. The variance reduction technique is used to reduce the number of histories required to reach the same low uncertainties thereby increasing simulation efficiency.<sup>222</sup>

With SPECT or PET images providing quantitative information about the cumulated activity distributions, MC simulation can be used to simulate ionizing radiation transport in the body of a patient and calculate the resulting 3D dose distributions.<sup>210–212</sup> The simulation model can be set using patient-specific CT images, allowing the technique to account for patient-specific source and target organ anatomies as well as tissue inhomogeneities.<sup>193,223</sup>

Patient-specific dose estimate using full MC simulations is considered the potentially most accurate technique to predict radiation dose from targeted radionuclide therapy because full MC simulation accounts for heterogeneity in activity distribution in both the tumor and critical healthy organs, patient-specific anatomy and tissue inhomogeneity in density and composition (e.g. bone/calcifications vs soft tissue).<sup>208,224</sup> However, despite the availability of a wide range of MC codes, dosimetry treatment planning systems based on such codes have yet to achieve widespread acceptability in clinical practice

because MC dose calculation is computationally intensive and there is no convenient reference standard to validate the dose obtained.<sup>225,226</sup>

### 2.3.3.1 Interpretation of Dose Distribution from Monte Carlo Simulation

The dose distribution in a phantom using in Monte Carlo simulation method is given by Equation 1.6

$$D(x, y, z) = \frac{E(x, y, z)}{M(x, y, z)} = \sum_{k=1}^M \sum_{i,j=1}^N TIA(x_i, y_j, z_k) \frac{S(x_i \rightarrow x, y_j \rightarrow y, z_k \rightarrow z)}{M(x, y, z)} \quad 2.6$$

where  $D(x, y, z)$  is the dose (energy deposited,  $E(x, y, z)$ ) at voxel  $(x, y, z)$  from decays ( $TIA(x_i, y_j, z_k)$ ) at all  $(x_i, y_j, z_k)$ ,  $S(x_i \rightarrow x, y_j \rightarrow y, z_k \rightarrow z)$  is the energy deposited at  $(x, y, z)$  from a decay at  $(x_i, y_j, z_k)$ ,  $M(x, y, z)$  is the voxel mass.  $TIA(x_i, y_j, z_k)$  is related to the time activity,  $TA(x_i, y_j, z_k, t)$ , at time  $t$  as:

$$TIA(x_i, y_j, z_k) = \int_0^{\infty} TA(x_i, y_j, z_k, t) dt \quad 2.7$$

where  $\infty$  is the shorter of five biological or physical half-lives of the radionuclide at voxel  $(x_i, y_j, z_k)$ .

Dividing Equation 2.6 by the total TIA over all  $(x_i, y_j, z_k)$ , we have:

$$\frac{D(x, y, z)}{\sum_{k=1}^M \sum_{i,j=1}^N TIA(x_i, y_j, z_k)} = \sum_{k=1}^M \sum_{i,j=1}^N \frac{TIA(x_i, y_j, z_k)}{\sum_{k=1}^M \sum_{i,j=1}^N TIA(x_i, y_j, z_k)} \frac{S(x_i \rightarrow x, y_j \rightarrow y, z_k \rightarrow z)}{M(x, y, z)} \quad 2.8$$

The probability of decay at  $(x_i, y_j, z_k)$  can be estimated as:

$$P(x_i, y_j, z_k) = \frac{TIA(x_i, y_j, z_k)}{\sum_{k=1}^M \sum_{i,j=1}^N TIA(x_i, y_j, z_k)} \quad 2.9$$

Rewriting Equation 2.8 in terms of  $P(x_i, y_j, z_k)$  :

$$\frac{D(x, y, z)}{\sum_{k=1}^M \sum_{i,j=1}^N TIA(x_i, y_j, z_k)} = \sum_{k=1}^M \sum_{i,j=1}^N P(x_i, y_j, z_k) \frac{S(x_i \rightarrow x, y_j \rightarrow y, z_k \rightarrow z)}{M(x, y, z)} \quad 2.10$$

For Monte Carlo simulation with  $N_H$  histories, Equation 2.10 is modified as:

$$\begin{aligned} \frac{D(x, y, z)}{\sum_{k=1}^M \sum_{i,j=1}^N TIA(x_i, y_j, z_k)} \\ = \frac{1}{N_H} \sum_{k=1}^M \sum_{i,j,k=1}^N N_H P(x_i, y_j, z_k) \frac{S(x_i \rightarrow x, y_j \rightarrow y, z_k \rightarrow z)}{M(x, y, z)} \end{aligned} \quad 2.11$$

In Equation 2.11,  $\sum_{k=1}^M \sum_{i,j,k=1}^N N_H P(x_i, y_j, z_k) \frac{S(x_i \rightarrow x, y_j \rightarrow y, z_k \rightarrow z)}{M(x, y, z)}$  is the dose deposited in  $(x, y, z)$  for  $N_H$  histories while  $\frac{1}{N_H} \sum_{k=1}^M \sum_{i,j=1}^N N_H P(x_i, y_j, z_k) S(x_i \rightarrow x, y_j \rightarrow y, z_k \rightarrow z) = MC_{norm}(x, y, z)$  is the dose per decay or the normalized dose from the Monte Carlo simulation. If the simulation is correct,  $MC_{norm}(x, y, z)$  should be independent of the number of histories,  $N_H$ , used in the simulation. That is, mean  $MC_{norm}(x, y, z)$  should have zero bias, or it is independent of  $N_H$  but the standard deviation should increase with decreasing  $N_H$ .

Equation 2.11 also states that  $MC_{norm}(x, y, z)$  in Equation 2.12 is the dose at  $(x, y, z)$  divided by the total TIA. Thus, the voxel dose distribution,  $D(x, y, z)$ , is the normalized dose distribution from the Monte Carlo simulation,  $MC_{norm}(x, y, z)$ , multiplied by the summed TIA over all voxels. The voxel dose distribution divided by the summed TIA over all voxels is the normalized dose distribution from the Monte Carlo simulation.

$$MC_{norm}(x, y, z) = \frac{D(x, y, z)}{\sum_{k=1}^M \sum_{i,j=1}^N TIA(x_i, y_j, z_k)} = \frac{E(x, y, z)/M(x, y, z)}{\sum_{k=1}^M \sum_{i,j=1}^N TIA(x_i, y_j, z_k)} \quad 2.12$$

In summary, the 3D dose map produced by egs\_mird is:

$$\frac{1}{N_H} \sum_{i,j,k=1}^N N_H P(x_i, y_j, z_k) S(x_i \rightarrow x, y_j \rightarrow y, z_k \rightarrow z)$$

in units of Gy per decay. To convert to more convenient units of  $\mu Gy(GBq \cdot s)^{-1}$ , the voxel values have to be scaled by  $10^{15}$ . For DVH generated with egs\_mird 3D dose after it has been scaled by  $10^{15}$ , the horizontal axis is in units of  $\mu Gy(GBq \cdot s)^{-1}$ .

The egs\_mird dose calculation is based on the probability distribution,  $P(x_i, y_j, z_k)$ . As shown in Equation 2.8:

$$P(x_i, y_j, z_k) = \frac{TIA(x_i, y_j, z_k)}{\sum_{k=1}^M \sum_{i,j=1}^N TIA(x_i, y_j, z_k)}$$

### 2.3.4 Quantification of Time-Integrated Activity from PET/SPECT Images

The activity of radioactive materials measures the number of radioactive decay that occur per unit of time. According to the International System of Units (SI), the unit for activity is the Becquerel (Bq), defined as one disintegration (decay) per second, and is measured in reciprocal seconds ( $s^{-1}$ ). The older standard, the curie (Ci), is still in common usage and  $1 \text{ Ci} = 3.7 \times 10^{10} \text{ Bq}$ .

The radiolabelled molecule (or radiopharmaceutical) is injected intravenously into a patient's bloodstream to assess disease extent (diagnosis), TRT treatment planning and dosimetry. For these purposes, especially dose calculation, the distribution of activity concentrations (Bq/mL) in the tumor and organs and tissues of individual patients has to be determined.<sup>227</sup> In quantitative nuclear medicine, SPECT and PET are used to visualize

the distribution of radiopharmaceuticals in a patient's body and to determine the absolute activity concentration of the radiopharmaceutical.

where  $C_T$  is the count rate (counts per unit time (cps)) in the phantom as measured by the PET or SPECT scanner and  $A_T^c$  is the actual activity concentration in the phantom. Both count rate and activity concentration are corrected for radioactive decay at the same time of measurement.

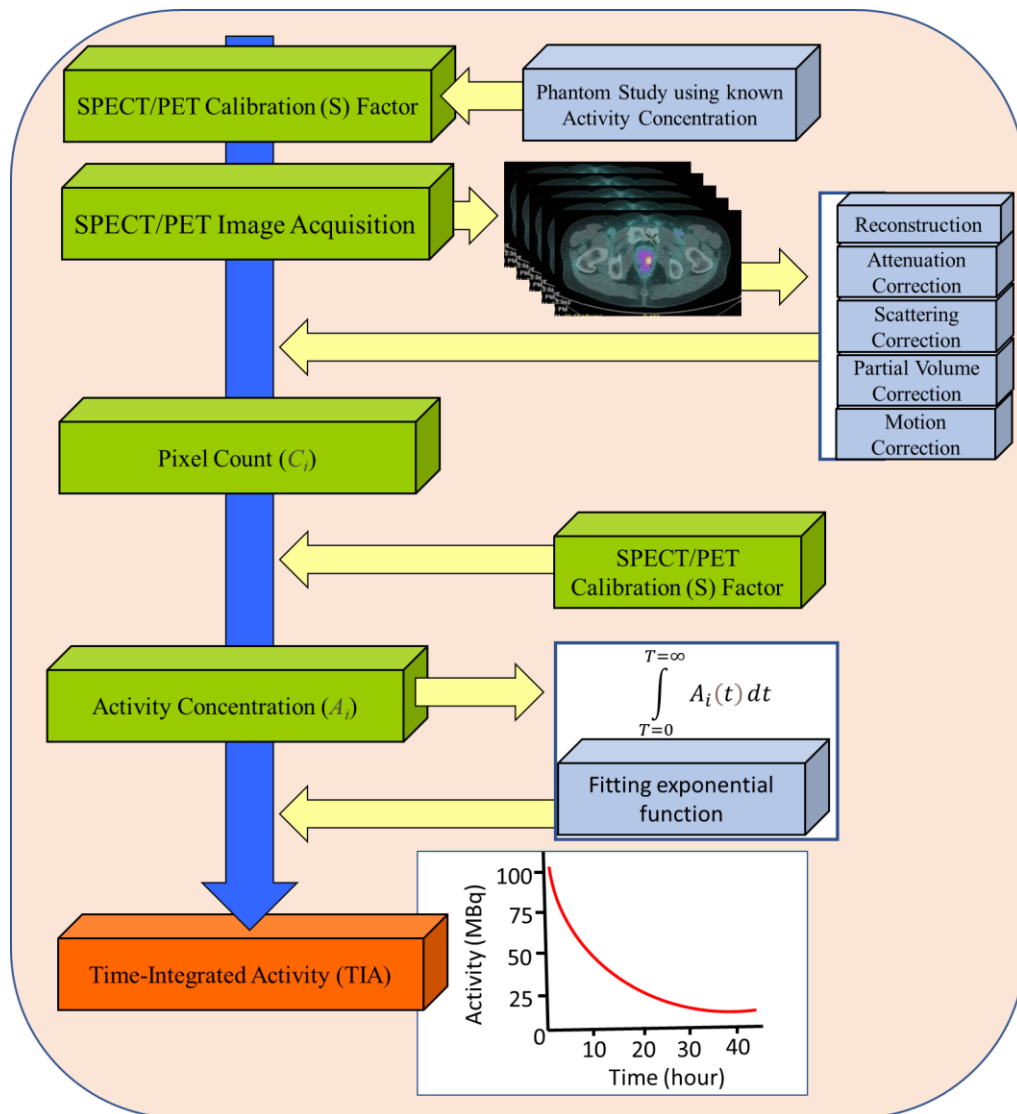


**Figure 2.2:** Time-integrated activity quantification workflow

To determine the time-integrated activity following a radiopharmaceutical injection, SPECT or PET images are acquired at different time intervals. Because PET and SPECT images are affected by attenuation, scatter, and patient motion, they have to be corrected for these effects first. The corrected image pixel values (count rate) are then converted into activity concentration via the pre-determined calibration factor according to the formula in Equation 2.14.<sup>228</sup>

$$A_i^c = \frac{C_i}{S} \quad 2.13$$

where  $C_i$  and  $A_i^c$  are the corrected image pixel value and activity concentration at  $i$ th pixel respectively and  $S$  is the scanner calibration factor. The voxel volume,  $\Delta v$ , is used to convert activity concentration into activity at the  $i$ th pixel shown in Equation 2.13.

$$A_i = A_i^c \Delta v \quad 2.14$$

Since radiopharmaceuticals take time to decay or to be cleared from the tumor and tissues, SPECT or PET studies are acquired at different times after injection. Since decay and many clearance processes are exponential in nature, multiexponential functions are widely used to fit time activity curve data derived from sequential PET and SPECT images following radiopharmaceutical injection.

The cumulated (or time-integrated) activity (in units of Bq.s) is defined as the integral of the activity over time. The time-integrated activity can be determined by fitting the measured data to a summation of exponential terms or another mathematical function that can be integrated analytically. In dynamic PET, B-splines have been proposed for estimating activity using parametric estimation.<sup>229</sup> This fitting method can also be applied to SPECT imaging. For the spline method, the time-integrated activity was calculated using Equation 2.16.

$$\tilde{A}_s = \int_0^T A(t) dt + \int_T^\infty A_f e^{-\lambda t} dt \quad 2.15$$



where  $\tilde{A}_s$  is the time-integrated activity,  $A(t)$  is the spline fitted time-activity curve at which imaging was terminated,  $A_f$  is the activity of the organ at the end of the last PET or SPECT scan,  $\lambda$  is the decay rate constant of the radionuclide and  $T$  is the time at which sequential imaging was terminated.

Ahkvanallaf et al<sup>198</sup>, using a Siemens Biograph mCT hybrid PET/CT scanner, imaged patients after intravenous injection of <sup>18</sup>F-FDG tracer. PET images of the patients were acquired at 13-time points. The time-integrated activity was calculated by integrating voxelwise time activity curves over 13-time points within the dynamic PET frames using Equation 2.17:

$$\tilde{A}_s = \sum_{i=0}^{13} (A_i + A_{i+1}) \cdot \Delta t_i + \int_T^{\infty} A_f e^{-\lambda t} dt \quad 2.16$$

where  $\tilde{A}_s$  is the cumulated activity,  $A_i$  is the activity obtained from the images pixel at the  $i$ th time frame,  $A_f$  is the activity concentration in the last time point of measurement,  $\lambda$  is the decay rate constant of the radionuclide and  $T$  is the bladder voiding time.

## 2.4 Thesis Objectives and Outline

The objective of this thesis is two folds. Firstly, to validate an `egs_mird` (an in-house MC simulation code) program and see if it agrees with itself and well-established MC codes. Secondly, to develop a 3D voxel-level dose point kernel convolution method and investigate whether it is accurate for patient-specific TRT dosimetry in prostate cancer.

### 2.4.1 Chapter 3: `egs_mird` MC code validation

To validate `egs_mird`, both internal and external consistency tests were performed. The internal consistency test measures the agreement between various simulations computed using `egs_mird` while the external consistency test assesses the correlation between the same simulation but calculated using different MC codes. In the internal consistency tests, `egs_mird` is used to calculate energy deposition in DPKs of different voxel sizes and the results are compared with the theoretical calculation. While in the external

consistency tests, the DPKs for different radionuclides generated by `egs_mird` are compared against those obtained by different MC codes published in the literature.

#### 2.4.2 Chapter 4: Three-dimensional Voxel-level Dose Point Kernel Convolution Code

The validation of the 3D voxel-based DPK convolution code is presented. This chapter introduces the 3D voxel-based DPK convolution code developed in my research and investigates whether it is accurate in comparison to MC simulation for patient-specific dosimetry in prostate cancer using the time-integrated activity (TIA) distribution from a diagnostic dynamic PET [ $^{18}\text{F}$ ]DCFPyL or [ $^{18}\text{F}$ ]FCH study to approximate that of [ $^{177}\text{Lu}$ ]PSMA-617 used in TRT.

#### 2.4.3 Chapter 5: Conclusion and Future Direction

Chapter 5 contains the thesis summary, a discussion of how tissue density inhomogeneities affect the DPK convolution result, and future directions. The future direction will account for tissue inhomogeneities, estimate the biological effective dose (BED) and the time-integrated activity.

## Chapter 3

### 3 egs\_mird Validation

Monte Carlo (MC) codes such as GEANT4 and GATE have been used for targeted radionuclide therapy dosimetry. However, their dose calculations are based on assumptions about patient geometry (uses reference phantoms to model patient geometry) and activity distribution.<sup>208,230–232</sup> Thus, we developed egs\_mird to calculate a patient-specific absorbed dose distribution in targeted radionuclide therapy using individual patient CT for the definition of patient geometry and density distribution and PET or SPECT scans for integrated time activity distribution.<sup>233</sup> This chapter introduces egs\_mird MC code and validates it using both internal and external consistency test.

#### 3.1 egs\_mird Monte Carlo Code

egs\_mird is an egs++ application developed from the EGSnrc MC code that scores dose in a 3D array and outputs the result in an EGSnrc .3ddose file. EGSnrc MC code toolkit is used to simulate the transport of ionizing radiation through matter. With the egs\_mird MC code, ionizing radiation emitted by radionuclides (such as photons, electrons, and positrons) is simulated in a patient geometry defined by CT for density and tissue type (media). egs\_mird takes certain input files similar to EGSnrc application for its simulation. egs\_mird input file is conveniently saved as Filename.egsinp.

##### 3.1.1 egs\_mird Monte Carlo Code

This section offers a brief description of the various components of the input files that egs\_mird requires. egs\_mird input files are identical to that of other egs++ applications.<sup>234</sup> In all cases, the input blocks start and end with :start and :stop delimiter statements. For example:

```
:start some input:  
    my_inputs (one or more lines)  
:stop some input:
```

The `egs_mird` input blocks that are commonly required are run control, media definition, phantom geometries, source definition, scoring options, variance reduction, and MC transport parameters.

### 3.1.1.1 Run Control

The `:start run mode:` block of the input file specifies how many histories to run (`ncase`) and additionally, `nbatch`, `nchunk` if needed. EGSnrc applications divide simulations into `nchunk` 'chunks,' which are beneficial during parallel runs because they allow for a better balance of computation time on each computer, even if their speeds are considerably different. By default, `nchunk=1` for simple runs with no parallelization, and `nchunk=10` for parallel runs. The job is broken into `ncase/(npar*nchunk)` 'chunks' of history for parallel runs, where `ncase` is the total number of histories to be done in parallel on `npar` machines. When jobs from different 'chunk' are completed, they are combined. Thus, faster machines can run more 'chunks' in this manner. The input block run control is specified as:

```
:start run control:
      ncase      = 100000000
      nbatch     = 1
:stop run control:
```

### 3.1.1.2 Media Definition

It requires a `:start media definition:` input block which inputs the values of `AE`, `UE`, `AP` and `UP`. The lower and upper energy thresholds of charged particles are denoted by `AE` and `UE`, respectively. `AP` and `UP` are used to represent the lower and upper energy thresholds of photons, respectively. Another input in the media definition is materials defined in the `material.dat` file. The `material.dat` file contains tissue media composition with their densities. The media definition is defined as, for instance:

```
:start media definition:
      AE = 0.512
      UE = 2.012
      AP = 0.001
      UP = 1.500
      material data file = material.dat
:stop media definition:
```

The material.dat file is specified as:

```
medium = Prostate
rho = 1.040
elements = H, C, N, O, NA, P, S, CL
mass fractions = 0.105, 0.089, 0.025, 0.774, 0.002, 0.001, 0.002,
0.002
bremsstrahlung correction = NRC
```

### 3.1.1.3 Geometry Definition

This block tells egs\_mird which geometry (phantom) to score dose in. The phantom geometry in 3D can be user-defined or patient-specific geometry derived from the CT images. Patient-specific CT densities are stored in egsphant file. The :start geometry definition: input block takes input values from information contained in the material.dat file (defining the tissue media and densities) specified in the media definition block. For example, a user-defined 3D geometry is defined as:

```
:start geometry definition:
  :start geometry:
    library = egs_ndgeometry
    type    = EGS_XYZGeometry
    name    = phantom
    x-planes = -10 -9 -7 -5 -3 -1 1 3 5 7 9 10
    y-planes = -10 -9 -7 -5 -3 -1 1 3 5 7 9 10
    z-planes = -10 -9 -7 -5 -3 -1 1 3 5 7 9 10
    :start media input:
      media = Prostate
    :stop media input:
  :stop geometry:
  simulation geometry = phantom
:stop geometry definition:
```

Patient-specific geometry is defined as:

```
:start geometry definition:
  :start geometry:
    library      = egs_glib
    type         = egsphant
    name         = phantom
    egsphant file = FileName.egsphant
    density file = material.dat
  :stop geometry:
  simulation geometry = phantom
:stop geometry definition:
```

### 3.1.1.4 Source Definition

The `:start source definition:` input block specifies the required information about the radioactive sources used for TRT. `egs_mird` uses `egs_internal_source` and `egs_radionuclide_source` for its source definition. `egs_internal_source` takes two inputs: a rectilinear patient geometry (i.e., a patient is defined as a 3D grid of voxels with the appropriate media and densities) and a list of voxel regions with corresponding time-integrated activity (TIA). The list of regions and weight is created into a table that can be sampled at  $O(1)$  efficiency using the alias technique already provided in EGSnrc as the class EGS AliasTable: (i.e., EGS AliasTable samples at the same rate regardless of table size). To determine where to generate the particle, two random numbers are used. Consequently, if a user has a heterogeneous TIA distribution over a patient geometry, they can utilize it in the patient simulation. The `egs_radionuclide_source` is an `egs++` source class that can simulate the decay (decay chain) of a variety of radionuclides used in TRT (e.g.,  $^{177}\text{Lu}$ ,  $^{90}\text{Y}$ ,  $^{131}\text{I}$ ,  $^{223}\text{Ra}$ , and  $^{225}\text{Ac}$ ).<sup>233</sup> Because EGSnrc is unable to simulate alpha transport, all alpha particles generated in decay are considered to deposit their energy locally.

Additionally, `egs_mird` also allows simulation with monoenergetic ionizing radiation sources. To implement this, within the `:start source definition:` input block there is a nested input block called `:start source:` which specifies the charge such as 0, -1, and 1 for photons, electrons and positrons respectively. The energy spectrum of the source must be specified in a `:start spectrum:` nested block. This spectral input is monoenergetic, with the energy set (in MeV).”

### 3.1.1.5 Scoring Options

The `:start scoring options:` input block specifies the geometry to score dose, the output filetype and filename. For example, the input block of the scoring option is defined as:

```
:start scoring options:
    type          = 3ddose
    file name     = fileName.3ddose
    scoring geometry = phantom
:stop scoring options:
```

### 3.1.1.6 Variance Reduction

The `:start variance reduction:` is used to turn on variance reduction techniques. The variance reduction is an optional input block in `egs_mird` that allows the user to enable tracklength scoring and choose a data file containing the energy absorption coefficient ( $\mu_{en}$ ) data used in the calculation. The `:start variance reduction:` block is defined as:

```
:start variance reduction:
    score tracklength dose = yes
    muen file               = XCOM_muen_1500keV.muendat
:stop variance reduction:
```

A photon tracklength estimator is a variance reduction technique based on the premise that all electrons deposit their energy locally at low photon energies, allowing the dose to be approximated as collision kerma.<sup>233,235</sup> It requires setting the electron transport cutoff to the maximum energy, implying that no electrons are transferred during the simulation and instead deposit their energy locally when formed. A photon traveling through a volume is counted as a dose deposition event when employing tracklength scoring. Using the total tracklength across the volume ( $t$ ), the appropriate mass-energy absorption coefficient ( $\mu_{en}/\rho$ ) and the energy of the travelling photon ( $E$ ), the dose deposited in this event ( $D_e$ ) to the scoring volume ( $V$ ) may be calculated using Equation 3.1.

$$D_e = \frac{t \cdot E \cdot \mu_{en}/\rho}{V} \quad 3.1$$

A large increase in simulation efficiency can be realized by scoring dose along a photon's track rather than in individual interaction events; even though a single photon history using tracklength scoring takes longer to compute, the total number of histories required to attain low uncertainties can be greatly reduced. The `egs_mird` application and `egs_internal_source` are available at the [https://github.com/Robarts-Lee-Lab/egs\\_mird](https://github.com/Robarts-Lee-Lab/egs_mird) website and `egs_radionuclide_source` is available as a pull request on the main EGSnrc github page at <https://github.com/nrc-cnrc/EGSnrc>.

## 3.2 Methods

To validate `egs_mird`, both internal and external consistency tests were performed. The internal consistency test measures the agreement between various simulations computed using `egs_mird` while the external consistency test assesses the correlation between the same simulation but calculated using different MC codes. In the internal consistency test, `egs_mird` was used to calculate dose point kernels (DPKs) at different voxel sizes and the energy deposition is compared with the energy of the radionuclide source. While in the external consistency test, the DPKs generated by `egs_mird` are compared against DPKs obtained by different MC codes published in the literature.

### 3.2.1 Internal Consistency Test

The `egs_mird` MC code was used to generate the DPKs of  $^{177}\text{Lu}$  and two ‘fake’ radionuclides one emits a monoenergetic photon of energy 120 keV and 500 keV. Another emits monoenergetic electrons of energy 500 keV at a voxel resolution of  $1 \times 1 \times 1 \text{ mm}^3$  and  $2 \times 2 \times 2 \text{ mm}^3$ . Energy deposition in different volumes was calculated by summing the corresponding DPK values and then scaling the summation by the voxel mass. The internal consistency tests consisted of testing for energy conservation in three different ways. First, the energy deposited by  $^{177}\text{Lu}$  in volumes of different sizes as evaluated from the DPK generated by `egs_mird` using different voxel resolutions was compared; second, the total energy deposited by  $^{177}\text{Lu}$  was evaluated as the summation of all (non-zero) DPK values scaled by the voxel mass was compared with the total energy emitted from a single decay of the radionuclide which has a spectrum of energy emissions, third, energy conservation is also tested for the two ‘fake’ radionuclides with monoenergetic photon and electron emission respectively.

For the first energy conservation test, DPK simulation was performed using  $^{177}\text{Lu}$  as the radionuclide source. A schematic diagram of the simulation phantom is shown in Figure 3.1. The simulation phantom  $20 \times 20 \times 20 \text{ cm}^3$  in size consisted of prostate media with a density of  $1.03 \text{ g/cm}^3$ . with `egs_mird` at a voxel resolution of  $1 \times 1 \times 1 \text{ mm}^3$  and  $2 \times 2 \times 2 \text{ mm}^3$ .



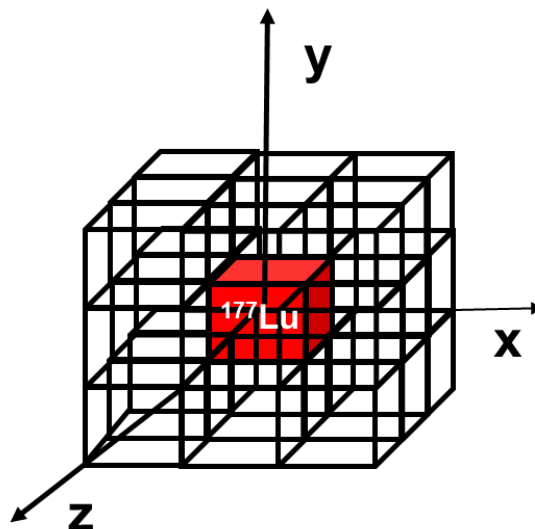


**Figure 3.1:** Schematic diagram of DPK phantom. The source,  $^{177}\text{Lu}$  radionuclide source was positioned at the center voxel. The DPK phantom was filled with prostate media with a density of  $1.03 \text{ g/cm}^3$ .

For the second energy conservation test, the total energy on average emitted from a  $^{177}\text{Lu}$  decay cannot be accurately calculated theoretically from its decay due to characteristic X-ray emission and Auger emission cascades ( $K\alpha$ ,  $K\beta$ ,  $KLX$ ,  $KXY$ ) are cited in probabilities and have a range of energies, Instead, egs\_mird was used to calculate the  $^{177}\text{Lu}$  DPK with all transport processes turned off and the energy deposited at the center voxel was taken as the (average) energy emitted by a single decay of  $^{177}\text{Lu}$  radionuclide. The  $^{177}\text{Lu}$  decay scheme is available at <http://www.nucleide.org/DDEPWG/DDEPdata.htm>.

For the final test of energy conservation, DPKs of 500 keV monoenergetic electron and photon of energy 500 keV and 120 keV in a phantom of either  $65 \times 65 \times 65 \text{ cm}^3$  or  $100 \times 100 \times 100 \text{ cm}^3$ .

All DPK simulations in the internal consistency tests used the default EGSnrc transport parameters: Compton scattering, Rayleigh scattering, and electron impact ionization switched on, pair angular sampling was set to off, and bremsstrahlung cross sections set to 'NIST'. DPK simulations were performed with  $3 \times 10^9$  decays (histories) without

employing variance reduction techniques. Electrons and photons were transported with a cutoff kinetic energy of 1 keV.

### 3.2.2 External Consistency Test

A 3D DPK for the three radionuclide sources ( $^{90}\text{Y}$ ,  $^{131}\text{I}$  and  $^{177}\text{Lu}$ ) were calculated using the egs\_mird MC code and compared to those calculated with general-purpose MC codes: DOSXZnrc, EGS4, MCNP4C, GEANT4 and vxIPen (application developed using PENELOPE) found in literature.<sup>213,236</sup>

The transport of electrons and photons emitted by radionuclide sources are simulated in a homogenous medium of soft tissue according to the Cristy and Eckermann elemental composition shown in Table 3.1.<sup>237</sup>

**Table 3.1:** Cristy and Eckermann's elemental composition.<sup>237</sup>

Element	Percentage by weight
H	10.454
C	22.663
N	2.490
O	63.525
Na	0.112
Mg	0.013
Si	0.030
P	0.134
S	0.204
Cl	0.133
K	0.208
Ca	0.024
Fe	0.005
Zn	0.003
Rb	0.001
Zr	0.001
Pb	0.001
Density	1.400 g/cm <sup>3</sup>

The deposited energy is scored in cubic voxels with a voxel resolution of 3 mm in phantom size of 16.5 x 16.5 x 16.5 cm<sup>3</sup> for  $^{90}\text{Y}$  and  $^{131}\text{I}$  and in cubic voxels of 4 mm

resolution in phantom size of 43.6 x 43.6 x 43.6 cm<sup>3</sup> for <sup>177</sup>Lu source. The DPK simulations were implemented using `egs_internal_source` and `egs_radionuclide_source`. The radionuclide source was placed at the center voxel of each phantom in 3D Cartesian geometry. The energy and frequency of emissions of the radionuclide sources were obtained from the Brookhaven National Laboratory database available at <http://www.nucleide.org/DDEPWG/DDEPdata.htm>.

All simulations used the default EGSnrc transport parameters: Compton scattering, Rayleigh scattering, and electron impact ionization switched on, pair angular sampling was set to off, and bremsstrahlung cross sections set to 'NIST'. DPK simulations were performed with  $2.5 \times 10^7$  decays (histories) without employing variance reduction techniques. Electrons and photons were transported with a cutoff kinetic energy of 1 keV. The `egs_mird` <sup>131</sup>I and <sup>90</sup>Y DPK results were compared to DOSXZnrc, EGS4, MCNP4C, GEANT4 found in a literature whereas <sup>177</sup>Lu DPK result was compared to `vxIPen` found in another literature.<sup>213,236</sup> The absorbed dose scored in each voxel was normalized in units of mGy.MBq<sup>-1</sup>.s<sup>-1</sup>.

### 3.3 Results

Here results of external and internal consistency tests of `egs_mird` are presented. In general, for the internal consistency tests, `egs_mird` passed the three energy conservation tests; for the external consistency tests, `egs_mird` DPKs for <sup>90</sup>Y, <sup>131</sup>I and <sup>177</sup>Lu agree with those generated by other MC software packages.

#### 3.3.1 Internal Consistency Test

Figure 3.2 shows the DPK of <sup>177</sup>Lu radionuclide generated by `egs_mird` for 1 mm and 2 mm voxel resolution. In Table 3.2, the energy deposition profile in volumes of 1 – 125 cm<sup>3</sup> calculated from 1 mm voxel resolution DPK overlaps with that calculated from 2 mm voxel resolution DPK, showing good agreement or energy is conserved independent of voxel resolution used in the generation of DPK.

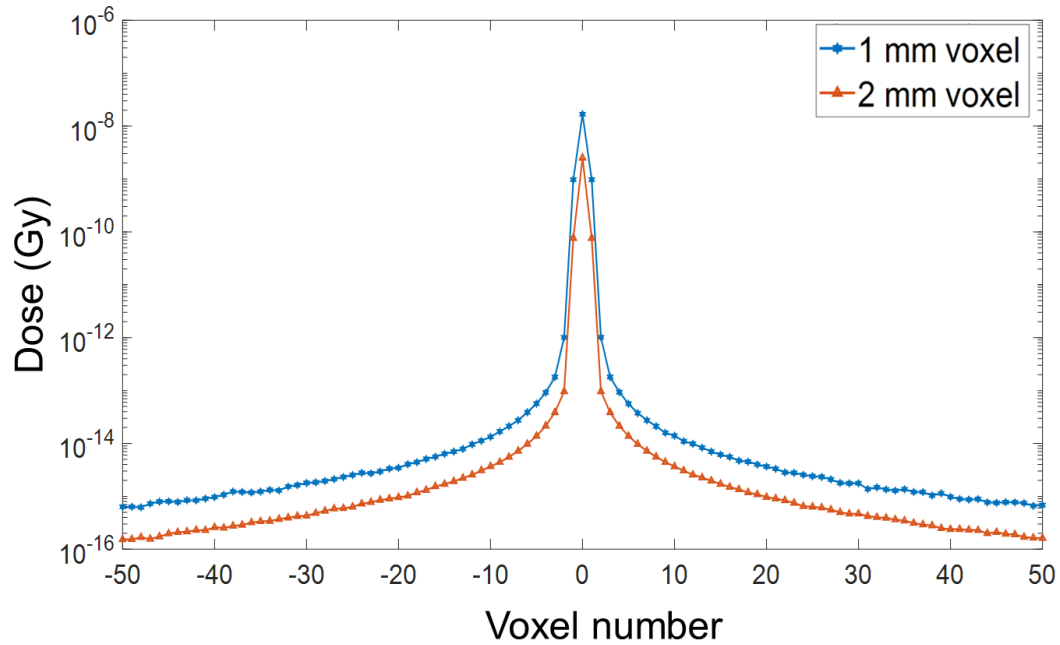


**Figure 3.2:**  $^{177}\text{Lu}$  DPKs generated with `egs_mird` for 1 mm (in blue) and 2 mm (in red) voxel resolution.

As shown in Table 3.3, the total energy deposition from a  $^{177}\text{Lu}$  radionuclide source estimated from 1 mm and 2 mm voxel resolution DPK shown in Figure 3.2 was essentially identical to that obtained from a simulation with no radiation transport so that all energy is deposited at the center voxel where the source was situated.

**Table 3.2:** Energy deposition profile of  $^{177}\text{Lu}$  in volumes of different sizes as estimated from DPK of 1 mm and 2 mm voxel resolution.

Volume (cm <sup>3</sup> )	1 mm	2 mm
	Energy (J/decay)	Energy (J/decay)
1	$2.52 \times 10^{-14}$	$2.52 \times 10^{-14}$
8	$2.53 \times 10^{-14}$	$2.53 \times 10^{-14}$
27	$2.56 \times 10^{-14}$	$2.56 \times 10^{-14}$
64	$2.60 \times 10^{-14}$	$2.60 \times 10^{-14}$
125	$2.63 \times 10^{-14}$	$2.63 \times 10^{-14}$

**Table 3.3:** egs\_mird Monte Carlo simulation using 1 mm and 2 mm voxel resolution of total energy deposition from a  $^{177}\text{Lu}$  radionuclide source. For comparison, energy deposited for a simulation with no transport is also included.

egs_mird DPK simulation	Energy (J/decay)
1 mm voxel	$2.7057 \times 10^{-14}$
2 mm voxel	$2.7064 \times 10^{-14}$
No transport	$3.0202 \times 10^{-14}$

Simulations of total energy deposition from monoenergetic 120 keV and 500 keV photons and 500 keV monoenergetic electrons with voxel dimensions of  $0.976 \times 0.976 \times 3.51 \text{ mm}^3$  in two different phantom sizes and with and without radiation transport are summarized in Table 3.4. In each case, the percentage difference of total deposited energy in the phantom relative to the reference energy of either the monoenergetic electron or photon was calculated and listed in Table 3.4.

**Table 3.4:** Simulations of total energy deposition of monoenergetic 120 keV and 500 keV photon and monoenergetic 500 keV electron in  $(65 \text{ cm})^3$  and  $(100 \text{ cm})^3$  phantom sizes.

Transport simulated	Total energy deposited (keV)	Energy diff (%)
Monoenergetic 500 keV photon in a $65 \times 65 \times 65 \text{ cm}^3$ phantom		
Photon transport	438.6	-12.3
No photon transport	500	0
Monoenergetic 500 keV electron in a $65 \times 65 \times 65 \text{ cm}^3$ phantom		
Electron transport	500	0
No electron transport	500	0
Monoenergetic 120 keV photon in a $65 \times 65 \times 65 \text{ cm}^3$ phantom		
Photon transport	114.9	-4.2
No photon transport	120.0	0
Monoenergetic 120 keV photon in a $100 \times 100 \times 100 \text{ cm}^3$ phantom		
Photon transport	119.5	-0.4
No photon transport	120.0	0

### 3.3.2 External Consistency Test

Soft tissue DPKs for  $^{90}\text{Y}$ ,  $^{131}\text{I}$ , and  $^{177}\text{Lu}$  was estimated with egs\_mird. Comparisons of egs\_mird DPKs with those from literature in Figure 3.3 to Figure 3.5 show good agreement. The percentage difference (PD) of DPK values at the same distance from the source was determined for each DPK profile using Equation 3.2.

$$PD(i) = \frac{Da(i) - Db(i)}{Da(i)}, \quad i = 0, \dots, n \quad 3.2$$

where  $Da$  is the reference EGS4 DPK value,  $Db$  is the DPK value from other MC codes and  $i$  is the source-target voxel distance.  $i = 0$  corresponds to the center voxel and  $i = 1, \dots, n$  corresponds to the distance away from the source (center). For  $^{90}\text{Y}$  in Figure 3.3, egs\_mird had a 4% dose difference, DOSXYZnrc 11%, MCNP4C and GEANT4 2% for the center voxel. At distance  $>6$  mm, consistent differences in dose are observed for a mean dose difference of 52% for egs\_mird, 50% for MCNP4C, 56% for DOSXYZnrc, and 47% GEANT4. The same comparison is reported for  $^{131}\text{I}$  in Figure 3.4. At the center voxel, the difference reaches -3% for egs\_mird, 10% for DOSXYZnrc, 4% for MCNP4C, and 4% for GEANT4. At larger distances greater than 4 mm, differences are scattered between -4% and 19% for egs\_mird, 0% and 24% for DOSXYZnrc, -11% and 12% for MCNP4C, and -11% and 12% for GEANT4.

Figure 3.5 shows the soft tissue DPK of  $^{177}\text{Lu}$  calculated with egs\_mird and vxlPen profiles. In this case, the percentage dose difference comparison was carried out using vxlPen as the reference. Results show good agreement at source distance greater than 4 mm with less than 0.004% dose deviation, except for the center voxel where it is 9.96%, shown in Figure 3.5.

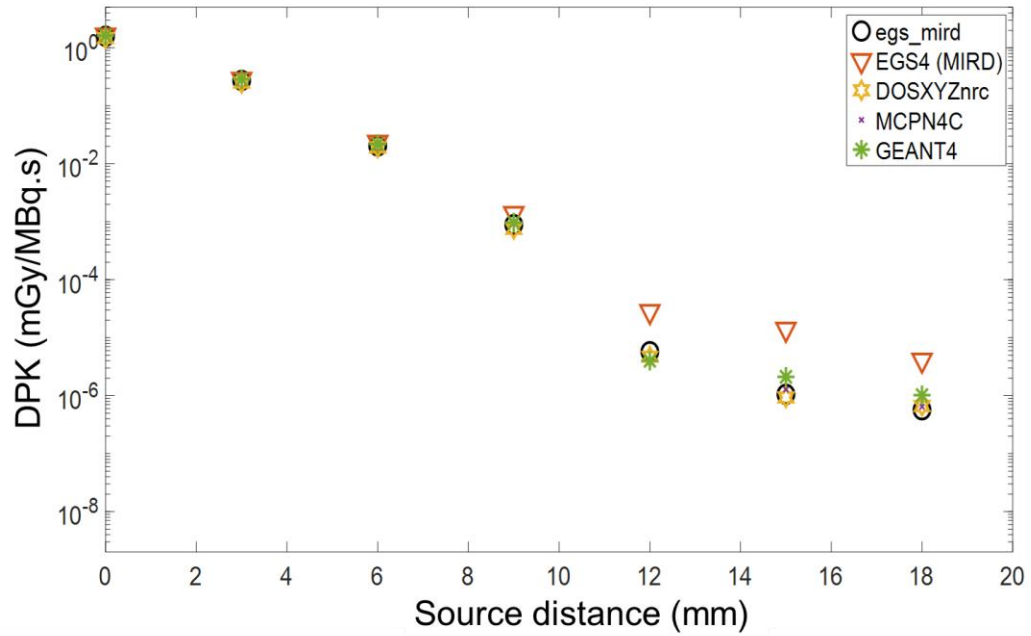


**Figure 3.3:** Comparison of  $^{90}\text{Y}$  DPKs generated using egs\_mird (black circle) to other DPKs from the literature.

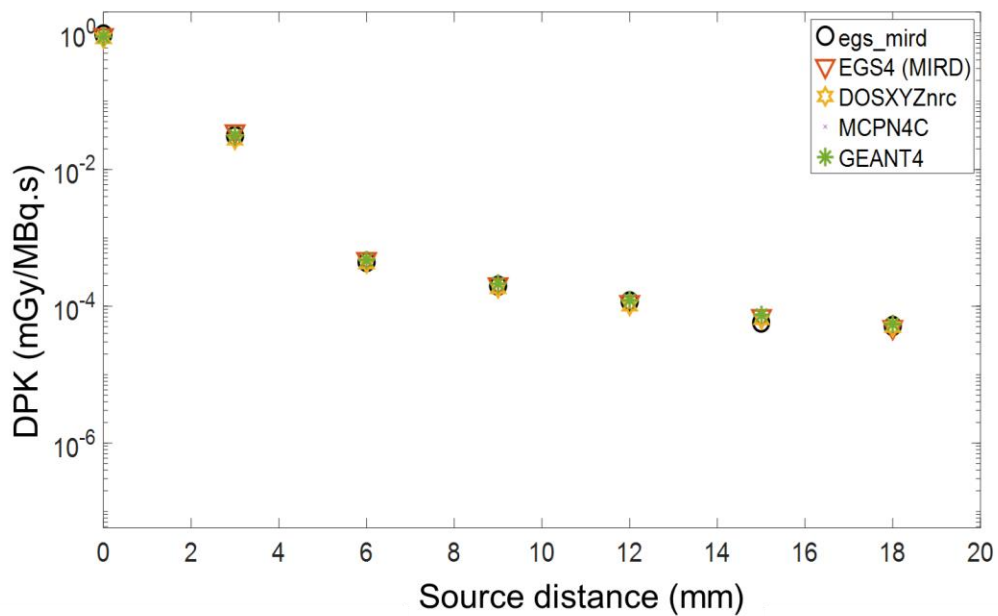


**Figure 3.4:** Comparison of  $^{131}\text{I}$  DPKs generated using egs\_mird (black circle) to other DPKs from the literature.

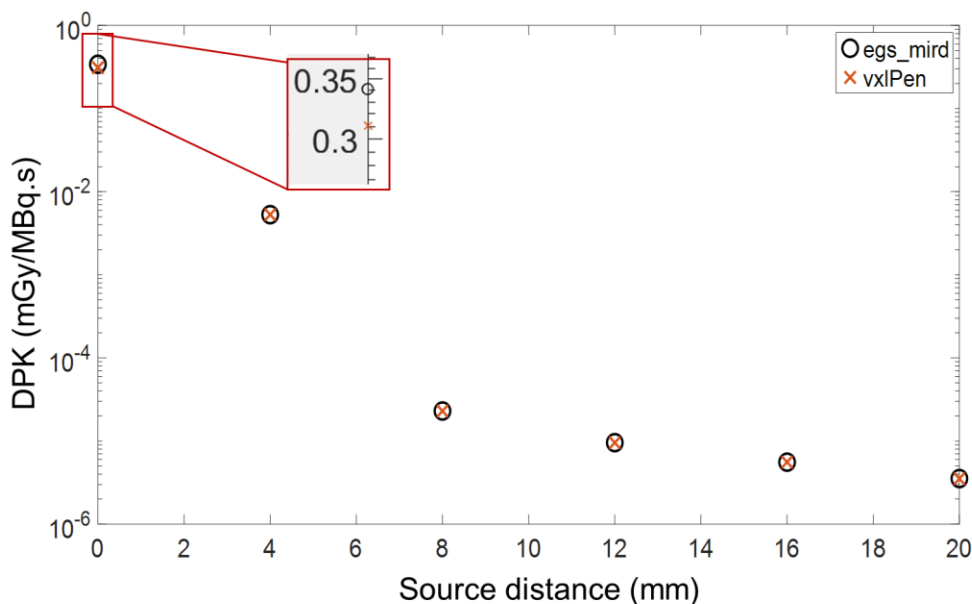


**Figure 3.5:** Comparison of  $^{177}\text{Lu}$  DPKs generated using `egs_mird` (black circle) to other DPKs from the literature. A magnified scale of the DPK profile at the center voxel is shown.

### 3.4 Discussion

The validity of `egs_mird` Monte Carlo code for targeted radionuclide therapy dosimetry was investigated by checking the internal consistency of `egs_mird` results with respect to energy conservation at different phantom voxel resolutions. Figure 3.2 shows that the  $^{177}\text{Lu}$  DPK expressed in voxel number distance from the source voxel at 1 mm voxel resolution is always higher than 2 mm voxel resolution. As dose is the quotient of the energy deposited in a target voxel and the mass of the voxel. Thus, the discrepancies in the DPKs shown in Figure 3.2 can be explained by the difference in voxel mass. The `egs_mird` Monte Carlo simulation of total energy deposition by  $^{177}\text{Lu}$  derived from 1 mm and 2 mm resolution DPK were in good agreement. Furthermore, the energy deposited was in agreement with that from a simulation with no radiation transport. Monoenergetic photons and electrons were used to further investigate the energy deposition in the DPK volume to further validate the `egs_mird` Monte Carlo simulation code according to energy conservation. The 120 keV monoenergetic photons simulation with radiation transport for



both 65 cm x 65 cm x 65 cm and a 100 cm x 100 cm x 100 cm DPK volume showed a significant decrease in energy deposition in the DPK volume, 12.27% and 4.22% respectively with respect to the energy of the monoenergetic photon due to energy escape from the phantom. As expected, since the escape of secondary radiation was less, the decrease in energy deposition was less in the larger phantom. Electron interaction is vastly different from photons. The energy deposition in the DPK volume for electron simulation showed good agreement with the energy of the monoenergetic electron with and without particle transport because a 500 keV electron travels only 1.78 mm in soft tissues before it is completely stopped. The electron range in soft tissue was calculated using the ESTAR program available at <https://physics.nist.gov/PhysRefData/Star/Text/ESTAR.html>.

In the external consistency tests, DPK for  $^{90}\text{Y}$ ,  $^{131}\text{I}$ , and  $^{177}\text{Lu}$  calculated by egs\_mird were in good agreement with those from other MC codes in the literature. All the DPKs have a similar profile as shown in Figure 3.3 to Figure 3.5. At the center voxel where the source was, the absorbed dose was very high compared to the surrounding voxels due to energy deposition by electrons within a few millimeters of the source. At larger distances, the beta (electron) contribution became negligible relative to the bremsstrahlung contribution.

As shown in Figure 3.3, the  $^{90}\text{Y}$  DPK calculated by EGS4 diverges from egs\_mird and other MC codes from the literature. The algorithms for electron and photon transport and multiple scattering events and cross-section libraries used in EGS4 code could be different from egs\_mird and other MC codes.<sup>236,238-241</sup> Similarly for  $^{131}\text{I}$ , in Figure 3.4, egs\_mird was in good agreement with the literature. At distances further away from the source voxel, slight differences were noticed, from poor statistics due to the high-energy spectrum of  $^{131}\text{I}$ .

Figure 3.5 shows that the  $^{177}\text{Lu}$  DPK calculated by egs\_mird agreed well with vxIPen except at the source pixel where egs\_mird was 9.96% higher than vxIPen. The source of the difference was due to the difference in the  $^{177}\text{Lu}$  emission spectrum used in the simulation. In the vxIPen simulation, only primary emissions of  $^{177}\text{Lu}$  were utilized,

while excluding electron capture and Auger electrons. The egs\_mird DPK simulation included electron capture and Auger electrons which contributed a more absorbed dose at the source voxel. Table 3.5 shows vxIPen excluded electron capture and Auger electron contributed an additional 0.033 mGy/(MBq.s) at the source voxel. This missing dose from vxIPen was close to the source voxel difference between egs\_mird and vxIPen DPK 0.031 mGy/(MBq.s) (see inset in Figure 3.5). This result shows that the decay spectrum is one of the critical factors that significantly affect the accuracy of dose calculation with MC simulation. The dose in Gy/decay is converted to mGy/(MBq.s) by scaling Gy/decay with  $10^9$ . One decay is equivalent to one becquerel second (Bq.s).

**Table 3.5:** Theoretical calculation to estimate the absorbed dose from electron capture and Auger electron not considered in vxIPen MC simulation of the decay of  $^{177}\text{Lu}$  radionuclide source.

Emission	Energy (keV)	Frequency (%)	$\approx$ Range (mm)	E. Dep (J/decay)	Dose (Gy/decay)	Dose (mGy/MBq.s)
Auger-L e-	7.720	8.750	0.011	1.08E-16	1.69E-12	1.69E-3
ce-K e-	6.291	0.123	0.011	1.24E-18	1.94E-14	1.94E-5
Auger-K e-	53.647	0.283	0.197	2.43E-17	3.80E-13	3.80E-4
ce-K e-	47.599	5.070	0.197	3.87E-16	6.04E-12	6.04E-3
ce-L e-	101.678	6.840	0.665	1.11E-15	1.74E-11	1.74E-2
ce-M e-	110.348	1.710	0.665	3.02E-16	4.72E-12	4.72E-3
ce-K e-	143.015	0.570	1.322	1.31E-16	2.04E-12	2.04E-3
ce-L e-	197.094	0.098	2.118	3.09E-17	4.84E-13	4.84E-4
					Total	3.28E-2

### 3.5 Conclusion

This work has validated egs\_mird MC code which can be used to calculate a patient-specific dose distribution from TRT. Validation was completed using internal and external consistency tests. Internal consistency tests were based on testing that energy was conserved between  $^{177}\text{Lu}$  DPK with and without transport as well as between monoenergetic photon and electron DPK and the assumed energy also with and without transport. The external consistency validation of egs\_mird compared DPK for  $^{90}\text{Y}$ ,  $^{131}\text{I}$ , and  $^{177}\text{Lu}$  calculated using egs\_mird with those using other Monte Carlo codes such as DOSXYZnrc, vxIPen, EGS4, MCNP4C, and GEANT4 cited in the literature.

## Chapter 4

### 4 Three-Dimensional Voxel-Level Dose Point Convolution Code

#### 4.1 Motivation

Targeted radionuclide therapy (TRT) requires an accurate calculation of the energy deposited by a radionuclide per unit mass (dose) in patients to achieve optimal patient outcomes.<sup>208,224</sup> Visualizing patient-specific absorbed dose distributions in three-dimensions (3D) is of high clinical value to avoid low-dose regions which might lead to potential lesion recurrence and high-dose regions which could cause necrosis in normal tissues. Moreover, normal organs might have sub-compartments that have different tolerances to radiation, thus non-uniform dose distributions could result in different levels of toxicity.<sup>208,224</sup> Due to these reasons, patient-specific targeted radionuclide therapy dosimetry is important for treatment planning to achieve an adequate dose to a tumor without serious normal tissue toxicity and for establishing radiation dose-response of biological tissues to guide clinical trials. A prerequisite to patient-specific 3D absorbed dose calculation is the time-integrated activity (TIA) distribution of the administered radionuclide over the residence time in the patient. The measurement of patient-specific TIA by quantitative SPECT (e.g.,  $^{177}\text{Lu}$ ) or PET (e.g.,  $^{18}\text{F}$ ) is discussed in §2.3.4.<sup>208</sup>

With the patient-specific TIA known, the absorbed dose distribution in TRT can be calculated using organ S-value, voxel S-value superposition (dose point kernel convolution), or the Monte Carlo method as discussed in Chapter 2. Monte Carlo simulation is the most accurate method for calculating voxel-based patient-specific absorbed dose distributions at present, but it is time-consuming, computationally expensive, and generally hard to implement. Besides overcoming the challenges of the organ S-value dose calculation method as discussed in §2.3.1, DPK convolution, like MC simulation, is a fast, voxel-based dosimetry method. This chapter introduces a 3D voxel-based DPK convolution (3DDC) code developed in my research and investigates whether it is accurate and faster in comparison to MC simulation for patient-specific dosimetry in

prostate cancer using the TIA distribution from a diagnostic dynamic PET [ $^{18}\text{F}$ ]DCFPyL study to approximate that of [ $^{177}\text{Lu}$ ]PSMA-617 used in TRT.

## 4.2 Methods

### 4.2.1 Dynamic PET and CT Study

Registered CT and PET scan from a prospective clinical trial (NCT04009174) on men with untreated biopsy-proven localized prostate cancer were used to obtain both the patient-specific anatomy and TIA distribution. The institutional Research Ethics Board approved the clinical trial protocol (NCT04009174). All participants provided written informed consent before the investigation. A CT scan of the pelvis covering the entire prostate gland was first obtained, followed by a dynamic [ $^{18}\text{F}$ ]DCFPyL PET scan where a sequence of images of the same pelvic region as the CT scan was recorded over 22 minutes starting at the same time of injection of the radiotracer in an antecubital vein with varied image durations of 10 seconds (10 image sets), 20 seconds (5 image sets), 40 second (4 image sets), 60 seconds (4 image sets), and 180 seconds (4 image sets). The patient remained stationary on the patient's couch between the two imaging sessions. In addition, to help localize the low resolution [ $^{18}\text{F}$ ]DCFPyL uptake in the patient's anatomy, the CT scans were also used for attenuation correction of PET activity, as well as to determine the density and composition of tissue for MC simulations.

The CT and PET images had a thickness of 3.75 mm and 3.27 mm, respectively. However, the CT voxel size was  $0.98 \times 0.98 \times 3.75 \text{ mm}^3$  while the PET voxel size was  $3.90 \times 3.90 \times 3.27 \text{ mm}^3$ . The MIM Maestro (MIM Software Inc., OH, 195 USA) auto-contouring software was used to contour the different organs/tissues – prostate, bladder, rectum, and femurs – from the CT scans and the contours saved in a CT structure file. The TIA distribution was derived from the dynamic PET images by integrating the time-activity curves of each voxel by trapezoidal rule over the same duration of the PET acquisition (i.e. 22 min).

#### 4.2.2 Conversion of PET and CT Data for DPK Convolution and Monte Carlo Simulation

The patient PET and CT data were converted into an EGSnrc format geometry (egsphant file) and an activity file that comprises a list of time-integrated activity for each voxel using in-house conversion tools (available at <https://github.com/Robarts-LeeLab/DICOM>). The patient geometry was determined by converting the HUs in 47 CT slices to density using a HU versus density curve appropriate for the CT scanner. After that, densities are used to assign media types (e.g., prostate, muscle, bone etc.) to various regions. Media was assigned using an assignment scheme, which had previously been employed with EGSnrc egsphant in brachytherapy<sup>242,243</sup> and used the density thresholds for all media as shown in Table 4.1. The media P50C50 was a media assigned to hybrid prostate/calcification voxels that were assumed to be approximately 50% calcification (by mass), to create a middle ground for voxels that are only partially calcified.

The voxel in each dynamic PET image was the average activity concentration over the image acquisition interval, therefore the voxel TIA in units of Bq was calculated as the sum of all dynamic images and then scaled by voxel volume which is  $3.90 \times 3.90 \times 3.27 \text{ mm}^3$  or 0.050 mL. The 3D TIA array was  $128 \times 128$  (the same size as the PET images) whereas the egsphant array from the patient CT images was  $512 \times 512$ . The TIA of each egsphant voxel was linearly interpolated from the 3D TIA array. Any egsphant voxel where the density was less than  $0.75 \text{ g/cm}^3$  was assumed to be air, and the corresponding TIA was set to zero. As calcifications were shown to significantly influence dose results in brachytherapy.<sup>242,243</sup>, two TIA arrays were generated for patients with calcifications in the prostate to investigate their potential effect on the voxel-based dose distribution. One with no further restrictions other than the air voxel TIA was set to zero and the other with the TIA in calcification set to zero which was equivalent to halving the TIA in the hybrid prostate/calcification voxels assuming their composition was 50:50.

**Table 4.1:** The media assignment scheme used to assign the media described in Table 4.2 to different structures defined for the patient CT.

Structure	Medium	Density (g/cm <sup>3</sup> )	
		Lower	Upper
Patient (everywhere)	Air	0	0.75
	Male Soft Tissue	0.75	1.14
	Cortical Bone	1.14	∞
Prostate	Prostate	0	1.14
	P50C50	1.14	1.27
	Calcification	1.27	∞
Rectum	Rectum	0	∞
Bladder	Bladder (full)	0	∞
Femur	Male Soft Tissue	0	1.14
	Cortical Bone	1.14	∞

**Table 4.2:** The density and atomic composition of all elements used in this work with their accompanying source in the literature. DPK Tissue also includes trace amounts of Mg, Si, Fe, Zn, Rb, Zr, and Pb not listed on the table.

Medium	Density (g/cm <sup>3</sup> )	Atomic Mass Fractions											Source Paper
		H	C	N	O	Na	P	S	Cl	K	Ca	Ar	
Male Soft Tissue	1.030	10.500	25.600	2.700	60.200	0.100	0.200	0.300	0.200	0.200			ICRU4611 <sup>244</sup>
Cortical Bone	1.920	3.400	15.500	4.200	43.500	0.100	0.200	0.300	0.200	0.200			ICRU46 <sup>244</sup>
Prostate	1.040	10.500	8.900	2.500	77.400	0.200	0.100	0.200	0.200	0.000	0.000		ICRU46 <sup>244</sup>
Calcification	3.060	0.300	1.600	0.500	40.700	0.000	18.700	0.000	0.000	0.000	38.200		ICRU46 (for breast) <sup>244</sup>
Prostate/Calcification	1.552	5.400	5.250	1.500	59.050	0.100	9.400	0.100	0.000	0.100	19.100		50/50 hybrid medium
Rectum	0.750	6.300	12.100	2.200	78.800	0.010	0.100	0.000	0.100	0.100	0.000		ICRU46 <sup>244</sup>
Bladder (full)	1.030	10.800	3.500	1.500	83.000	0.300	0.100	0.100	0.500	0.200	0.000		ICRU46 <sup>244</sup>
Marrow Yellow	0.980	11.800	64.600	0.700	23.200								Schneider et al <sup>245</sup>
Marrow Yellow-Red	1.000	11.000	53.100	2.100	33.600		0.100						Schneider et al <sup>245</sup>
Marrow Red	1.030	10.600	41.700	3.400	44.200		0.100						Schneider et al <sup>245</sup>
Air	0.001	0.070	0.010	75.030	23.610							1.270	Rivard et al <sup>246</sup>
Water	0.998	11.110			89.990								Rivard et al <sup>246</sup>

### 4.2.3 Absorbed Dose Calculation Comparison between Analytical Calculation, DPK Convolution and Monte Carlo Simulation

In order to validate the 3D dose convolution code, MC simulations with and without (where the absorbed dose is deposited only at the center voxel) radiation transport were used to calculate the DPK of a radionuclide source that emits a 500 keV monoenergetic electron. The choice of this particular ‘fake’ radionuclide for the validation is that the absorbed dose distribution corresponding to a uniform TIA of 1.0 Bq.s can be easily calculated analytically. The analytically calculated dose distribution was then used as the reference for comparison with those calculated by DPK convolution and MC simulation.

The 3D DPK simulation phantom  $65 \times 65 \times 64 \text{ cm}^3$  in size at a voxel resolution of  $0.0976 \text{ cm} \times 0.0976 \text{ cm} \times 0.351 \text{ cm}$  was filled with a uniform prostate media at a uniform density of  $1.03 \text{ g/cm}^3$  and a TIA of 1.0 Bq.s per voxel. The total number of voxels in the phantom was  $513 \times 513 \times 47 = 12,368,943$  and the total TIA in the phantom was numerically the same since the TIA per voxel was 1.0 Bq.s. The 3D dose convolution code was used to calculate (numerically) the absorbed dose by convolving the 3D DPK,  $DPK(\underline{\mathbf{r}})$  with the time-integrated activity,  $TIA(\underline{\mathbf{r}})$ . In principle, the absorbed dose,  $D(\underline{\mathbf{r}})$  can be calculated analytically using Equation 4.1.

$$D(\underline{\mathbf{r}}) = DPK(\underline{\mathbf{r}}) \otimes TIA(\underline{\mathbf{r}}) \quad 4.1$$

where  $\otimes$  is the convolution operator. Expanding Equation 4.1 as a 3D convolution integral yields Equation 4.2.

$$D(\underline{\mathbf{r}}) = \int_0^{\infty} DPK(\underline{\mathbf{s}}) TIA(\underline{\mathbf{r}} - \underline{\mathbf{s}}) d\underline{\mathbf{s}} \quad 4.2$$

where  $\underline{\mathbf{r}}$  and  $\underline{\mathbf{s}}$  are the target and source coordinates. Since  $TIA(\underline{\mathbf{r}}) = 1.0$  for all  $\underline{\mathbf{r}}$ , the integral simplifies to Equation 4.3.

$$D(\underline{\mathbf{r}}) = \int_0^{\infty} DPK(\underline{\mathbf{s}}) d\underline{\mathbf{s}} \quad 4.3$$

that is,  $D(\mathbf{r})$  is uniform and equal to the sum of all voxels in  $DPK(\mathbf{r})$  which by energy conservation is the energy of the emitted electron (500 keV) divided by the voxel mass ( $1.03 \text{ g/cm}^3 \times 0.0976 \text{ cm} \times 0.0976 \text{ cm} \times 0.351 \text{ cm} = 3.44 \text{ mg}$ ) to estimate the analytical dose,  $2.33 \times 10^{-8} \text{ Gy}$  ( $8.0109 \text{ Joules}/3.44 \times 10^{-6} \text{ kg}$ ) One kiloelectronvolts is equivalent to  $1.60 \times 10^{-16} \text{ Joules}$  and  $1 \text{ mg}$  equals  $10^{-6} \text{ kg}$ . As the dose distribution calculated by Monte Carlo simulation (e.g., `egs_mird` used in this work) by necessity is normalized by the total TIA in the phantom. From Equation 2.10 (discussed in §2.3.3.1), the DPK simulation with `egs_mird` is  $(DPK(x, y, z))$ , because the total TIA is 1.0 (the unit is arbitrary, it can be Bq.s) or  $\sum_{k=1}^M \sum_{i,j=1}^N TIA(x_i, y_j, z_k) = 1.0$ , then we can rewrite Equation 2.12 as:

$$MC_{norm}(x, y, z) = D(x, y, z) = DPK(x, y, z) \quad 4.4$$

From Equation 4.4, in other words, for DPK simulation, the dose is per unit of TIA (i.e., Bq.s). For a patient, `egs_mird` MC gives the dose distribution normalized by the total TIA while the DPK normalized to per unit TIA convolves with the TIA distribution gives the absolute dose distribution. Therefore, to compare the two dose distribution, we can use two alternative approaches: normalize (divide) the DPK convolution dose distribution by the total TIA so that it is the same as the normalized `egs_mird` dose distribution or multiply the normalized `egs_mird` dose distribution by the total TIA. We also have to normalize the analytical calculated normalized dose in the phantom, which is:  $2.33 \times 10^{-8} \text{ Gy}/12,368,943 \text{ Bq.s}$  or  $1.88 \mu\text{Gy}.GBq^{-1}.s^{-1}$ .

A Monte Carlo simulation was also used to calculate the dose distribution in the same phantom as the DPK simulation. All simulations, both DPK and dose distribution, were performed using  $10^9$  histories. The dose profiles for the normalized dose distribution calculated by convolution and MC simulation were compared.

#### 4.2.4 Patient-Specific 3D Dose Convolution and Monte Carlo Simulation

Figure 4.1 shows the workflow used to perform 3D dose convolution using patient-specific PET and CT data. The 3D dose convolution was performed by convolving the 3D  $^{177}\text{Lu}$  DPK from MC simulation with the 3D time-integrated activity from PET. The



MC simulation of the  $^{177}\text{Lu}$  DPK used a  $65 \times 65 \times 65 \text{ cm}^3$  uniform phantom with density and elemental composition according to the ICRU 46 shown in Table 4.2 at a voxel resolution of  $0.0976 \text{ cm} \times 0.0976 \text{ cm} \times 0.351 \text{ cm}$  to match that of the anatomical CT scan. Required simulation parameters were set similarly to §3.2.1. The DPK simulation was averaged over a total of  $3.0 \times 10^9$  particle histories to minimize uncertainties.

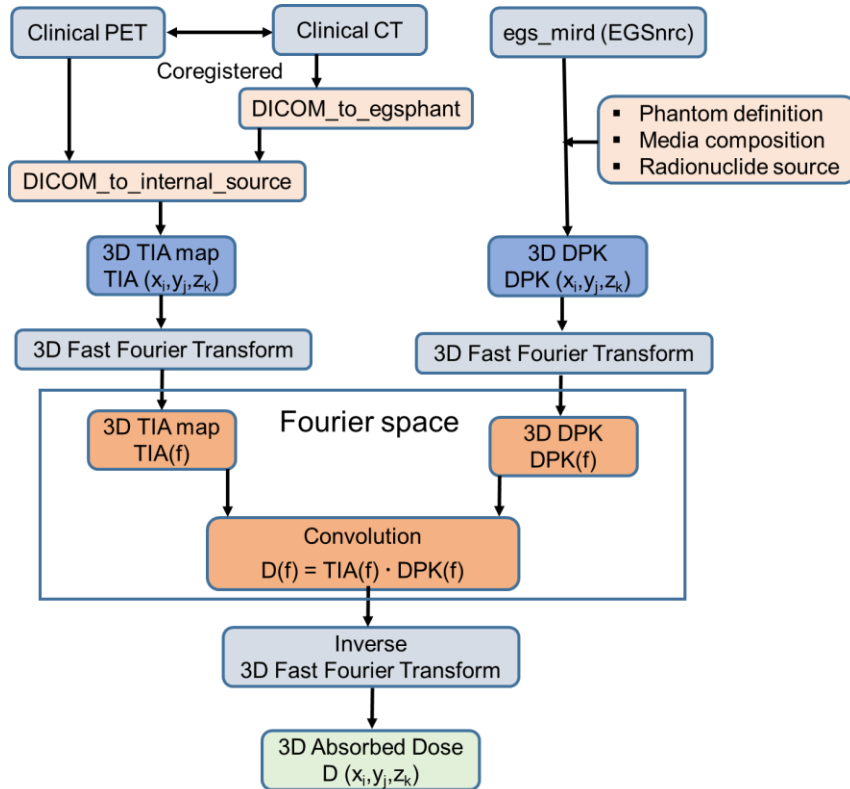


**Figure 4.1:** 3D Fast Fourier Transform dose convolution workflow

The 3D dose convolution calculation was implemented using the 3D fast Fourier transform (FFT) technique in MATLAB for six patients ( $N=6$ ). The flowchart in Figure 4.1 illustrates how the 3D FFT technique is used for 3D dose convolution. The procedure involves a 3D FFT of the TIA distribution,  $TIA(x_i, y_j, z_k)$  and of the dose point kernel,  $DPK(x_i, y_j, z_k)$ . The 3D arrays were multiplied together and inverse Fourier transformed of their product was implemented to yield the 3D absorbed dose  $D(x_i, y_j, z_k)$ .

To benchmark the 3D dose convolution algorithm, MC simulations without variance reduction (VR) and with tracklength dose scoring (as a VR technique) were performed on

the same six patients to generate the 3D dose distributions for comparison with those from the convolution algorithm. As shown in Figure 4.1, MC simulation was performed with the egsphant file and time-integrated activity file of  $^{177}\text{Lu}$  source generated from the PET/CT studies. Simulation parameters were set similar to §3.2.1 and the scheme in Table 4.1 was used to assign media to different structures outlined from the patient CT. Simulations were performed using  $10^9$  histories.

The DPK convolution absorbed dose maps were corrected for density inhomogeneity using a heuristic density correction method by scaling the DPK convolution maps voxel by voxel by  $1.04 \text{ g/cm}^3$  (the density of the DPK phantom, Table 4.2) divided by CT scan-based voxel density. Density corrected DPK convolution maps were labeled as ‘DPK’ and those without density correction as ‘DPK without Den. Corr.’ MC simulation dose maps were already density corrected in their generation. The time taken to perform DPK convolution and egs\_mird Monte Carlo simulation for patient-specific TRT dose calculation was recorded and compared. All dose calculations were implemented using AMD Ryzen 9 3900XT processor.

## 4.3 Results

### 4.3.1 Absorbed Dose Comparison between Analytical Calculation, DPK Convolution and Monte Carlo Simulation

#### 4.3.1.1 Results for No Radiation Transport

Shown in Figure 4.2 are profiles along the x-, y-, and z-axis of the DPK of a radionuclide source that emits only 500 keV monoenergetic calculated by egs\_mird when no radiation transport. The DPK profile is a delta function with an absorbed dose of  $2.3261 \times 10^{-8}$  Gy at center voxel, the same as given by analytical calculation discussed in §4.2.3.

The absorbed dose distributions from a uniformly distributed radionuclide source emitting a 500 keV monoenergetic electron at voxel TIA of 1 Bq.s were calculated using DPK convolution and egs\_mird noVR MC with no radiation transport. Figure 4.3 compares the x-dose profiles of the two dose distributions.

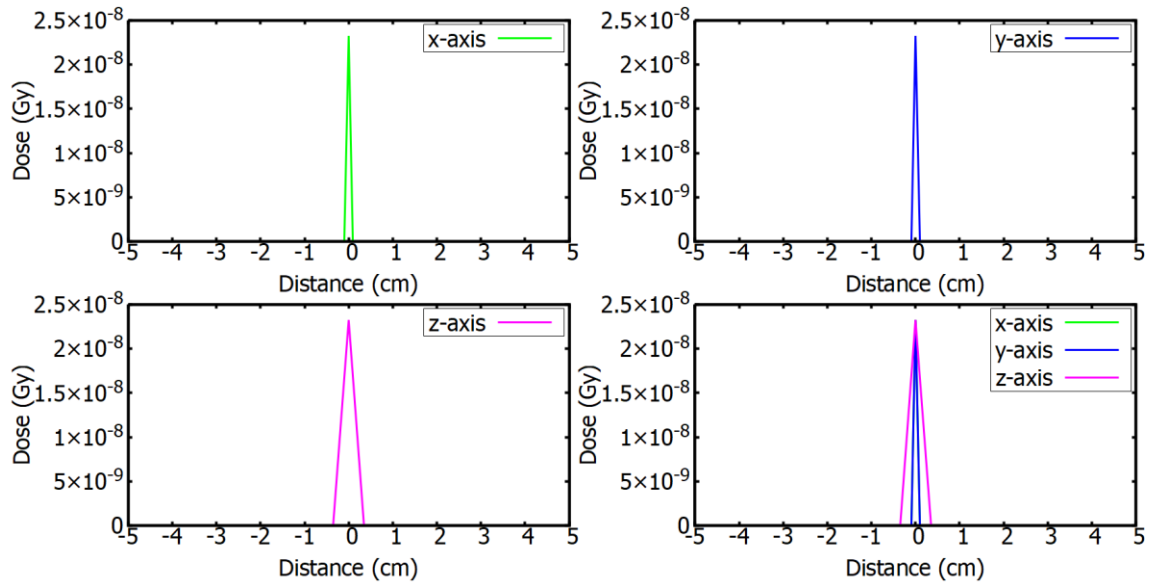


**Figure 4.2:** Dose point kernel (DK) of a radionuclide source emitting a 500 keV monoenergetic electron plotted along the x-(green), y-(blue) and z-axis (pink) for no radiation transport. The profiles along the x- and the y-axis overlap completely.

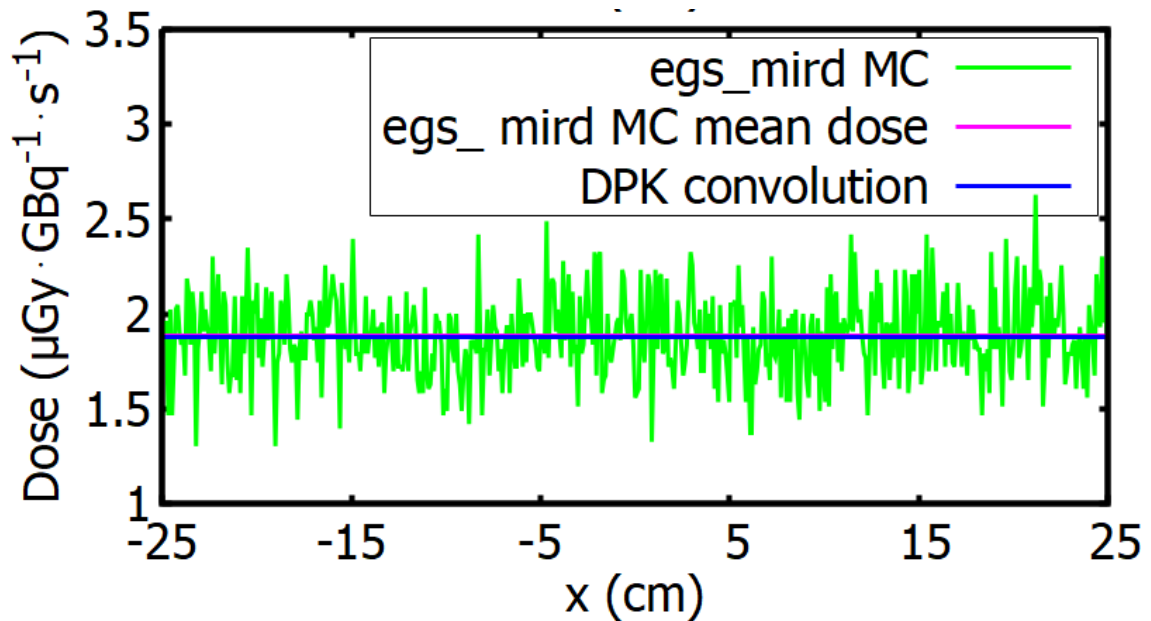


**Figure 4.3:** Dose profiles of the absorbed dose distributions in a phantom containing a 500 keV monoenergetic electron source at a uniform voxel TIA of 1 Bq.s calculated by DPK convolution and noVR MC with no radiation transport.

The x-dose profile of the DPK convolution result was a uniform horizontal line at  $1.8806 \mu\text{Gy}\cdot\text{GBq}^{-1}\cdot\text{s}^{-1}$  in good agreement with the analytical calculation of §4.2.3. While that of the noVR MC showed a mean dose that is within 0.2% of the DPK convolution profile.

#### 4.3.1.2 Results for Radiation Transport

The x-, y-, and z-axis profiles of the DPK of a radionuclide source emitting 500 keV monoenergetic electrons with radiation transport are shown in Figure 4.4. The x- and y-profiles completely overlap each other. Figure 4.5 shows the absorbed dose comparison between DPK convolution and egs\_mird noVR MC with radiation transport for a 500 keV monoenergetic electron source distributed uniformly at a voxel TIA of 1 Bq.s in a

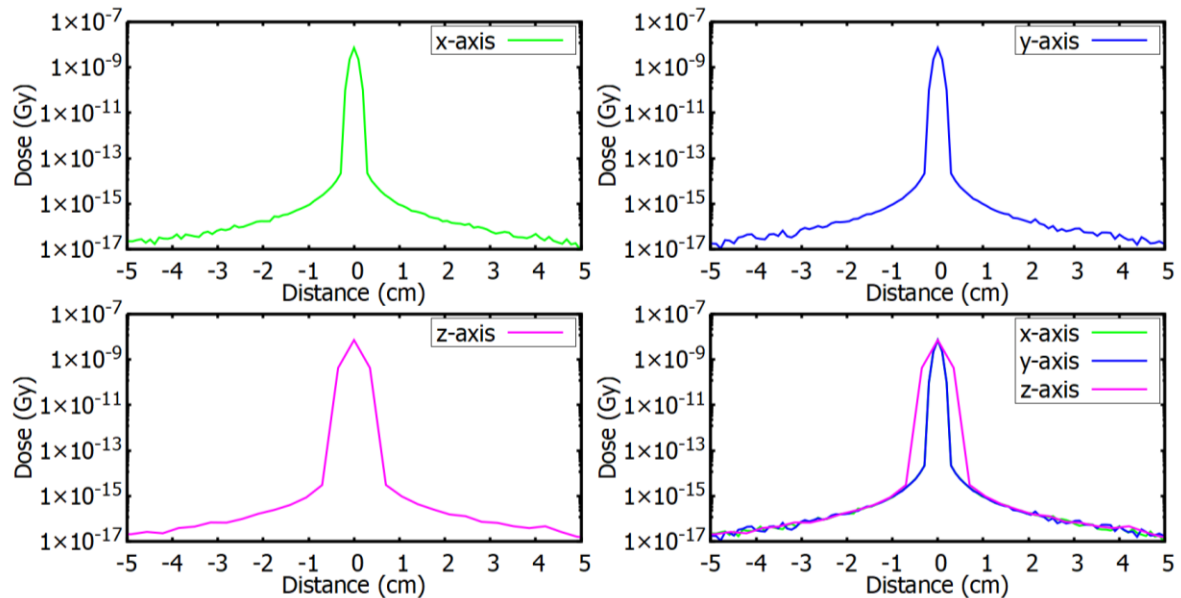


**Figure 4.4:** DPK with radiation transport of a 500 keV monoenergetic electron source plotted along the x-(green), y-(blue) and z-axis (pink).

phantom. DPK convolution dose was uniform at  $1.8797 \mu\text{Gy}\cdot\text{GBq}^{-1}\cdot\text{s}^{-1}$  in agreement with analytical calculation (§4.2.3) throughout the phantom. The dose difference between DPK convolution and egs\_mird noVR MC was about 0.4 %.

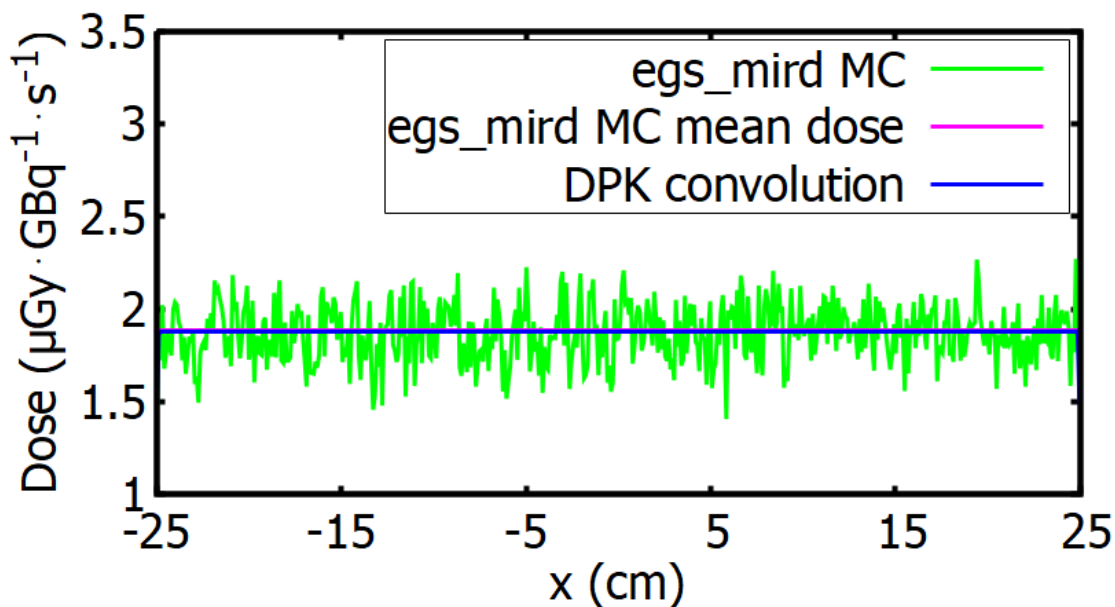


**Figure 4.5:** Dose profiles of the absorbed dose distributions in a phantom containing a 500 keV monoenergetic electron source at a uniform voxel TIA of 1 Bq.s calculated by DPK convolution and noVR MC with radiation transport.

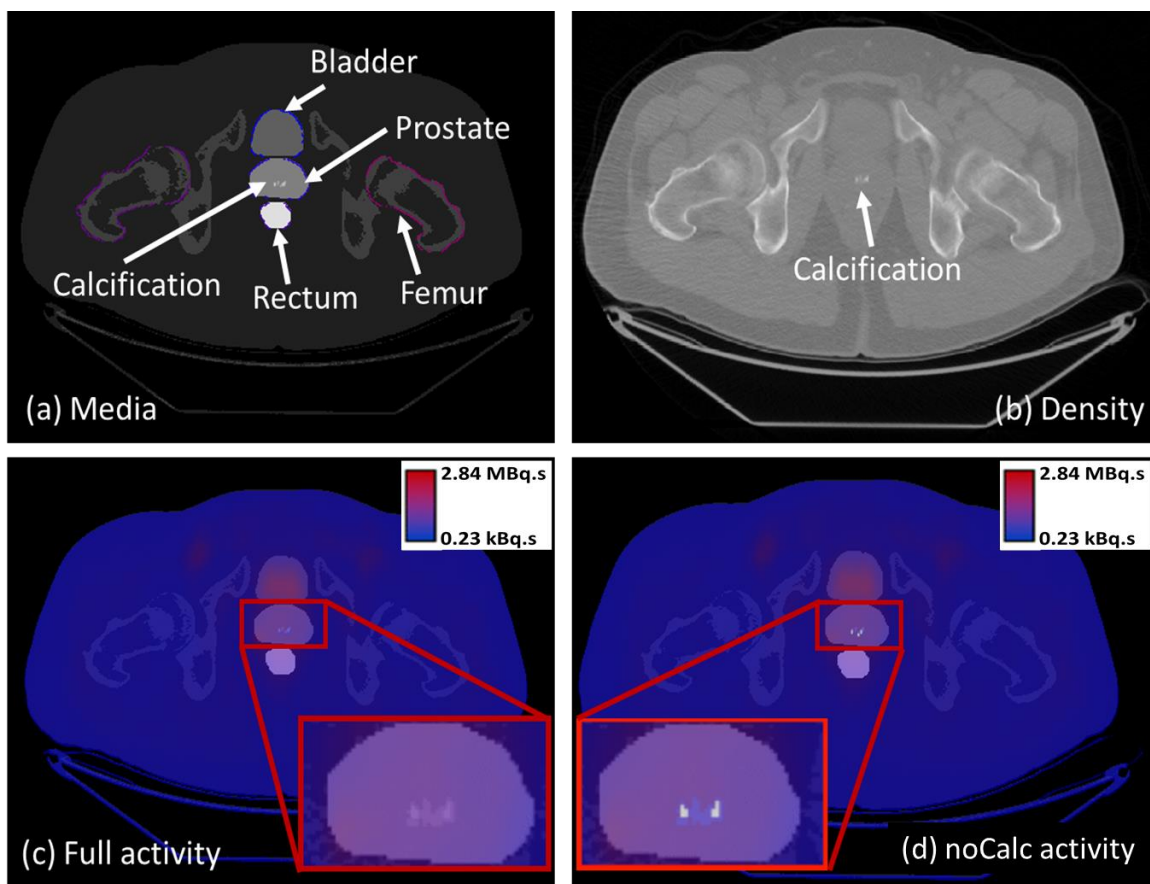
#### 4.3.2 Patient-Specific 3D Dose Convolution and Monte Carlo Simulation

Dose calculations were performed on six patients. Five patients received the  $^{18}\text{F}$ DCFPyL radiotracer; three have calcification in their prostate, while the other two are free of calcification. In the remaining patient (N=1), there is calcification in the prostate and the patient received  $^{18}\text{F}$ FCH radiotracer. The absorbed dose percentage difference between DPK convolution and full Monte Carlo simulation for all groups of patients was consistent.

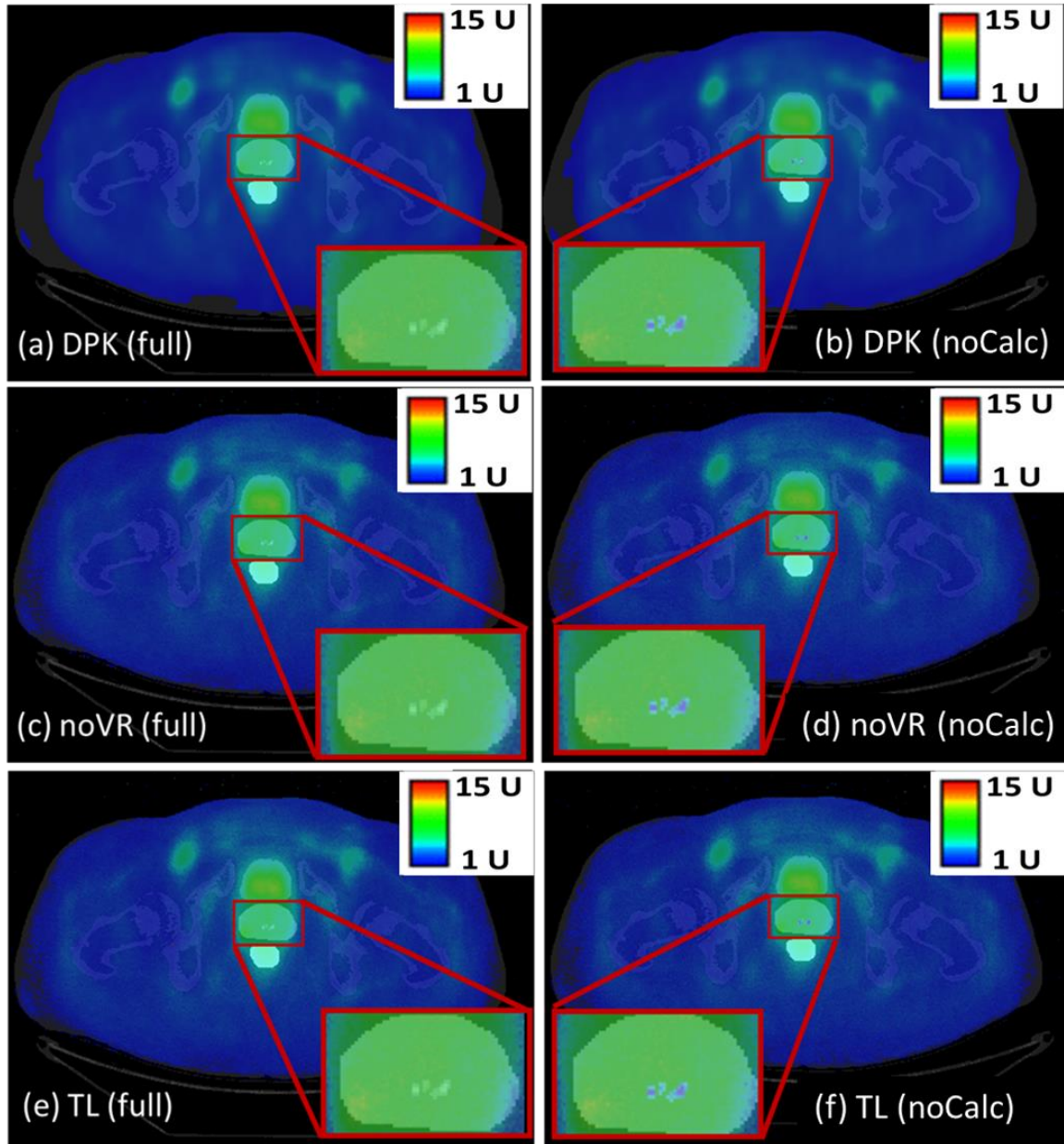
Based on time comparisons, TRT dose calculation in AMD Ryzen 9 3900XT processor took 16.23 minutes with a single core for DPK convolution and 28.47 minutes for egs\_mird noVR Monte Carlo simulation on 22 cores.

#### 4.3.2.1 Voxelwise Dose Maps and Dose Profiles for a Patient with Calcification in the Prostate that Received [18F]DCFPyL

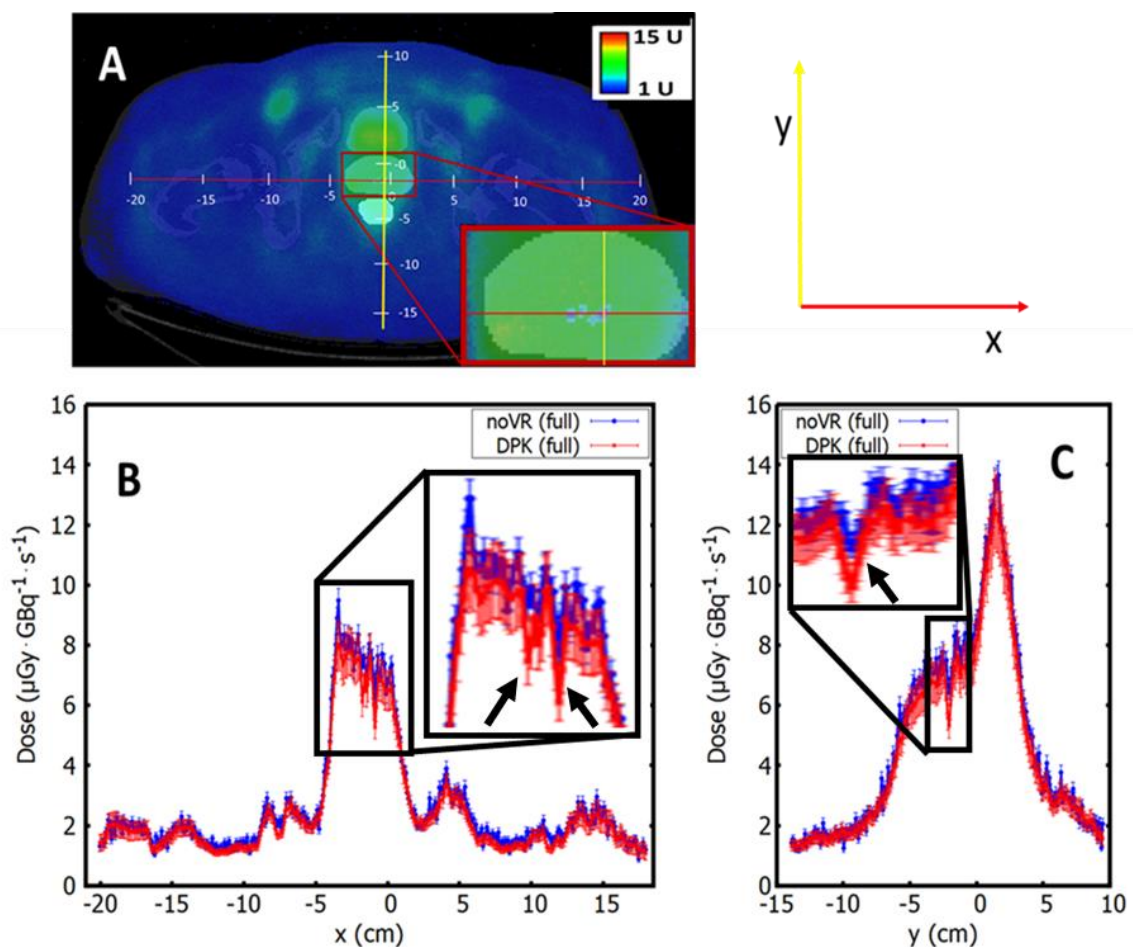
Figure 4.6 illustrates a cross-section slice from the [18F]DCFPyL PET and CT study of a patient with calcifications in the prostate showing various media assignments, density distribution (map), and TIA maps for full and no activity in the calcifications of a patient (IGPC-02-036). Magnified images of the prostate region are displayed for each TIA map. Figure 4.7 are the density corrected radiation dose maps from simulated  $^{177}\text{Lu}$  TRT corresponding to the cross-sectional slice shown in Figure 4.6.



**Figure 4.6:** A cross-sectional slice from the [18F]DCFPyL PET/CT study of a patient (IGPC-02-036) showing (a) media assignment, (b) density map, and TIA map for (c) full activity and (d) noCalc denoting no activity in calcifications.



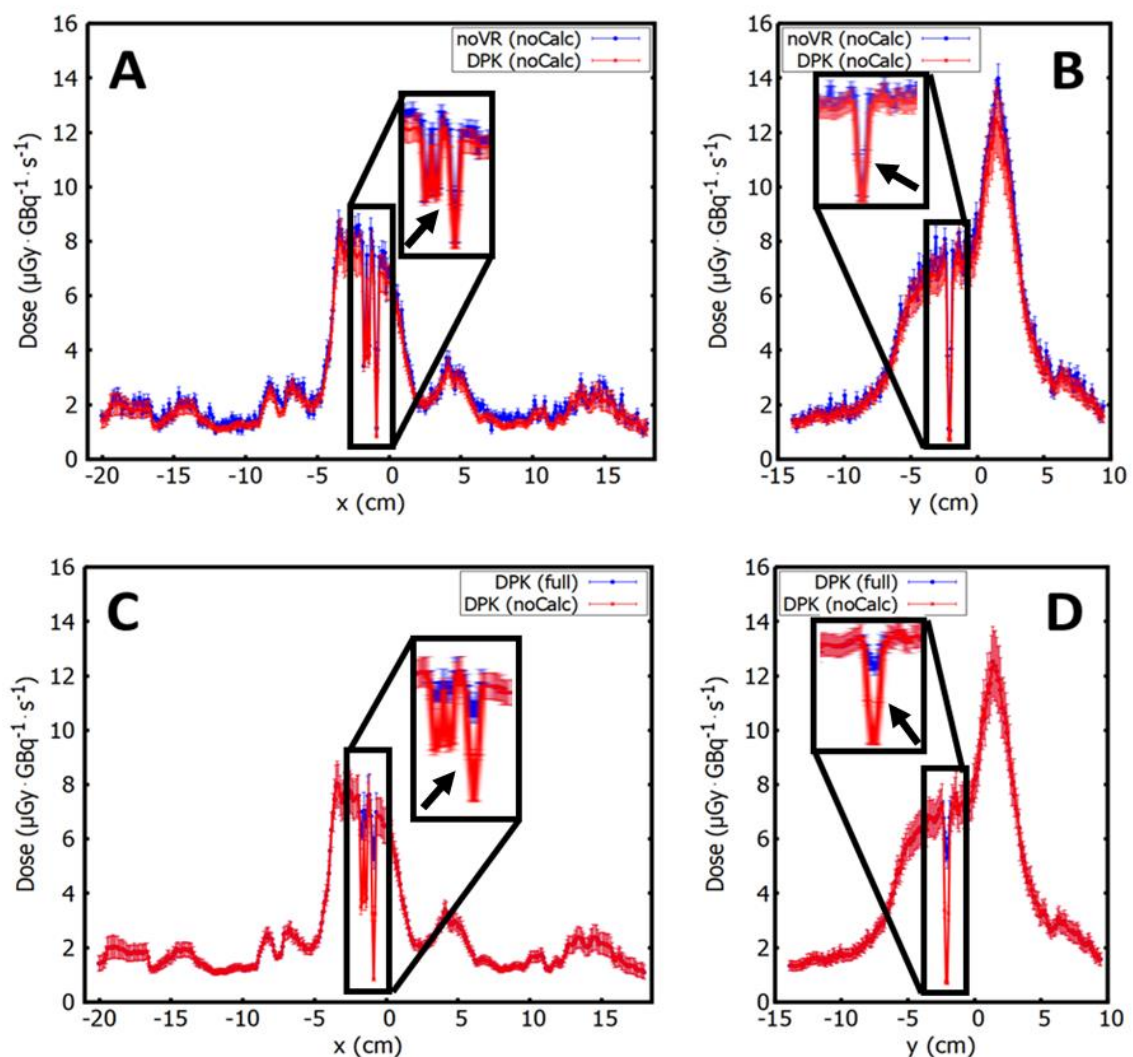
**Figure 4.7:** Dose map from simulated  $^{177}\text{Lu}$  TRT of the same cross-sectional slice as Figure 4.7. in  $\text{U} = \mu\text{Gy}\cdot\text{GBq}^{-1}\cdot\text{s}^{-1}$  units. The dose maps were computed using DPK convolution (top) and noVR `egs_mird` simulation (middle), an `egs_mird` simulation with tracklength scoring (bottom). The left and right images show dose maps with (full) and without (noCalc) activity in the calcifications, respectively. A magnified image of the prostate is shown for each dose map.



**Figure 4.8:** X- and Y-dose profile of the density corrected DPK convolution (red) and noVR MC (blue) dose maps calculated using full activity TIA in calcifications of Figure 4.8 are shown here. The DPK simulation-derived uncertainties were convolved with the time-integrated activity to generate error bars on the DPK plot while noVR uncertainties were derived from MC simulation. The black arrows point to calcified regions.

The representative X- and Y-dose profiles of the density corrected DPK convolution against noVR MC simulation maps with full activity in calcifications are shown in Figure 4.8. Both profiles cut across calcified voxels/regions in the prostate. The density corrected DPK convolution dose profiles followed the same trend as those from the noVR MC simulation. The density corrected DPK convolution dose uncertainties were derived from convolving kernel uncertainties generated using `egs_mird` with the time-integrated activity. The noVR MC dose uncertainties were generated by `egs_mird`.





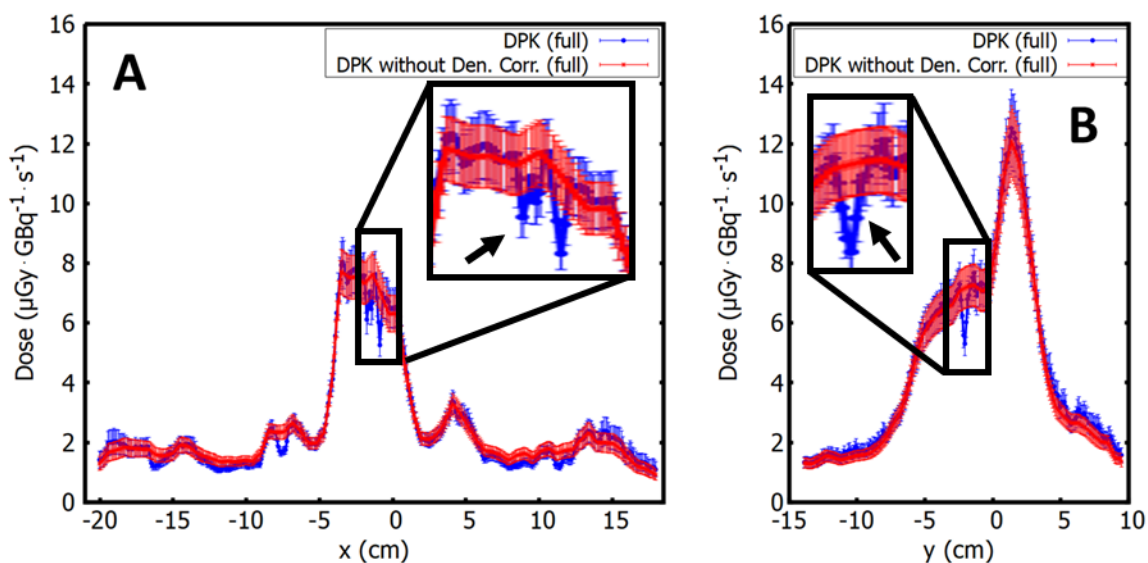
**Figure 4.9:** (A) X-dose profile of the density corrected DPK convolution (red) and noVR MC (blue) dose maps with no activity in calcifications. (B) Y-dose profile of the same dose maps as (A). (C) X-dose profiles of density corrected DPK convolution maps with full (blue) and no (red) activity in the calcifications. (D) Y-dose profiles of the same dose maps as in (C). The black arrows point to calcifications with no assumed activity in them.

Figure 4.9 shows the X- and Y-dose profiles of the density corrected DPK convolution map against the noVR MC simulation map with no activity in the calcifications as well as the dose profile comparison between density corrected DPK convolution maps with full and no activity in calcifications. As expected, the density corrected DPK convolution map showed the same trend as the noVR MC map with a dip in calcifications for no

activity. The size of the calcifications was within the  $0.0976 \times 0.0976$  pixels defined by the CT, thus density corrected DPK convolution and noVR MC simulation dose maps showed good spatial dose resolution by detecting the calcifications with either full or no activity.

#### 4.3.2.1.1 Analysis of Density Impact on DPK Convolution

To assess the impact of density heterogeneity on absorbed dose results, the DPK convolution dose maps were also generated without density correction and the X- and Y-dose profiles for maps with and without density correction are compared in Figure 4.10.



**Figure 4.10:** Comparison of (A) X- and (B) Y-dose profiles in DPK convolution dose maps with (blue) and without (red) density correction. The maps were generated with full activity in the calcifications. The black arrows point to the calcified region.

As the DPK was simulated in a phantom of the prostate density of  $1.04 \text{ g/cm}^3$  (see §4.2.3), it is expected that for density higher than prostate, DPK convolution without density correction overestimates the deposited dose while for lower density, the dose is underestimated. As shown in Figure 4.10, the deposited dose obtained with density corrected DPK showed dips in high-density regions like the calcification in the prostate and bone regions while DPK without density correction smoothed out the dose profile.

Thus, heterogeneity in density has an impact on dose results and care should be taken to account for variations in media density in targeted radionuclide therapy.

#### 4.3.2.1.2 Dose Volume Histogram for Patient with Calcifications in the Prostate

Figure 4.11 shows DVHs for all calculation methods in prostate, rectum, bladder, and bone marrow for the same patient as Figure 4.6 to Figure 4.10. In all tissue types, DPK (full) and DPK (noCalc) convolution DVH results superimposed on each other ‘completely’ and the same is true for all DVHs from the `egs_mird` MC simulation with either noVR or TL method.

To quantify the agreement between the dose distribution calculated by the density corrected DPK convolution method and the standard of reference `egs_mird` MC simulation method, the areas of the dose-volume histograms for the four regions: the prostate, rectum, bladder, and bone marrow were compared.

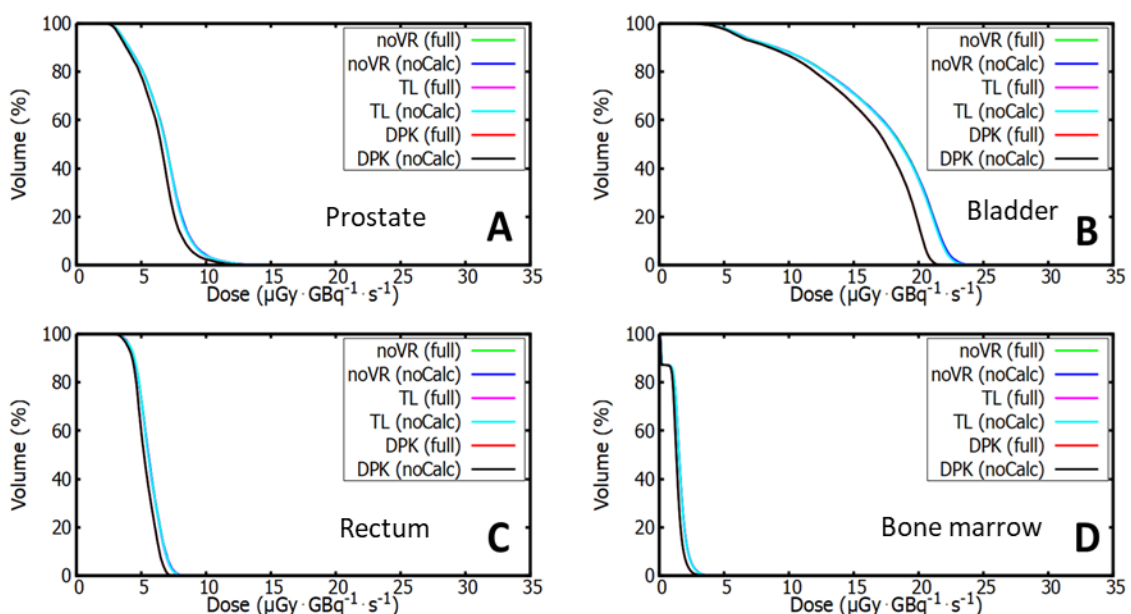


**Figure 4.11:** Dose-volume histograms derived from dose distribution calculated with density corrected DPK convolution calculations, noVR MC and TL MC using TIA

matrices with full and no activity in calcifications for (A) prostate, (B) bladder, (C) rectum, and (D) bone marrow.

The mean relative errors of DVHs for prostate, rectum, bladder, and bone marrow were  $-5.28 \pm 0.82\%$ ,  $-5.21 \pm 1.13\%$ ,  $-5.73 \pm 0.73\%$  and  $-15.60 \pm 7.19\%$ , respectively.

While for DPK without Den. Corr. the difference in DVH area against noVR MC is  $-6.44 \pm 1.23\%$ ,  $-6.1 \pm 1.39\%$ ,  $-8.69 \pm 1.12\%$ , and  $6.10 \pm 10.22\%$  for prostate, rectum, bladder, and bone marrow respectively.

**Table 4.3:** Average area under the DVH curve for the prostate and other organs at risk like the rectum, and bone marrow for the different dose calculation methods.

Organ	DPK without Den. Corr. ( $\mu\text{Gy}\cdot\text{GBq}^{-1}\cdot\text{s}^{-1}$ )	DPK ( $\mu\text{Gy}\cdot\text{GBq}^{-1}\cdot\text{s}^{-1}$ )	noVR ( $\mu\text{Gy}\cdot\text{GBq}^{-1}\cdot\text{s}^{-1}$ )
Prostate	3.92	4.02	4.53
Rectum	2.32	2.44	2.75
Bone marrow	1.56	1.24	1.46

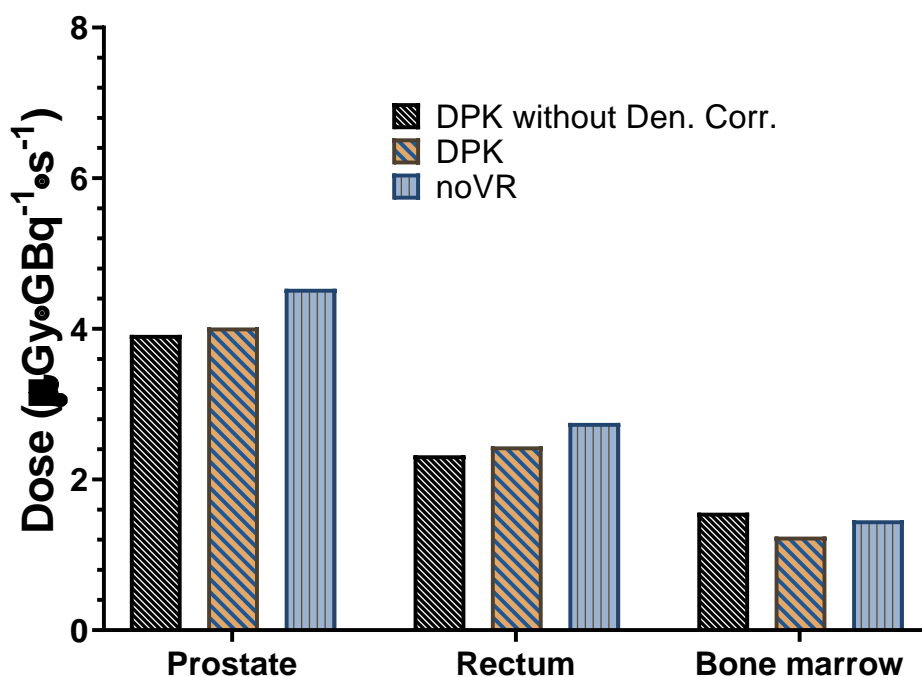


**Figure 4.12:** Organ-level absorbed doses estimated using DPK convolution with and without density correction compared to noVR MC.

The total TIA over the patient body was 979.492 GBq·s. Table 4.3 is the mean absorbed dose under the DVH curve for the prostate, rectum, and bone marrow also plotted in Figure 4.12.

#### 4.3.2.2 Voxelwise Dose Maps and Dose Profiles for a Patient without Calcification in the Prostate that Received [<sup>18</sup>F]DCFPyL

A cross-sectional slice from the [<sup>18</sup>F]DCFPyL PET/CT scan study showing various media assignments, density map, and TIA maps are depicted in Figure 4.13.



**Figure 4.13:** A cross-sectional slice from the [<sup>18</sup>F]-DCFPyL PET/CT study of a patient without calcifications in the prostate showing (a) media assignment, (b) density map, and (c) TIA map.

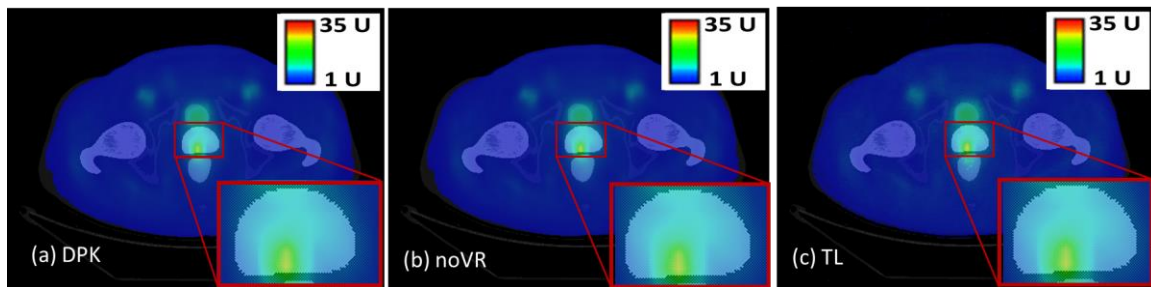


**Figure 4.14:** Dose maps of a patient without calcification in the prostate from simulated <sup>177</sup>Lu TRT. The maps were computed using DPK convolution (left) and noVR eggs\_mird simulation (middle), an eggs\_mird simulation with tracklength scoring (right). A magnified image of the prostate is shown for each dose map. Dose values are expressed in units of  $U = \mu\text{Gy} \cdot \text{GBq}^{-1} \cdot \text{s}^{-1}$ .

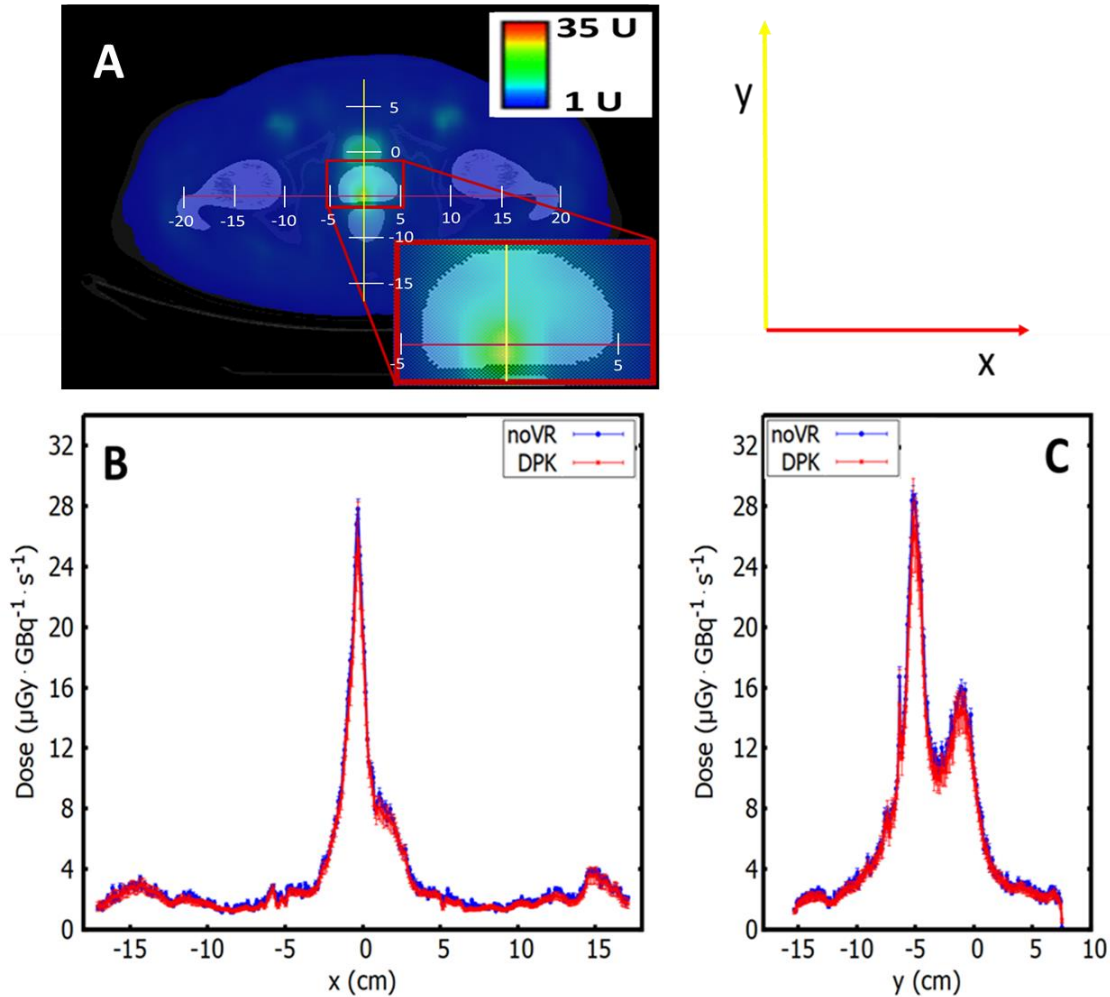


**Figure 4.15:** (A) The dose map of a cross-sectional slice superimposed on its corresponding CT image with distance scales shown for the x- and y-axis. The x-dose profiles of the  $^{177}\text{Lu}$  DPK convolution (red) and noVR MC (blue) are shown in (B) and the y-dose profiles in (C). The error bars on the dose profiles were obtained with the uncertainties in the dose maps. These uncertainties were calculated as described in the text.

This patient (IGPC-02-026) does not have calcified regions in the prostate. Figure 4.14 are the dose maps of a cross-sectional slice of the patient from the simulated  $^{177}\text{Lu}$  TRT. Each dose map was normalized by the total TIA in the patient and is displayed in units of  $\mu\text{Gy} \cdot \text{GBq}^{-1} \cdot \text{s}^{-1}$ . The dose maps were calculated by DPK convolution and egs\_mird (MC) simulation with noVR and with tracklength scoring, TL. The representative dose profiles

of the DPK convolution against noVR MC simulations are shown in Figure 4.15. The dose profiles are plotted along the x-axis and the y-axis cutting across the hot nodule in the prostate. The DPK convolution dose profile follows the same trend as the noVR MC simulation. The DPK convolution absorbed dose uncertainties are derived from convolving DPK kernel uncertainties generated using `egs_mird` with the time-integrated activity. The noVR MC absorbed dose uncertainties are derived from MC dose scoring uncertainties.

#### 4.3.2.2.1 Analysis of Density Impact on DPK Convolution

The tissue density within the prostate and other regions was not uniform. Thus, to assess the impact of density heterogeneity on dose results, dose profiles of DPK convolution maps with and without density correction are compared in Figure 4.16.

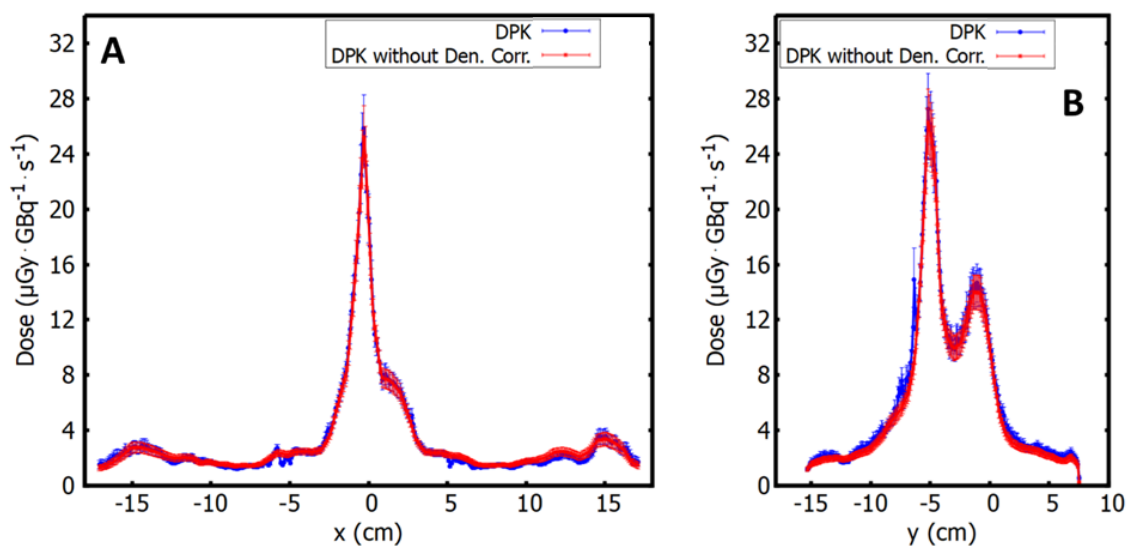


**Figure 4.16:** The difference in dose profiles between DPK convolution maps calculated using density correction (blue) and without density correction (red) using the activity TIA map from [ $^{18}\text{F}$ ]DCFPyL. The dose is in units of  $\mu\text{Gy} \cdot \text{GBq}^{-1} \cdot \text{s}^{-1}$ .

When the density of the medium is lower than that of the prostate used in the generation of the DPK, the deposited dose is underestimated, while for media with a higher density, the deposited dose is overestimated. Density corrected DPK convolution dose profile

showed dips in high-density regions, while that without density correction smoothed over density changes.

#### 4.3.2.2.2 Dose Volume Histogram for Patient without Calcifications in the Prostate

The DVHs from dose distributions of all calculation methods in prostate, rectum, bladder, and bone marrow tissue are shown in Figure 4.17 shows. The mean absolute relative errors of estimated absorbed doses between DPK convolution against MC simulations for prostate, rectum, bladder, and bone marrow were  $-5.23 \pm 0.81\%$ ,  $-5.12 \pm 1.12\%$ ,  $-5.62 \pm 0.49\%$  and  $-17.12 \pm 8.71\%$ , respectively.

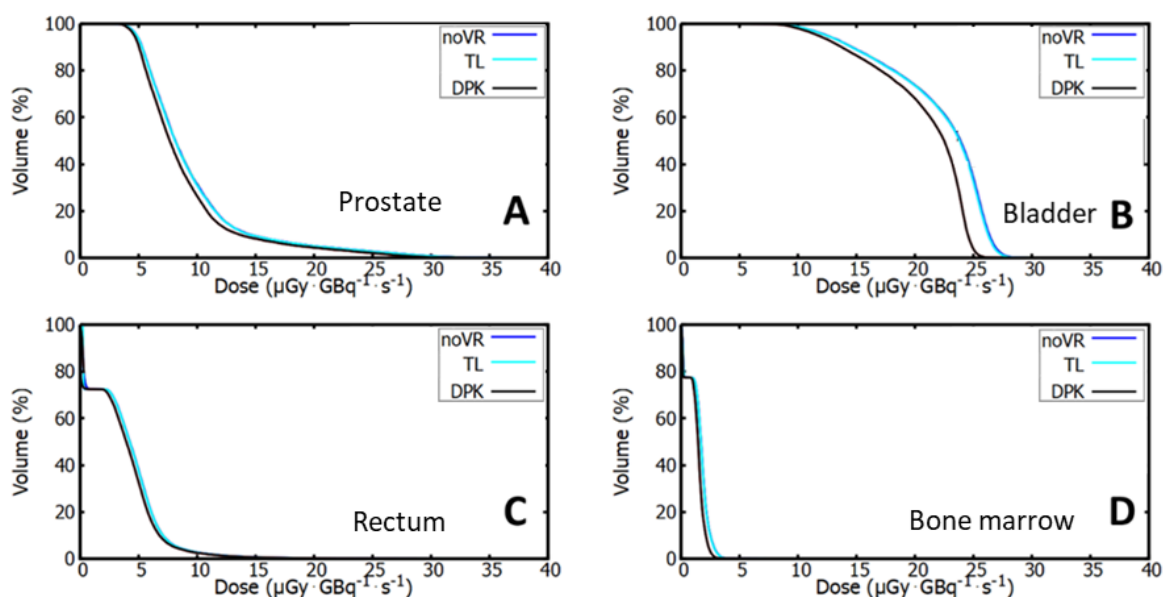


**Figure 4.17:** Dose volume histograms from dose distributions calculated by DPK convolution and MC with noVR and with TL dose scoring. There were differences between the DPK convolution and MC DVHs but the MC DVHs were the same.

For DPK convolution without density correction, the mean dose (or area of the DVH) was consistently underestimated relative to noVR MC by  $-6.59 \pm 1.01\%$ ,  $-6.13 \pm 1.39\%$ ,  $-9.2 \pm 0.78\%$ , and  $-6.42 \pm 2.90\%$  for prostate, rectum, bladder, and bone marrow respectively.



**Table 4.4:** Total dose under the DVH curve for the prostate and other organs at risk like the rectum, and bone marrow.

Organ	DPK without Den. Corr. ( $\mu\text{Gy}\cdot\text{GBq}^{-1}\cdot\text{s}^{-1}$ )	DPK ( $\mu\text{Gy}\cdot\text{GBq}^{-1}\cdot\text{s}^{-1}$ )	noVR ( $\mu\text{Gy}\cdot\text{GBq}^{-1}\cdot\text{s}^{-1}$ )
Prostate	5.68	5.71	6.50
Rectum	3.37	3.79	4.01
Bone marrow	1.58	1.27	1.51

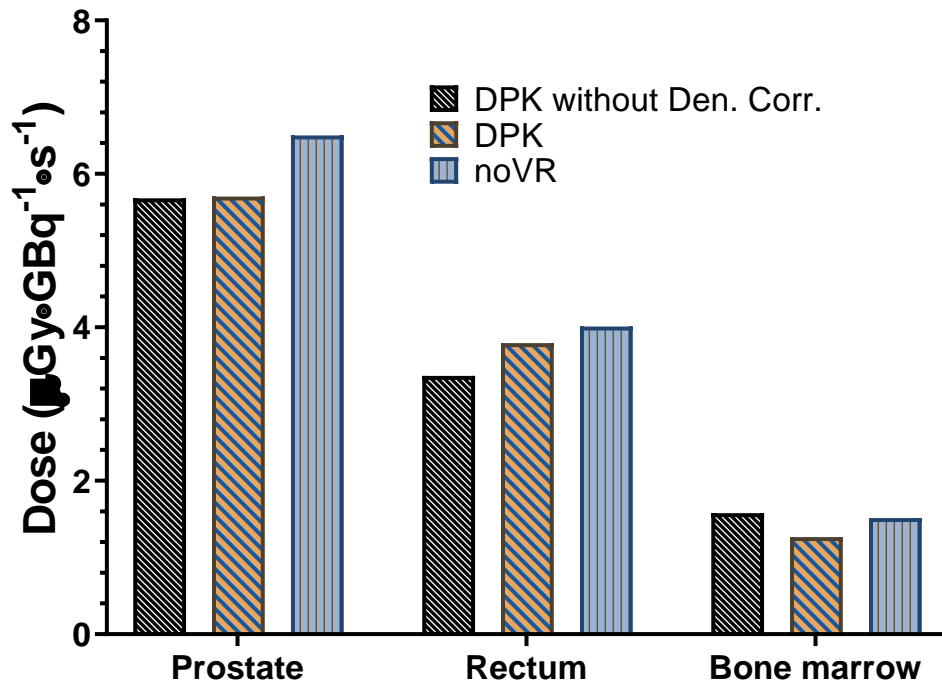


**Figure 4.18:** Organ-level absorbed doses estimated using DPK convolution with and without density correction compared to noVR MC.

The total TIA over the patient body was 1215.797 GBq·s. The area average underneath the DVH curves is the mean absorbed doses to prostate, rectum, and bone marrow respectively shown in Table 4.4 and Figure 4.18.

#### 4.3.2.3 Voxelwise Dose Maps and Dose Profiles for a Patient with Calcification in the Prostate that Received $[^{18}\text{F}]\text{FCH}$

A cross-section slice from the  $[^{18}\text{F}]\text{FCH}$  PET and CT study of a patient with calcifications in the prostate showing various media assignments, density distribution (map), and TIA maps for full and no activity in the calcifications of a patient (IGPC-02-028) is shown in Figure 4.19. Magnified images of the prostate region are depicted for each TIA map. Figure 4.20 are the density corrected radiation dose maps from simulated  $^{177}\text{Lu}$  TRT corresponding to the cross-sectional slice shown in Figure 4.19. Each dose map was normalized by the total TIA in the patient and is displayed in units of  $\mu\text{Gy}\cdot\text{GBq}^{-1}\cdot\text{s}^{-1}$ . The dose maps were calculated by DPK convolution and `egs_mird` (MC) simulation with noVR and with tracklength scoring, TL.

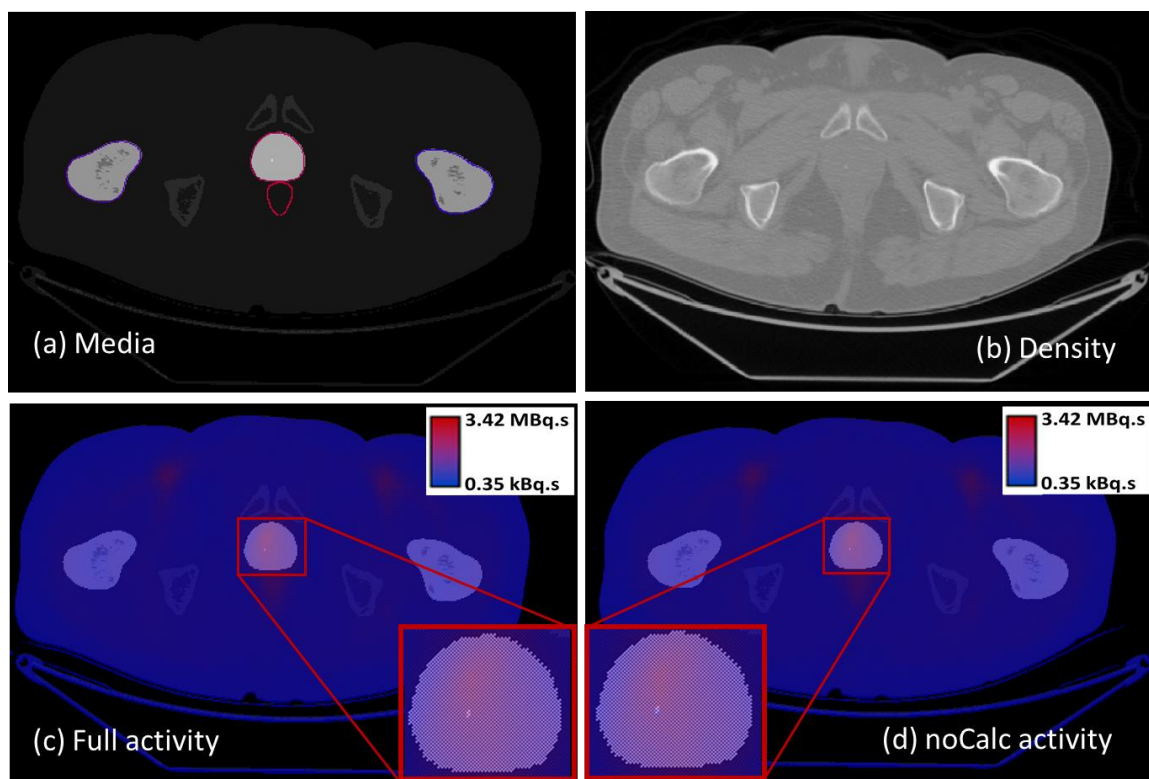


**Figure 4.19:** A cross-sectional slice from the  $[^{18}\text{F}]\text{FCH}$  PET and CT study of a patient (IGPC-02-028) showing (a) media assignment, (b) density map, and TIA map for (c) full activity and (d) noCalc denoting no activity in calcifications.

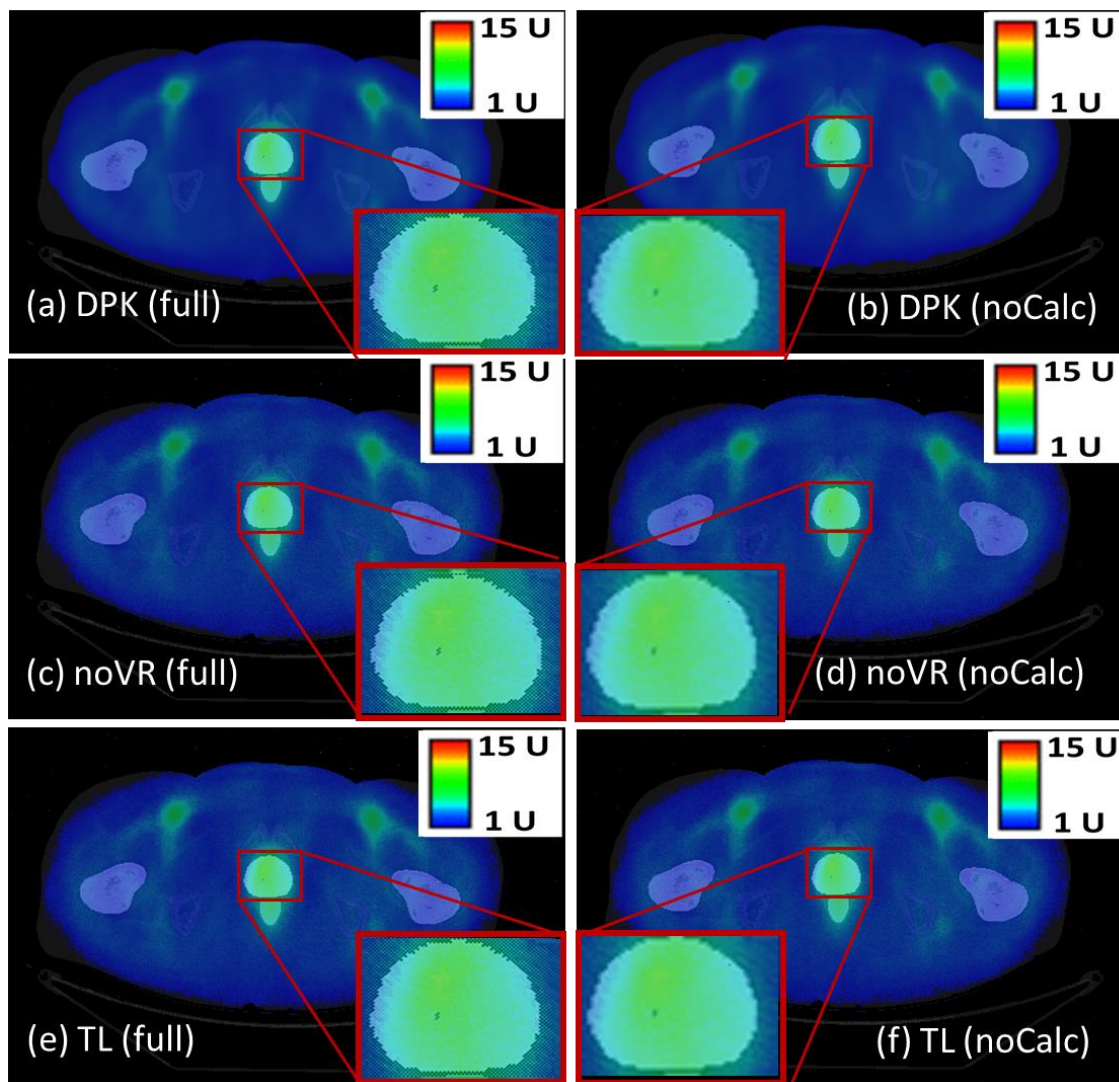


**Figure 4.20:** Dose map from simulated  $^{177}\text{Lu}$  TRT of the same cross-sectional slice as Figure 4.19 in  $\text{U} = \mu\text{Gy}\cdot\text{GBq}^{-1}\cdot\text{s}^{-1}$  units. The dose maps were computed using DPK convolution (top) and noVR `egs_mird` simulation (middle), an `egs_mird` simulation with tracklength scoring (bottom). The left and right images show dose maps with (full) and without (noCalc) activity in the calcifications, respectively. A magnified image of the prostate is shown for each dose map.

The representative X- and Y-dose profiles of the density corrected DPK convolution against noVR MC simulation maps with full activity in calcifications are shown in Figure 4.21. Both profiles cut across calcified voxels/regions in the prostate. The density corrected DPK convolution dose profiles followed the same trend as those from the

noVR MC simulation. The density corrected DPK convolution dose uncertainties were derived from convolving kernel uncertainties generated using `egs_mird` with the time-integrated activity. The noVR MC dose uncertainties were generated by `egs_mird`.

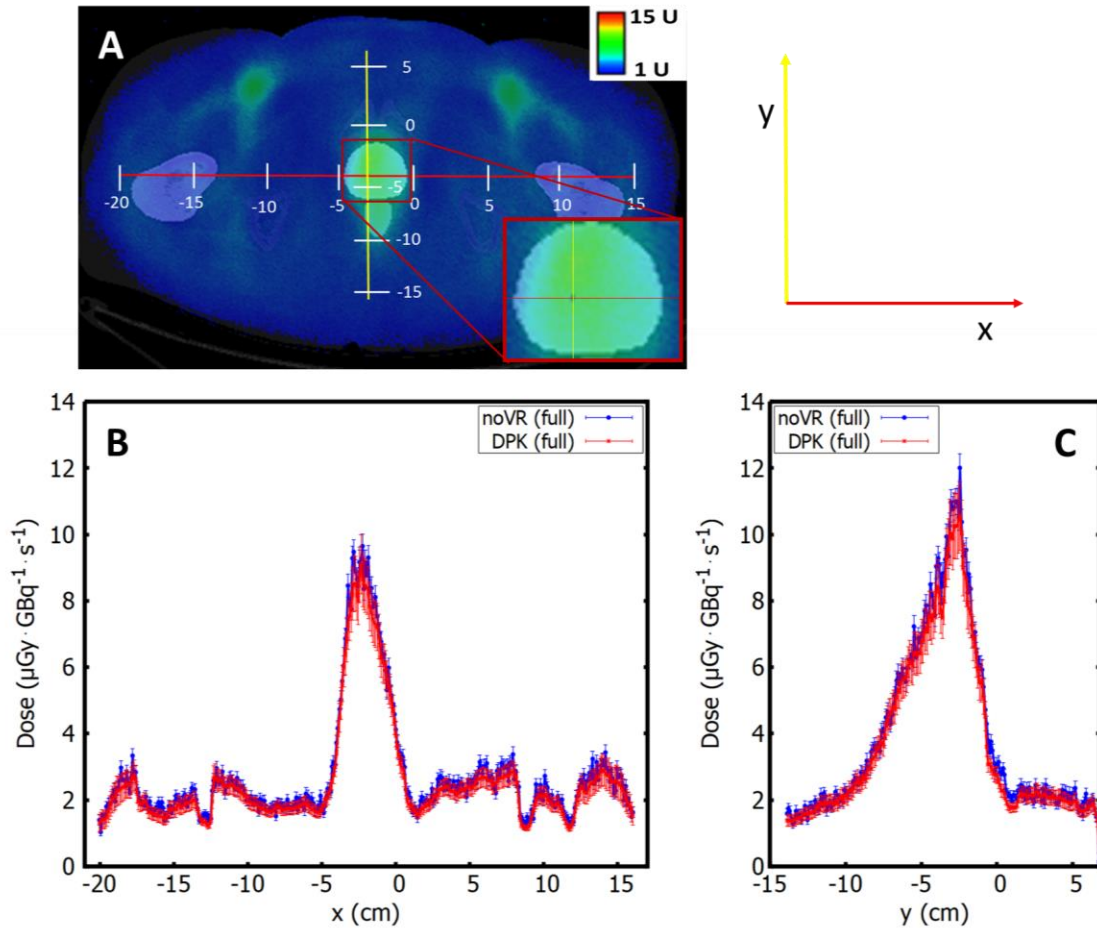


**Figure 4.21:** X- and Y-dose profile of the density corrected DPK convolution (red) and noVR MC (blue) dose maps with full activity in calcifications of Figure 4.19 are shown here. The DPK simulation-derived uncertainties were convolved with the time-integrated activity to generate error bars on the DPK plot while noVR uncertainties were derived from MC simulation.

Figure 4.22 shows the X- and Y-dose profiles of the density corrected DPK convolution map against the noVR MC simulation map with no activity in the calcifications as well as the dose profile comparison between density corrected DPK convolution maps with full and no activity in calcifications. As expected, the density corrected DPK convolution

map showed the same trend as the noVR MC map with a dip in calcifications with no activity.

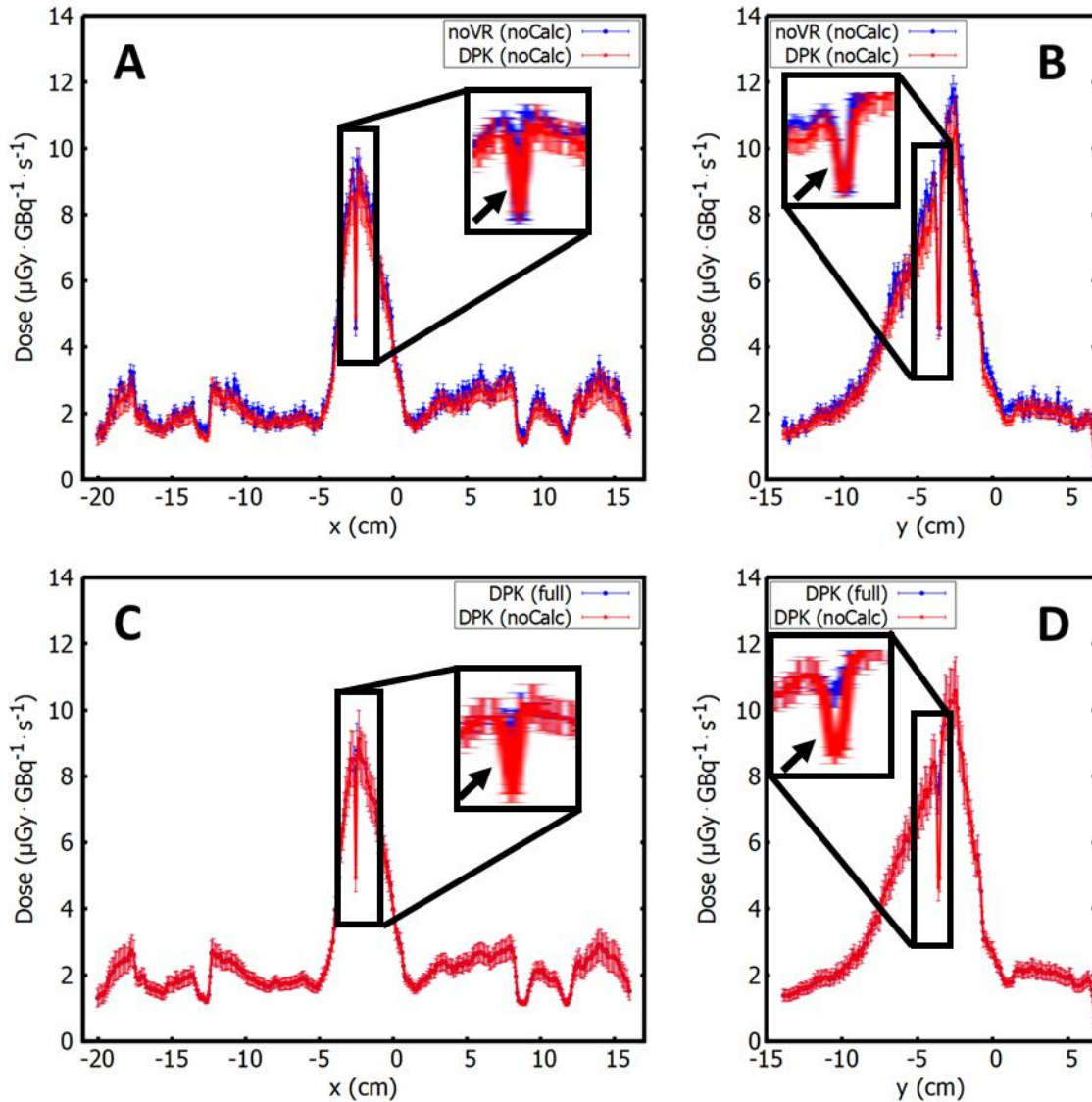


**Figure 4.22:** (A) X-dose profile of the density corrected DPK convolution (red) and noVR MC (blue) dose maps with no activity in calcifications. (B) Y-dose profile of the same dose maps as (A). (C) X-dose profiles of density corrected DPK convolution maps with full (blue) and no (red) activity in the calcifications. (D) Y-dose profiles of the same dose maps as in (C). The black arrows point to calcifications with no assumed activity in them.

#### 4.3.2.3.1 Analysis of density impact on DPK convolution

To assess the impact of density heterogeneity on absorbed dose results, the DPK convolution dose maps were also generated without density correction and the X- and Y-dose profiles for maps with and without density correction are compared in Figure 4.23.

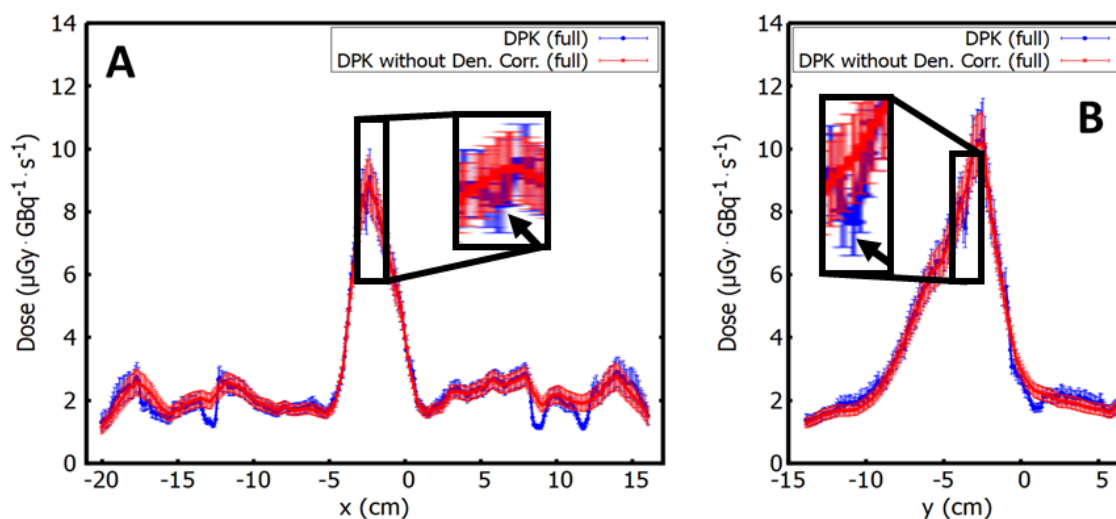


**Figure 4.23:** Comparison of (A) X- and (B) Y-dose profiles in DPK convolution dose maps with (blue) and without (red) density correction. The maps were generated with full activity in the calcifications. The black arrows point to calcification.

As the DPK was simulated in a phantom of the prostate density of  $1.04 \text{ g/cm}^3$  (see §4.2.3), it is expected that for density higher than prostate, DPK convolution without density correction overestimates the deposited dose while for lower density, the dose is underestimated. As shown in Figure 4.23, the deposited dose obtained with density corrected DPK showed dips in high-density regions like the calcification in the prostate and bone regions while DPK without density correction smoothed out the dose profile.

#### 4.3.2.3.2 Dose Volume Histogram

Figure 4.24 shows DVHs for all calculation methods in prostate, rectum, bladder, and bone marrow for the same patient as Figure 4.19 to Figure 4.23. In all tissue types, DPK (full) and DPK (noCalc) convolution DVH results superimposed on each other

‘completely’ and the same is true for all DVHs from the `egs_mird` MC simulation with either noVR or TL method.

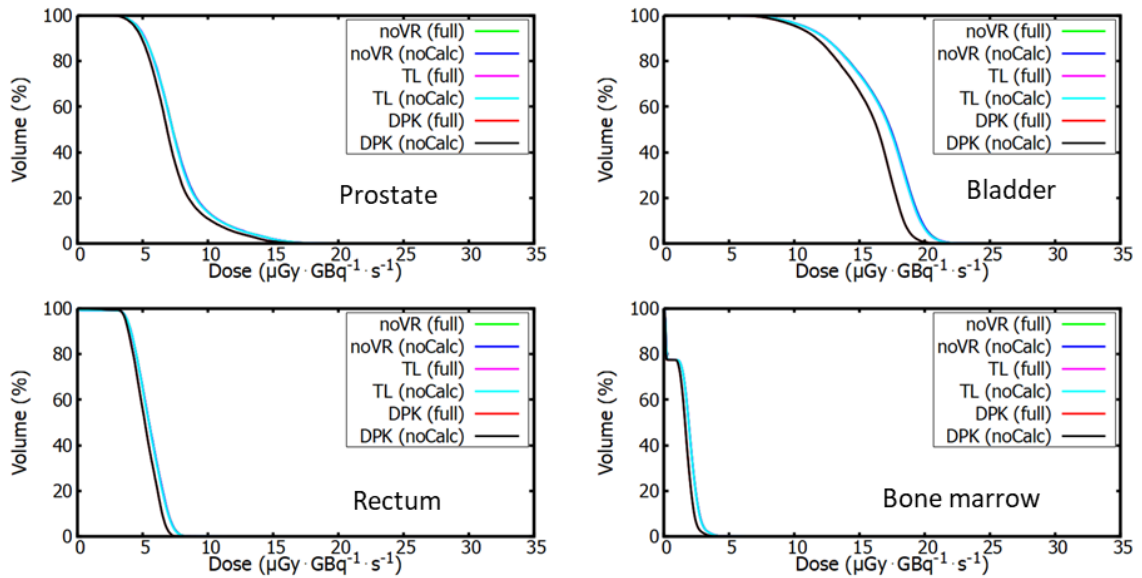


**Figure 4.24:** Dose-volume histograms derived from dose distribution calculated with density corrected DPK convolution calculations, noVR MC and TL MC using TIA matrices with full and no activity in calcifications for (A) prostate, (B) bladder, (C) rectum, and (D) bone marrow.

**Table 4.5:** Area under the DVH curve for the prostate and other organs at risk like the rectum, and bone marrow for the different dose calculation methods.

Organ	DPK without Den. Corr. ( $\mu\text{Gy} \cdot \text{GBq}^{-1} \cdot \text{s}^{-1}$ )	DPK ( $\mu\text{Gy} \cdot \text{GBq}^{-1} \cdot \text{s}^{-1}$ )	noVR ( $\mu\text{Gy} \cdot \text{GBq}^{-1} \cdot \text{s}^{-1}$ )
Prostate	4.39	4.54	5.20
Rectum	4.32	4.86	5.46
Bone marrow	1.75	1.41	1.68

To evaluate the agreement between the dose distribution calculated by the density corrected DPK convolution method and the standard of reference `egs_mird` MC simulation method, the areas of the dose-volume histograms for the four regions: the prostate, rectum, bladder, and bone marrow were compared. The mean relative errors of DVHs for prostate, rectum, bladder, and bone marrow were  $-5.55 \pm 0.79\%$ ,  $-5.36 \pm 1.32\%$ ,  $-5.83 \pm 0.50\%$  and  $-14.68 \pm 6.25\%$ , respectively. While for DPK

convolution without density the dose variation against noVR MC is  $-6.86 \pm 0.95\%$ ,  $-6.86 \pm 1.28\%$ ,  $-10.01 \pm 0.85\%$ , and  $6.48 \pm 2.85\%$  for prostate, rectum, bladder, and bone marrow respectively.

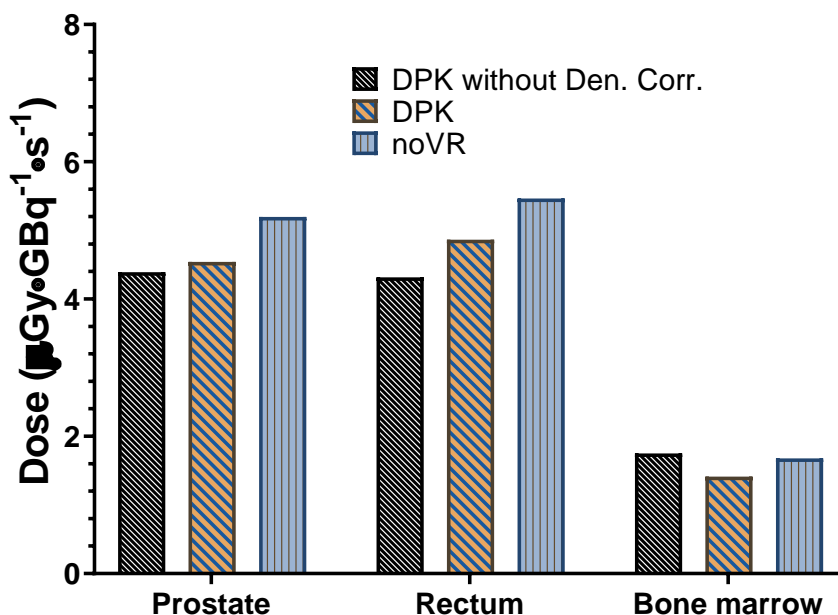


**Figure 4.25:** Organ-level absorbed doses estimated using DPK convolution with and without density correction compared to noVR MC.

The total TIA over the patient body was 1270.243 GBq·s. Table 4.5 is the mean absorbed dose under the DVH curve for the prostate, rectum, and bone marrow plotted in Figure 4.25.

## 4.4 Discussion

As currently practiced, patients in targeted radionuclide therapy are administered a fixed radionuclide activity regardless of their body weight and personalized radiation dose calculation from the administered activity is not performed. As a result, the tumor and critical organs could either be over- or under-dose leading to suboptimal treatment efficacy and/or increased rates of complications. Voxelized absorbed dose calculation is preferable to organ-level mean absorbed doses calculated with the MIRD formalism as hot and cold spots could be overlooked with the latter method. The Monte Carlo (MC)



simulation method is considered the gold standard for calculating voxelized absorbed doses in targeted radionuclide therapy. However, MC simulation is complex and computationally demanding if it is required for each patient.

In this work, a 3D FFT convolution method for voxel-level dose calculation method was developed for application in targeted radionuclide therapy and diagnostic nuclear medicine procedures. This method has been demonstrated in simulated  $^{177}\text{Lu}$  targeted radionuclide therapy for (N=6) six patients using the  $^{18}\text{F}$ ]DCFPyL or  $^{18}\text{F}$ ]FCH PET/CT data of each patient. Five patients were administered  $^{18}\text{F}$ ]DCFPyL and only one received  $^{18}\text{F}$ ]FCH.

The MC simulation used `egs_mird`, a EGSnrc MC application developed by Dr. M Martinov of our group.<sup>233</sup> The  $^{177}\text{Lu}$  3D dose point kernel in homogeneous prostate media at  $1.04\text{ g/cm}^3$  density was generated with `egs_mird`. The size of the kernel was 65 cm and photon energy loss in the kernel was roughly 1%. The patient absorbed dose was calculated by convolving the  $^{177}\text{Lu}$  dose point kernel dose with patient-specific time-integrated activity. The convolution calculated absorbed dose for each voxel was further scaled with the prostate density of  $1.04\text{ g/cm}^3$  divided by the real density values derived from the CT scan to correct for the density deviation of each voxel from the assumed prostate density. The density corrected DPK convolution absorbed dose results were compared with those of `egs_mird` MC.

The DPK convolution method can perform a TRT treatment simulation using a pre-calculated  $^{177}\text{Lu}$  DPK and patient-specific time-integrated activity data in 16.23 minutes with a single core of AMD Ryzen 9 3900XT processor. On the contrary, the `egs_mird` noVR Monte Carlo simulation took 28.47 minutes using 22 cores of the same Ryzen 9 3900XT processor.

Figure 4.6, Figure 4.13 and Figure 4.19 illustrate patients' CT,  $^{18}\text{F}$ ]DCFPyL, and  $^{18}\text{F}$ ]FCH PET data side by side. Due to the reduced spatial resolution, the calcifications are not as visible in the PET scans as they are on the CT scans for patients with calcified prostate regions. The 3D TIA map was derived from the dynamic PET data and represented a TIA across a 22-minute scan in each voxel.

Although the noise level in DPK convolution dose maps appeared to be the same as the egs\_mird MC dose maps shown in Figure 4.7, Figure 4.14 and Figure 4.20, the dose profiles from the DPK convolution dose map were less noisy than the egs\_mird MC dose map as shown in Figure 4.8 to Figure 4.9, Figure 4.15 and Figure 4.21 to Figure 4.22. The fluctuations in the dose profiles reflect the statistical uncertainties of the DPK convolution and MC dose calculations. While both noise in the TIA map and the MC simulation process contributed to the noise in egs\_mird dose maps, only that in the TIA map contributed to the noise in the DPK convolution dose map.

In this study, calcifications were modelled as an equal mix by mass of prostate tissue and pure calcification. Further, by assuming full and no activity in the calcifications, then the TIA in these calcified regions was halved and the corresponding dose declined by 40%. For all patients, the presence of calcifications in the prostate did not noticeably affect the immediately surrounding voxels, namely spurious increase or decrease of dose were not observed. It is worth noting that the pure calcification voxels still have dose deposition even when the TIA in them is set to zero, indicating that there is at least some dose contribution from adjacent non-calcification voxels. This is a strong indication that the reduced energy deposited in the P50C50 voxels would not be entirely localized within the prostate fraction of the voxel media if the different media in the voxel were to be modelled explicitly.

DPK convolution consistently demonstrated a lower dose compared to MC. This discrepancy between the models could stem from several factors. One factor is the PET scan noise which is the only substantial noise source that the DPK convolution must deal with, although the PET scan activity was up-sampled using linear interpolation from 128x128 to 512x512 resolution, improving the smoothness between neighboring voxels. Furthermore, the convolution kernel assumes that all voxels are prostate tissue with a density of 1.04 g/cm<sup>3</sup> and does not account for density variation. The tissue density inhomogeneities in the patient's body could contribute to systemic discrepancies between DPK convolution and MC calculated doses. Figure 4.10, Figure 4.16 and Figure 4.23 show the effect of a simple density correction performed on DPK convolution at the voxel level on accounting for density inhomogeneity. As a result of this correction, the

accuracy of the DPK convolution dose was improved relative to MC simulation, particularly for high-density objects, that is those whose density differs significantly from that used in the DPK simulation. Another factor is the variation in the mass energy absorption coefficient. For  $^{177}\text{Lu}$ , about 22% are photon decays, for these decays, the change in mass energy absorption coefficients with energy and media composition can further contribute to the discrepancy between DPK convolution and MC.

To verify that the DPK convolution and MC dose calculations agree when removing all the above discrepancies, simulations were performed using a radionuclide source that emits only 500 keV electrons. The simulation was performed with a cuboid phantom (65 cm)<sup>3</sup> in size that was uniformly filled with prostate media at a density of 1.03 g/cm<sup>3</sup>. The time-integrated activity per phantom voxel was also 1 Bq.s. The dose distribution in the phantom calculated with MC simulation was compared to that calculated with DPK convolution using prostate media and prostate density DPK. The two dose distributions agreed to within 0.2 %. Furthermore, there was no difference in dose calculated with DPK convolution and analytically. This comparison shows that when discrepancies in density inhomogeneity and other factors, e.g., mass energy absorption coefficient discussed above, are removed, the dose calculated by DPK convolution and MC simulation is the same. It also shows that DPK convolution dose calculation can be inaccurate in tissue/media with prominent density inhomogeneity, e.g., the lungs.

## 4.5 Conclusion

The present study demonstrates that DPK convolution can be used to calculate a patient-specific absorbed dose distribution in TRT using patient CT for the definition of patient geometry and density distribution and PET scans for integrated time activity distribution. Due to the difference in tissue media and densities, the DPK convolution dose for  $^{177}\text{Lu}$  TRT was approximately 5.6 % lower on average than the egs\_mird MC simulation dose for the prostate and rectum. As such, the DPK convolution method may not be suitable for TRT dose calculation for tumors within tissue regions of high-level inhomogeneities like bone or lung tissue regions. Further work is required to adapt DPK convolution to account for tissue media and density inhomogeneities.

## Chapter 5

### 5 Conclusion and Future Directions

#### 5.1 Summary

In many well-established MC codes, dose calculations are typically based on assumptions about patient geometry and activity distribution. We developed `egs_mird` for patient-specific targeted radionuclide therapy dosimetry, to overcome the challenges associated with other Monte Carlo codes. The purpose of this master's thesis is two-fold. Firstly, to validate `egs_mird` (an in-house Monte Carlo (MC) simulation code) and see if it agrees with well-established MC codes. Secondly, to develop a 3D voxel-level dose convolution algorithm and investigate whether it is fast and accurate for patient-specific TRT dosimetry in prostate cancer. `egs_mird` MC code was developed to calculate patient-specific absorbed dose distribution in TRT using patient CT for the definition of patient geometry and density distribution and PET scans for integrated time activity distribution.

I participated and contributed to the development of the `egs_mird` MC dosimetry program for internally distributed radionuclides by generating DPKs for  $^{90}\text{Y}$ ,  $^{131}\text{I}$  and  $^{177}\text{Lu}$  with the program and critically comparing the results with the literature. The DPKs showed good agreement, and the discrepancy between our  $^{177}\text{Lu}$  DPK and literature was due to differences in emission spectra. It illustrates the importance of using the correct emission spectrum when calculating DPKs.

I developed a 3D dose convolution algorithm to calculate 3D dose distributions of radionuclides using the dose point kernel (DPK) and the time-integrated activity (TIA) of the radionuclide. The 3D convolution algorithm 3D dose results were validated using analytical calculations and `egs_mird` MC simulation. The 3D dose distribution was in good agreement with analytical calculations (0%) and `egs_mird` MC simulations (0.2%-0.4%).

I used the 3D dose convolution algorithm and `egs_mird` MC simulation to calculate  $^{177}\text{Lu}$  TRT dose distributions in 3D for six patients. The DVHs were similar, but the mean

doses in the prostate and critical organs were 5-7% lower with DKP convolution than in the MC simulation. The reason is the density inhomogeneity. Moreover, an ad-hoc method for density correction brings the results closer to MC simulation in the calcified regions of the prostate, rectum and bladder than without the ad-hoc correction method. The comparison was worse for bone marrow.

## 5.2 DPK Convolution Density Correction

The TRT clinical practice relies on accurate TRT treatment planning systems based on absorbed dose distributions. The absorbed dose is affected by tissue heterogeneities and finite patient geometry.<sup>247</sup> DPK convolution depends on the dose point kernel, mostly in a homogeneous medium which limits absorbed dose accuracy. A more accurate dose convolution technique considers how ionizing radiation interacts with the body of the patient in the 3D spatial distribution of tissue heterogeneities.

Energy is deposited along the primary and secondary electron tracks as ionizing radiations (radionuclides used in TRT emit ionizing radiation such as photons, beta particles, electrons, alpha particles, etc.) interact with the body of the patient. These ionizing radiations frequently experience scattering processes and can participate in multiple scattering processes because of density variations before imparting all their energy to the patient's body or escaping.<sup>212</sup>

Future work will account for tissue density inhomogeneities by recalculation of the dose point kernel. Approximately, the kernel can be scaled by the prostate/water equivalent distance along rays between the source and dose-receiving points.<sup>248</sup> For most clinical situations, this method will provide a fast and sufficiently accurate way to incorporate inhomogeneities into 3D dose calculations, and it has been implemented in external beam radiotherapy. Instead of physical distance, the in-prostate/water kernel values are calculated along rays radiological distance using Equation 5.1.

$$\bar{k}(\mathbf{s}, \mathbf{r}) = \rho'_e(\mathbf{r})(\bar{\rho}'_e)^2 \bar{k}_p[\rho'_e(\mathbf{r} - \mathbf{s})] \quad 5.1$$

where  $\rho'_e(\mathbf{r}) = \rho_e(\mathbf{r})/\rho_e^p(\mathbf{r})$  is the local relative electron density at  $\mathbf{r}$ ,  $\bar{\rho}'_e$  is the average relative electron density along the path from point  $\mathbf{s}$  to  $\mathbf{r}$

$$\bar{\rho}'_e = \frac{\int_s^r \rho'_e(l) dl}{|\mathbf{r} - \mathbf{s}|} \quad 5.2$$

and  $\bar{k}_p$  is the kernel for a prostate or water medium.

The energy deposited per unit volume in the prostate is multiplied by the local relative electron density,  $\rho'_e(\mathbf{r})$  and the  $(\bar{\rho}'_e)^2$  the factor is used to compensate for the integrated inverse-square fall-off with physical distance in the values of the prostate or water kernels.

The dose-receiving point experiences a different density environment but stays at the same physical location relative to the source. From Equation 5.2, the integral  $\int_s^r \rho'_e(l) dl$  is the radiological distance, while the  $|\mathbf{r} - \mathbf{s}|$  is the geometric distance.

The 3D absorbed dose is now calculated by convolving the recalculated prostate or water kernel,  $\bar{k}(\mathbf{s}, \mathbf{r})$  (in Equation 5.1) with the time-integrated activity from each patient.

### 5.3 Estimation of Biological Effective Dose

The objective of dosimetry treatment-planning protocols in targeted radionuclide therapy is to prescribe a clinically useful absorbed dose to the tumor while at the same time avoiding organ toxicity. However, patients with rapid clearance of the radiopharmaceutical require a larger amount of initial activity than those with slow clearance to match the absorbed dose to the target and critical organ.<sup>249</sup> An increase in absorbed dose, arising from a large, administered activity may cause an unexpected increase in toxicity among the dose-limiting normal tissues, such as the red bone marrow and kidneys due to the more rapid clearance of radiopharmaceuticals from the body of a patient. Even though the total absorbed dose to a dose-limiting tissue remains constant, the absorbed dose can vary substantially among patients.<sup>249</sup>

Targeted radionuclide therapy dose delivery induces DNA damage both in the cancer cell and in normal tissues. DNA repair takes place faster in normal tissues than in cancer cells. The repair process in the interval between irradiation competes with the induction

of further DNA sublethal damage leading to a more lethal effect by the ongoing irradiation.<sup>250</sup> Thus, a more general model is required to account for the biological impact of different absorbed doses. These effects may be accounted for through the biological effective dose (BED). BED may be applied to evaluate how radiation delivery in TRT might impact on overall balance between the probabilities of tumor cure and normal-tissue complications.<sup>250–253</sup> The BED is the dose required for a given biological effect when delivered by infinitely small doses per fraction or at very low doses and is typically used to compare the response implications of total absorbed doses delivered at different doses. BED also relates absorbed dose with radiosensitivity and repair of radiation damage using the standard linear quadratic model.<sup>254</sup> In future work, BED modeling will be implemented to account for the impact of targeted radionuclide therapy on the target organ, prostate, dose-limiting organs, and other organs at risk.

## 5.4 Estimation of Time-Integrated Activity

Dosimetry for radionuclide therapy involves calculating the time-integrated activity. Time-integrated activity for current work is estimated using a PET study acquired within five-time points (~22 minutes). For calculating absorbed doses, future work will account for time-integrated activity until radiopharmaceuticals are eliminated from the body.

In most cases, blood samplings are taken to determine the level of activity in the blood.<sup>255</sup> (including various organs) and to estimate the biological half-life of radiopharmaceuticals in the body. Using Equation 5.3, we can estimate the time-integrated activity of radiopharmaceuticals administered to a patient from the time of administration to the time of elimination.

$$TIA(x_i, y_j, z_k) = \int_0^{\infty} A(x_i, y_j, z_k, t) dt \quad 5.3$$

The time-integrated activity  $TIA(x_i, y_j, z_k)$  can be calculated using exponential extrapolation and kinetic modelling.

### 5.4.1 Exponential Extrapolation

The exponential extrapolation of  $TA(x_i, y_j, z_k, t)$  is based on the fitting from the peak ( $t = t_p$ ) to  $t = t_e$  where  $t_e$  is the end of the measurement. Let the extrapolated curve be  $TA_e(x_i, y_j, z_k, t)$ , then:

$$TIA(x_i, y_j, z_k) = \int_0^{t_e} TA(x_i, y_j, z_k, t) dt + \int_{t_e}^{\infty} TA_e(x_i, y_j, z_k, t) dt \quad 5.4$$

where  $\infty$  is the shorter of five biological or physical half-lives of the radionuclide at voxel  $(x_i, y_j, z_k)$ .

### 5.4.2 From Kinetic Modelling

$$TIA(x_i, y_j, z_k) = \int_0^{\infty} TA(x_i, y_j, z_k, t) dt = \left[ \int_0^{\infty} C_a(t) dt \right] \cdot \left[ \int_0^{\infty} R_F(x_i, y_j, z_k, t) dt \right] \quad 5.5$$

where  $C_a(t)$  is the arterial curve and  $R_F(x_i, y_j, z_k, t)$  is the flow-scaled impulse residue function, that is,

$$TA(x_i, y_j, z_k, t) = C_a(t) \otimes R_F(x_i, y_j, z_k, t)$$

where  $\otimes$  is the convolution operator. It can be shown that:

$$\int_0^{\infty} R_F(x_i, y_j, z_k, t) dt = V_b(x_i, y_j, z_k) + V_D(x_i, y_j, z_k) = V_T(x_i, y_j, z_k) \quad 5.6$$

where  $V_b(x_i, y_j, z_k)$  is the blood volume,  $V_D(x_i, y_j, z_k)$  is the Logan distribution volume, and  $V_T(x_i, y_j, z_k)$  is the total distribution volume. Since  $\int_0^{\infty} C_a(t) dt = K_c$  is a constant, Equation 5.5 shows that  $TIA(x_i, y_j, z_k)$  is proportional to  $V_T(x_i, y_j, z_k)$ . Therefore, as shown in Equation 2.9 in §2.3.31,  $P(x_i, y_j, z_k)$  can also be determined with  $V_T(x_i, y_j, z_k)$ , or `egs_mird` can use  $V_T(x_i, y_j, z_k)$  instead of  $TIA(x_i, y_j, z_k)$  to calculate the normalized dose,  $MC_{norm}(x, y, z)$ , or the dose per decay. As in Equation 5.4:



$$\int_0^{\infty} C_a(t)dt = \int_0^{t_e} C_a(t)dt + \int_{t_e}^{\infty} C_{ae}(t)dt \quad \mathbf{5.7}$$

where  $t_e$  is the end of the measurement of  $C_a(t)$  and  $C_{ae}(t)$  is the exponential extrapolation of  $C_a(t)$  based on the fitting from the peak ( $t = t_p$ ) to  $t = t_e$ .

## References

1. Schatten H, Wiedemeier A, Taylor M, et al. Centrosome-centriole abnormalities are markers for abnormal cell divisions and cancer in the transgenic adenocarcinoma mouse prostate (TRAMP) model. *Biol Cell*. 2000;92(5):331-340. doi:10.1016/S0248-4900(00)01079-0
2. Gu G, Yuan J, Wills M, Kasper S. Prostate Cancer Cells with Stem Cell Characteristics Reconstitute the Original Human Tumor In vivo. *Cancer Res*. 2007;67(10):4807-4815. doi:10.1158/0008-5472.CAN-06-4608
3. LeBlanc AG, Demers A, Shaw A. Recent trends in prostate cancer in Canada. *Heal Reports*. 2019;30(4):12-17.
4. Adams, John. "The case of scirrhus of the prostate gland with corresponding affliction of the lymphatic glands in the lumbar region and in the pelvis." *Lancet* 1.1 (1853): 393-393.
5. LeBlanc AG, Demers A, Shaw A. Recent trends in prostate cancer in Canada. *Heal Reports*. 2019;30(4):12-17. doi:10.25318/82-003-X201900400002-ENG
6. Canadian Cancer Statistics Advisory Committee. (2019). Canadian cancer statistics 2019. Toronto, ON: Canadian Cancer Society.
7. Statistics Canada. Table 13-10-0747-01 (formerly CANSIM 103-0554) Number of new cases and age-standardized rates of primary cancer, by cancer type and sex. Release date: 2021-05-19.
8. Abid, Z., A.J. Cross, and R. Sinha, Meat, dairy, and cancer. *Am J Clin Nutr*, 2014. 100 Suppl 1: p. 386s-93s.
9. Carruba G, Cocciadiferro L, Di Cristina A, et al. Nutrition, aging and cancer: lessons from dietary intervention studies. *Immun Ageing*. 2016;13(1):13. doi:10.1186/s12979-016-0069-9
10. Bylsma LC, Alexander DD. A review and meta-analysis of prospective studies of red and processed meat, meat cooking methods, heme iron, heterocyclic amines and prostate cancer. *Nutr J*. 2015;14(1):125. doi:10.1186/s12937-015-0111-3
11. Bashir MN. Epidemiology of Prostate Cancer. *Asian Pacific J Cancer Prev*. 2015;16(13):5137-5141. doi:10.7314/APJCP.2015.16.13.5137
12. Kimura T, Egawa S. Epidemiology of prostate cancer in Asian countries. *Int J Urol*. 2018;25(6):524-531. doi:10.1111/iju.13593
13. Crawford ED. Epidemiology of prostate cancer. *Urology*. 2003;62(6):3-12. doi:10.1016/j.urology.2003.10.013
14. Carter HB, Piantadosi S, Isaacs JT. Clinical Evidence for and Implications of the Multistep Development of Prostate Cancer. *J Urol*. 1990;143(4):742-746. doi:10.1016/S0022-5347(17)40078-4
15. Stratton MR, Campbell PJ, Futreal PA. The cancer genome. *Nature*.

- 2009;458(7239):719-724. doi:10.1038/nature07943
16. Nettey OS, Walker AJ, Keeter MK, et al. Self-reported Black race predicts significant prostate cancer independent of clinical setting and clinical and socioeconomic risk factors. *Urol Oncol Semin Orig Investig*. 2018;36(11):501.e1-501.e8. doi:10.1016/j.urolonc.2018.06.011
  17. Oczkowski M, Dziendzikowska K, Pasternak-Winiarska A, Włodarek D, Gromadzka-Ostrowska J. Dietary Factors and Prostate Cancer Development, Progression, and Reduction. *Nutrients*. 2021;13(2):496. doi:10.3390/nu13020496
  18. Fontana F, Anselmi M, Limonta P. Molecular mechanisms and genetic alterations in prostate cancer: From diagnosis to targeted therapy. *Cancer Lett*. 2022;534:215619. doi:10.1016/j.canlet.2022.215619
  19. Valenciano A, Henríquez-Hernández LA, Moreno M, Lloret M, Lara PC. Role of IGF-1 Receptor in Radiation Response. *Transl Oncol*. 2012;5(1):1-9. doi:10.1593/tlo.11265
  20. Wilkenfeld SR, Lin C, Frigo DE. Communication between genomic and non-genomic signaling events coordinate steroid hormone actions. *Steroids*. 2018;133:2-7. doi:10.1016/j.steroids.2017.11.005
  21. Termini D, Den Hartogh DJ, Jaglanian A, Tsiani E. Curcumin against Prostate Cancer: Current Evidence. *Biomolecules*. 2020;10(11):1536. doi:10.3390/biom10111536
  22. Wang D, Hu L, Zhang G, Zhang L, Chen C. G protein-coupled receptor 30 in tumor development. *Endocrine*. 2010;38(1):29-37. doi:10.1007/s12020-010-9363-z
  23. Luo J, Liu D. Does GPER Really Function as a G Protein-Coupled Estrogen Receptor in vivo? *Front Endocrinol (Lausanne)*. 2020;11:148. doi:10.3389/fendo.2020.00148
  24. Chen CD, Welsbie DS, Tran C, et al. Molecular determinants of resistance to antiandrogen therapy. *Nat Med*. 2004;10(1):33-39. doi:10.1038/nm972
  25. Gregory CW, Raymond T, Johnson Jr, James L, Mohler FS, French, Elizabeth M, Wilson. Androgen receptor stabilization in recurrent prostate cancer is associated with hypersensitivity to low androgen. *Cancer Res*. 2001;7(61):2892-2898.
  26. Schulz WA. Molecular biology of prostate cancer. *Mol Hum Reprod*. 2003;9(8):437-448. doi:10.1093/molehr/gag064
  27. Kennedy J, Chicheportiche A, Keidar Z. Quantitative SPECT/CT for Dosimetry of Peptide Receptor Radionuclide Therapy. *Semin Nucl Med*. 2022;52(2):229-242. doi:10.1053/J.SEMNUCLMED.2021.11.004
  28. Bray F, Ferlay J, Soerjomataram I, Siegel RL, Torre LA, Jemal A. Global cancer statistics 2018: GLOBOCAN estimates of incidence and mortality worldwide for 36 cancers in 185 countries. *CA Cancer J Clin*. 2018;68(6):394-424. doi:10.3322/CAAC.21492

29. Agnihotri S, Mittal RD, Kapoor R, Mandhani A. Asymptomatic prostatic inflammation in men with clinical BPH and erectile dysfunction affects the positive predictive value of prostate-specific antigen. *Urol Oncol Semin Orig Investig.* 2014;32(7):946-951. doi:10.1016/J.UROLONC.2014.03.004
30. DeZeeuw J, O'Regan NB, Goudie C, Organ M, Dubrowski A. Anatomical 3D-Printed Silicone Prostate Gland Models and Rectal Examination Task Trainer for the Training of Medical Residents and Undergraduate Medical Students. *Cureus.* 2020;12(7). doi:10.7759/CUREUS.9020
31. Catalona WJ. Prostate Cancer Screening. *Med Clin North Am.* 2018;102(2):199. doi:10.1016/J.MCNA.2017.11.001
32. Catalona WJ, Hudson MA, Scardino PT, et al. Selection of Optimal Prostate Specific Antigen Cutoffs for Early Detection of Prostate Cancer: Receiver Operating Characteristic Curves. *J Urol.* 1994;152(6):2037-2042. doi:10.1016/S0022-5347(17)32300-5
33. Barsouk A, Padala SA, Vakiti A, et al. Epidemiology, Staging and Management of Prostate Cancer. *Med Sci 2020, Vol 8, Page 28.* 2020;8(3):28. doi:10.3390/MEDSCI8030028
34. Finne P, Finne R, Bangma C, et al. Algorithms based on prostate-specific antigen (PSA), free PSA, digital rectal examination and prostate volume reduce false-positive PSA results in prostate cancer screening. *Int J Cancer.* 2004;111(2):310-315. doi:10.1002/IJC.20250
35. Bell N, Connor Gorber S, Shane A, et al. Recommendations on screening for prostate cancer with the prostate-specific antigen test. *CMAJ.* 2014;186(16):1225-1234. doi:10.1503/CMAJ.140703/-/DC1
36. van der Leest M, Cornel E, Israël B, et al. Head-to-head Comparison of Transrectal Ultrasound-guided Prostate Biopsy Versus Multiparametric Prostate Resonance Imaging with Subsequent Magnetic Resonance-guided Biopsy in Biopsy-naïve Men with Elevated Prostate-specific Antigen: A Large Prospective Multicenter Clinical Study. *Eur Urol.* 2019;75(4):570-578. doi:10.1016/J.EURURO.2018.11.023
37. Choi YH, Kang MY, Sung HH, et al. Comparison of Cancer Detection Rates Between TRUS-Guided Biopsy and MRI-Targeted Biopsy According to PSA Level in Biopsy-Naïve Patients: A Propensity Score Matching Analysis. *Clin Genitourin Cancer.* 2019;17(1):e19-e25. doi:10.1016/J.CLGC.2018.09.007
38. Buyyounouski MK, Choyke PL, McKenney JK, et al. Prostate cancer – major changes in the American Joint Committee on Cancer eighth edition cancer staging manual. *CA Cancer J Clin.* 2017;67(3):245-253. doi:10.3322/CAAC.21391
39. Telloni SM. Tumor staging and grading: A primer. *Methods Mol Biol.* 2017;1606:1-17. doi:10.1007/978-1-4939-6990-6\_1/FIGURES/5
40. Cheng L, Montironi R, Bostwick DG, Lopez-Beltran A, Berney DM. Staging of prostate cancer. *Histopathology.* 2012;60(1):87-117. doi:10.1111/J.1365-2559.2011.04025.X

41. Ohori M, Wheeler TM, Scardino PT. The New American Joint Committee on Cancer and International Union Against Cancer TNM Classification of Prostate Cancer Clinicopathologic Correlations. doi:10.1002/1097-0142
42. Montie JE. Staging of Prostate Cancer Current TNM Classification and Future Prospects for Prognostic Factors. *Am Jt Comm Cancer*. Published online 1992. doi:10.1002/1097-0142
43. Humphrey PA. Gleason grading and prognostic factors in carcinoma of the prostate. *Mod Pathol 2004 173*. 2004;17(3):292-306. doi:10.1038/modpathol.3800054
44. Heidenreich A, Aus G, Bolla M, et al. EAU Guidelines on Prostate Cancer. *Eur Urol*. 2008;53(1):68-80. doi:10.1016/J.EURURO.2007.09.002
45. Dunn MW, Kazer MW. Prostate Cancer Overview. *Semin Oncol Nurs*. 2011;27(4):241-250. doi:10.1016/J.SONCN.2011.07.002
46. WALLACE DM, CHISHOLM GD, HENDRY WF. T.N.M. Classification for Urological Tumours (U.I.C.C.)—1974. *Br J Urol*. 1975;47(1):1-12. doi:10.1111/J.1464-410X.1975.TB03911.X
47. Makarov D V., Trock BJ, Humphreys EB, et al. Updated Nomogram to Predict Pathologic Stage of Prostate Cancer Given Prostate-Specific Antigen Level, Clinical Stage, and Biopsy Gleason Score (Partin Tables) Based on Cases from 2000 to 2005. *Urology*. 2007;69(6):1095-1101. doi:10.1016/J.UROLOGY.2007.03.042
48. Humphrey PA. Gleason grading and prognostic factors in carcinoma of the prostate. *Mod Pathol 2004 173*. 2004;17(3):292-306. doi:10.1038/modpathol.3800054
49. Linkon AHM, Labib MM, Hasan T, Hossain M, Jannat ME. Deep learning in prostate cancer diagnosis and Gleason grading in histopathology images: An extensive study. *Informatics Med Unlocked*. 2021;24:100582. doi:10.1016/J.IMU.2021.100582
50. Thompson I, Thrasher JB, Aus G, et al. Guideline for the Management of Clinically Localized Prostate Cancer: 2007 Update. *J Urol*. 2007;177(6):2106-2131. doi:10.1016/J.JURO.2007.03.003
51. Arvaniti E, Fricker KS, Moret M, et al. Automated Gleason grading of prostate cancer tissue microarrays via deep learning. *Sci Reports 2018 81*. 2018;8(1):1-11. doi:10.1038/s41598-018-30535-1
52. Khoo VS, Padhani AR, Tanner SF, Finnigan DJ, Leach MO, Dearnaley DP. Comparison of MRI with CT for the radiotherapy planning of prostate cancer: A feasibility study. *Br J Radiol*. 1999;72(JUN.):590-597. doi:10.1259/BJR.72.858.10560342
53. Zhang Q, Zang S, Zhang C, et al. Comparison of 68Ga-PSMA-11 PET-CT with mpMRI for preoperative lymph node staging in patients with intermediate to high-risk prostate cancer. *J Transl Med*. 2017;15(1). doi:10.1186/S12967-017-1333-2

54. Briganti A, Abdollah F, Nini A, et al. Performance Characteristics of Computed Tomography in Detecting Lymph Node Metastases in Contemporary Patients with Prostate Cancer Treated with Extended Pelvic Lymph Node Dissection. *Eur Urol*. 2012;61(6):1132-1138. doi:10.1016/J.EURURO.2011.11.008
55. Brady Z, Taylor ML, Haynes M, et al. The clinical application of PET/CT: A contemporary review. *Australas Phys Eng Sci Med*. 2008;31(2):90-109. doi:10.1007/BF03178584
56. Stabile A, Giganti F, Rosenkrantz AB, et al. Multiparametric MRI for prostate cancer diagnosis: current status and future directions. *Nat Rev Urol* 2019 171. 2019;17(1):41-61. doi:10.1038/s41585-019-0212-4
57. Moschini M, Briganti A, Murphy CR, et al. Outcomes for Patients with Clinical Lymphadenopathy Treated with Radical Prostatectomy. *Eur Urol*. 2016;69(2):193-196. doi:10.1016/J.EURURO.2015.07.047
58. Hara N, Okuizumi M, Koike H, Kawaguchi M, Bilim V. Dynamic contrast-enhanced magnetic resonance imaging (DCE-MRI) is a useful modality for the precise detection and staging of early prostate cancer. *Prostate*. 2005;62(2):140-147. doi:10.1002/PROS.20124
59. SAWAYAMA H, ISHIMOTO T, SUGIHARA H, et al. Clinical impact of the Warburg effect in gastrointestinal cancer (Review). *Int J Oncol*. 2014;45(4):1345-1354. doi:10.3892/ijo.2014.2563
60. Warburg O, Wind F, Negelein E. THE METABOLISM OF TUMORS IN THE BODY. *J Gen Physiol*. 1927;8(6):519. doi:10.1085/JGP.8.6.519
61. Jemal A, Siegel R, Ward E, et al. Cancer Statistics, 2006. *CA Cancer J Clin*. 2006;56(2):106-130. doi:10.3322/canjclin.56.2.106
62. Parent EE, Schuster DM. Update on 18 F-Fluciclovine PET for Prostate Cancer Imaging. *J Nucl Med*. 2018;59(5):733-739. doi:10.2967/jnumed.117.204032
63. Zhu A, Lee D, Shim H. Metabolic Positron Emission Tomography Imaging in Cancer Detection and Therapy Response. *Semin Oncol*. 2011;38(1):55-69. doi:10.1053/j.seminoncol.2010.11.012
64. Chen R, Wang Y, Shi Y, et al. Diagnostic value of 18F-FDG PET/CT in patients with biochemical recurrent prostate cancer and negative 68Ga-PSMA PET/CT. *Eur J Nucl Med Mol Imaging*. 2021;48(9):2970-2977. doi:10.1007/s00259-021-05221-6
65. Jadvar H. Is There Use for FDG-PET in Prostate Cancer? *Semin Nucl Med*. 2016;46(6):502-506. doi:10.1053/j.semnuclmed.2016.07.004
66. Bouchelouche K, Tagawa ST, Goldsmith SJ, Turkbey B, Capala J, Choyke P. PET/CT Imaging and Radioimmunotherapy of Prostate Cancer. *Semin Nucl Med*. 2011;41(1):29-44. doi:10.1053/J.SEMNUCLMED.2010.08.005
67. Beheshti M, Rezaee A, Geinitz H, Loidl W, Pirich C, Langsteger W. Evaluation of Prostate Cancer Bone Metastases with 18 F-NaF and 18 F-Fluorocholine PET/CT. *J Nucl Med*. 2016;57:55-60. doi:10.2967/jnumed.115.169730

68. Brogsitter C, Zöphel K, Kotzerke J. 18F-Choline, 11C-choline and 11C-acetate PET/CT: Comparative analysis for imaging prostate cancer patients. *Eur J Nucl Med Mol Imaging*. 2013;40(SUPPL. 1). doi:10.1007/S00259-013-2358-2
69. Husarik DB, Miralbell R, Dubs M, et al. Evaluation of [18F]-choline PET/CT for staging and restaging of prostate cancer. *Eur J Nucl Med Mol Imaging*. 2008;35(2):253-263. doi:10.1007/S00259-007-0552-9
70. Ehman EC, Johnson GB, Villanueva-Meyer JE, et al. PET/MRI: Where might it replace PET/CT? *J Magn Reson Imaging*. 2017;46(5):1247-1262. doi:10.1002/JMRI.25711
71. Queiroz MA, Hüllner M, Kuhn F, et al. PET/MRI and PET/CT in follow-up of head and neck cancer patients. *Eur J Nucl Med Mol Imaging*. 2014;41(6):1066-1075. doi:10.1007/S00259-014-2707-9
72. Evangelista L, Zattoni F, Cassarino G, et al. PET/MRI in prostate cancer: a systematic review and meta-analysis. *Eur J Nucl Med Mol Imaging*. 2021;48(3):859-873. doi:10.1007/s00259-020-05025-0
73. Zhao J, Hamm B, Brenner W, Makowski MR. Lesion-to-background ratio threshold value of SUVmax of simultaneous [68Ga]Ga-PSMA-11 PET/MRI imaging in patients with prostate cancer. *Insights Imaging*. 2020;11(1):137. doi:10.1186/s13244-020-00926-y
74. Zamboglou C, Wieser G, Hennies S, et al. MRI versus 68Ga-PSMA PET/CT for gross tumour volume delineation in radiation treatment planning of primary prostate cancer. *Eur J Nucl Med Mol Imaging*. 2016;43(5):889-897. doi:10.1007/s00259-015-3257-5
75. Scobioala S, Kittel C, Wolters H, et al. Diagnostic efficiency of hybrid imaging using PSMA ligands, PET/CT, PET/MRI and MRI in identifying malignant prostate lesions. *Ann Nucl Med*. 2021;35(5):628-638. doi:10.1007/s12149-021-01606-7
76. Wang R, Shen G, Yang R, Ma X, Tian R. 68Ga-PSMA PET/MRI for the diagnosis of primary and biochemically recurrent prostate cancer: A meta-analysis. *Eur J Radiol*. 2020;130:109131. doi:10.1016/j.ejrad.2020.109131
77. Lawrentschuk N, Klotz L. Active surveillance for low-risk prostate cancer: an update. *Nat Rev Urol*. 2011;8(6):312-320. doi:10.1038/nrurol.2011.50
78. Keyes M, Crook J, Frcpc MD, et al. Clinical Review Treatment options for localized prostate cancer. *Can Fam Physician*. 2013;59:1269-1274.
79. Klotz L. Active Surveillance for Prostate Cancer: Patient Selection and Management. *Curr Oncol*. 2010;17(12):11-17. doi:10.3747/co.v17i0.713
80. Hayes JH, Ollendorf DA, Pearson SD, et al. Active Surveillance Compared With Initial Treatment for Men With Low-Risk Prostate Cancer. *JAMA*. 2010;304(21):2373. doi:10.1001/jama.2010.1720
81. Shekarriz B, Upadhyay J, Wood DP. INTRAOPERATIVE, PERIOPERATIVE, AND LONG-TERM COMPLICATIONS OF RADICAL PROSTATECTOMY.

- Urol Clin North Am.* 2001;28(3):639-653. doi:10.1016/S0094-0143(05)70168-3
82. Mofid B, Rezaeizadeh H, Jaladat AM, et al. Preventive effect of Malva on urinary toxicity after radiation therapy in prostate cancer patients: A multi-centric, double-blind, randomized clinical trial. *Electron Physician.* 2015;7(5):1220.
  83. Hsiao CP, Moore IMK, Insel KC, Merkle CJ. Symptom self-management strategies in patients with non-metastatic prostate cancer. *J Clin Nurs.* 2014;23(3-4):440-449. doi:10.1111/jocn.12178
  84. Michaelson MD, Cotter SE, Gargollo PC, Zietman AL, Dahl DM, Smith MR. Management of Complications of Prostate Cancer Treatment. *CA Cancer J Clin.* 2008;58(4):196-213. doi:10.3322/CA.2008.0002
  85. Acar C, Schoffelmeer CC, Tillier C, de Blok W, van Muilekom E, van der Poel HG. Quality of Life in Patients with Low-Risk Prostate Cancer. A Comparative Retrospective Study: Brachytherapy Versus Robot-Assisted Laparoscopic Prostatectomy Versus Active Surveillance. *J Endourol.* 2014;28(1):117-124. doi:10.1089/end.2013.0349
  86. Martinez AA, Gustafson G, Gonzalez J, et al. Dose escalation using conformal high-dose-rate brachytherapy improves outcome in unfavorable prostate cancer. *Int J Radiat Oncol.* 2002;53(2):316-327. doi:10.1016/S0360-3016(02)02733-5
  87. Blasko JC, Mate T, Sylvester JE, Grimm PD, Cavanagh W. Brachytherapy for carcinoma of the prostate: Techniques, patient selection, and clinical outcomes. *Semin Radiat Oncol.* 2002;12(1):81-94. doi:10.1053/srao.2002.28667
  88. Cormack RA, Kooy H, Tempany CM, D'Amico A V. A clinical method for real-time dosimetric guidance of transperineal 125i prostate implants using interventional magnetic resonance imaging. *Int J Radiat Oncol.* 2000;46(1):207-214. doi:10.1016/S0360-3016(99)00422-8
  89. Grills IS, Martinez AA, Hollander M, et al. High Dose Rate Brachytherapy as Prostate Cancer Monotherapy Reduces Toxicity Compared to Low Dose Rate Palladium Seeds. *J Urol.* 2004;171(3):1098-1104. doi:10.1097/01.JU.0000113299.34404.22
  90. Martell K, Kollmeier MA. Complications and side effects of high-dose-rate prostate brachytherapy. *Brachytherapy.* 2021;20(5):966-975. doi:10.1016/j.brachy.2020.10.007
  91. Stone N. Complications Following Permanent Prostate Brachytherapy. *Eur Urol.* 2002;41(4):427-433. doi:10.1016/S0302-2838(02)00019-2
  92. Pignot G, Maillet D, Gross E, et al. Systemic treatments for high-risk localized prostate cancer. *Nat Rev Urol.* 2018;15(8):498-510. doi:10.1038/s41585-018-0017-x
  93. Saad F, Hotte SJ. Guidelines for the management of castrate-resistant prostate cancer. *Can Urol Assoc J.* 2010;4(6):380-384. doi:10.5489/cuaj.10167
  94. Nygren P. What is cancer chemotherapy? *Acta Oncol (Madr).* 2001;40(2-3):166-174. doi:10.1080/02841860151116204



95. Pienta KJ, Smith DC. Advances in Prostate Cancer Chemotherapy: A New Era Begins. *CA Cancer J Clin.* 2005;55(5):300-318. doi:10.3322/CANJCLIN.55.5.300
96. Gilligan T, Kantoff PW. Chemotherapy for prostate cancer. *Urology.* 2002;60(3):94-100. doi:10.1016/S0090-4295(02)01583-2
97. Teo MY, Rathkopf DE, Kantoff P. Treatment of advanced prostate cancer. *Annu Rev Med.* 2019;70:479-499. doi:10.1146/ANNUREV-MED-051517-011947
98. Pagliarulo V, Bracarda S, Eisenberger MA, et al. Contemporary Role of Androgen Deprivation Therapy for Prostate Cancer. *Eur Urol.* 2012;61(1):11-25. doi:10.1016/J.EURURO.2011.08.026
99. Nguyen PL, Alibhai SMH, Basaria S, et al. Adverse Effects of Androgen Deprivation Therapy and Strategies to Mitigate Them. *Eur Urol.* 2015;67(5):825-836. doi:10.1016/J.EURURO.2014.07.010
100. Allan CA, Collins VR, Frydenberg M, McLachlan RI, Matthiesson KL. Androgen deprivation therapy complications. *Endocr Relat Cancer.* 2014;21(4):T119-T129. doi:10.1530/ERC-13-0467
101. Schwandt A, Garcia JA. Complications of androgen deprivation therapy in prostate cancer. *Curr Opin Urol.* 2009;19(3):322-326. doi:10.1097/MOU.0B013E32832A082C
102. Curcio CG, Vasile C, Gianciotta A, et al. Short term results of combined radioimmunotherapy in inoperable lung cancer. *Tumori.* 1976;62(6):587-598. doi:10.1177/030089167606200602
103. Gallivanone F, Valente M, Savi A, Canevari C, Castiglioni I. Targeted radionuclide therapy: Frontiers in theranostics. *Front Biosci - Landmark.* 2017;22(10):1750-1759. doi:10.2741/4569
104. Krasikova RN. Potential of PET in Tumor Theranostics. *Radiochemistry.* 2019;61(6):645-655. doi:10.1134/S1066362219060018
105. Hertz S, Roberts A, Evans RD. Radioactive Iodine as an Indicator in the Study of Thyroid Physiology. *Exp Biol Med.* 1938;38(4):510-513. doi:10.3181/00379727-38-9915P
106. HERTZ S. RADIOACTIVE IODINE IN THE STUDY OF THYROID PHYSIOLOGY. *J Am Med Assoc.* 1946;131(2):81. doi:10.1001/jama.1946.02870190005002
107. SEIDLIN SM. RADIOACTIVE IODINE THERAPY. *J Am Med Assoc.* 1946;132(14):838. doi:10.1001/jama.1946.02870490016004
108. Noto RB, Pryma DA, Jensen J, et al. Phase 1 Study of High-Specific-Activity I-131 MIBG for Metastatic and/or Recurrent Pheochromocytoma or Paraganglioma. *J Clin Endocrinol Metab.* 2018;103(1):213-220. doi:10.1210/JC.2017-02030
109. Fisher RI, Kaminski MS, Wahl RL, et al. Tositumomab and iodine-131 tositumomab produces durable complete remissions in a subset of heavily pretreated patients with low-grade and transformed non-Hodgkin's lymphomas. *J*

- Clin Oncol.* 2005;23(30):7565-7573. doi:10.1200/JCO.2004.00.9217
110. Goldsmith SJ. Radioimmunotherapy of Lymphoma: Bexxar and Zevalin. *Semin Nucl Med.* 2010;40(2):122-135. doi:10.1053/J.SEMNUCLMED.2009.11.002
  111. Goldsmith SJ. Targeted Radionuclide Therapy: A Historical and Personal Review. *Semin Nucl Med.* 2020;50(1):87-97. doi:10.1053/J.SEMNUCLMED.2019.07.006
  112. de Jong M, Valkema R, Jamar F, et al. Somatostatin receptor-targeted radionuclide therapy of tumors: Preclinical and clinical findings. *Semin Nucl Med.* 2002;32(2):133-140. doi:10.1053/snuc.2002.31027
  113. Kwekkeboom DJ, Teunissen JJ, Bakker WH, et al. Radiolabeled somatostatin analog [177Lu-DOTA0, Tyr3]octreotate in patients with endocrine gastroenteropancreatic tumors. *J Clin Oncol.* 2005;23(12):2754-2762. doi:10.1200/JCO.2005.08.066
  114. Romer A, Seiler D, Marincek N, et al. Somatostatin-based radiopeptide therapy with [177Lu-DOTA]-TOC versus [90Y-DOTA]-TOC in neuroendocrine tumours. *Eur J Nucl Med Mol Imaging.* 2014;41(2):214-222. doi:10.1007/S00259-013-2559-8
  115. Kassis AI, Adelstein SJ. Radiobiologic Principles in Radionuclide Therapy. *J Nucl Med.* 2005;46(1 suppl):4S-12S.
  116. Kuroda I. Effective use of strontium-89 in osseous metastases. *Ann Nucl Med.* 2012;26(3):197-206. doi:10.1007/S12149-011-0560-5
  117. Gudkov S, Shilyagina N, Vodenev V, Zvyagin A. Targeted Radionuclide Therapy of Human Tumors. *Int J Mol Sci.* 2015;17(1):33. doi:10.3390/ijms17010033
  118. Dash A, F. (Russ) Knapp F, R.A. Pillai M. Targeted Radionuclide Therapy - An Overview. *Curr Radiopharm.* 2013;6(3):152-180.
  119. Goldsmith SJ. Targeted Radionuclide Therapy: A Historical and Personal Review. *Semin Nucl Med.* 2020;50(1):87-97. doi:10.1053/j.semnuclmed.2019.07.006
  120. Zweit J. Radionuclides and carrier molecules for therapy. *Phys Med Biol.* 1996;41(10):1905-1914. doi:10.1088/0031-9155/41/10/004
  121. Ghahramani-Asl R, Razghandi F, Sadoughi HR. Dosimetric evaluation of several candidate radionuclides used in radionuclide therapy of bone metastases in an upper leg model. *Radiat Phys Chem.* 2020;176:109082. doi:10.1016/j.radphyschem.2020.109082
  122. Parker C, Gillessen S, Heidenreich A, Horwich A. Cancer of the prostate: ESMO Clinical Practice Guidelines for diagnosis, treatment and follow-up. *Ann Oncol.* 2015;26:v69-v77. doi:10.1093/annonc/mdv222
  123. Troyer JK, Beckett M Lou, Wright GL. Location of prostate-specific membrane antigen in the LNCaP prostate carcinoma cell line. *Prostate.* 1997;30(4):232-242. doi:10.1002/(SICI)1097-0045(19970301)30:4<232::AID-PROS2>3.0.CO;2-N
  124. Kawakami M, Nakayama J, Su L, et al. Enhanced Expression of Prostate-specific Membrane Antigen Gene in Prostate Cancer as Revealed by in Situ Hybridization.

- Cancer Res.* 1997;53:1441-1443.
125. Ruigrok EAM, van Weerden WM, Nonnekens J, de Jong M. The Future of PSMA-Targeted Radionuclide Therapy: An Overview of Recent Preclinical Research. *Pharmaceutics*. 2019;11(11):560. doi:10.3390/pharmaceutics11110560
  126. Lütje S, Slavik R, Fendler W, Herrmann K, Eiber M. PSMA ligands in prostate cancer – Probe optimization and theranostic applications. *Methods*. 2017;130:42-50. doi:10.1016/j.ymeth.2017.06.026
  127. Okarvi SM. Recent developments of prostate-specific membrane antigen (PSMA)-specific radiopharmaceuticals for precise imaging and therapy of prostate cancer: an overview. *Clin Transl Imaging*. 2019;7(3):189-208. doi:10.1007/s40336-019-00326-3
  128. Wüstemann T, Haberkorn U, Babich J, Mier W. Targeting prostate cancer: Prostate-specific membrane antigen based diagnosis and therapy. *Med Res Rev*. 2019;39(1):40-69. doi:10.1002/med.21508
  129. Haberkorn U, Eder M, Kopka K, Babich JW, Eisenhut M. New Strategies in Prostate Cancer: Prostate-Specific Membrane Antigen (PSMA) Ligands for Diagnosis and Therapy. *Clin Cancer Res*. 2016;22(1):9-15. doi:10.1158/1078-0432.CCR-15-0820
  130. BANDER N. Targeted systemic therapy of prostate cancer with a monoclonal antibody to prostate-specific membrane antigen. *Semin Oncol*. 2003;30(5):667-676. doi:10.1016/S0093-7754(03)00358-0
  131. Wolf P. Anti-PSMA Antibody-Drug Conjugates and Immunotoxins. In: *Antibody-Drug Conjugates and Immunotoxins*. Springer New York; 2013:255-272. doi:10.1007/978-1-4614-5456-4\_15
  132. Goldsmith SJ, Tagawa ST, Vallabhajosula S, Nikolopoulou A, Lipai I, Bander NH. Targeted Radionuclide Therapy of Prostate Cancer. In: *Therapeutic Nuclear Medicine*. Springer, Berlin, Heidelberg; 2013:617-628. doi:10.1007/174\_2012\_786
  133. Nakajima T, Mitsunaga M, Bander NH, Heston WD, Choyke PL, Kobayashi H. Targeted, Activatable, In Vivo Fluorescence Imaging of Prostate-Specific Membrane Antigen (PSMA) Positive Tumors Using the Quenched Humanized J591 Antibody–Indocyanine Green (ICG) Conjugate. *Bioconjug Chem*. 2011;22(8):1700-1705. doi:10.1021/bc2002715
  134. de Jong M, Valkema R, Jamar F, et al. Somatostatin receptor-targeted radionuclide therapy of tumors: Preclinical and clinical findings. *Semin Nucl Med*. 2002;32(2):133-140. doi:10.1053/snuc.2002.31027
  135. Bander NH, Milowsky MI, Nanus DM, Kostakoglu L, Vallabhajosula S, Goldsmith SJ. Phase I Trial of 177 Lutetium-Labeled J591, a Monoclonal Antibody to Prostate-Specific Membrane Antigen, in Patients With Androgen-Independent Prostate Cancer. *J Clin Oncol*. 2005;23(21):4591-4601. doi:10.1200/JCO.2005.05.160
  136. Basuli F, Phelps TE, Zhang X, et al. Fluorine-18 Labeled Urea-Based Ligands

- Targeting Prostate-Specific Membrane Antigen (PSMA) with Increased Tumor and Decreased Renal Uptake. *Pharmaceuticals*. 2022;15(5):597. doi:10.3390/ph15050597
137. Dietlein M, Kobe C, Kuhnert G, et al. Comparison of [18F]DCFPyL and [68Ga]Ga-PSMA-HBED-CC for PSMA-PET Imaging in Patients with Relapsed Prostate Cancer. *Mol Imaging Biol*. 2015;17(4):575-584. doi:10.1007/S11307-015-0866-0
  138. Chandran E, Figg WD, Madan R. Lutetium-177-PSMA-617: A Vision of the Future. *Cancer Biol Ther*. 2022;23(1):186-190. doi:10.1080/15384047.2022.2037985
  139. Sathekge M, Bruchertseifer F, Vorster M, et al. mCRPC patients receiving 225Ac-PSMA-617 therapy in post androgen deprivation therapy setting: Response to treatment and survival analysis. *J Nucl Med*. 2022;(2):jnumed.121.263618. doi:10.2967/JNUMED.121.263618
  140. Jilg CA, Reichel K, Stoykow C, et al. Results from extended lymphadenectomies with [111In]PSMA-617 for intraoperative detection of PSMA-PET/CT-positive nodal metastatic prostate cancer. *EJNMMI Res*. 2020;10(1):1-13. doi:10.1186/S13550-020-0598-2/TABLES/4
  141. Heinzl A, Boghos D, Mottaghy FM, et al. 68 Ga-PSMA PET/CT for monitoring response to 177 Lu-PSMA-617 radioligand therapy in patients with metastatic castration-resistant prostate cancer. *Eur J Nucl Med Mol Imaging*. 2019;46(5):1054-1062. doi:10.1007/S00259-019-4258-6/FIGURES/4
  142. Rathke H, Flechsig P, Mier W, et al. Dosimetry Estimate and Initial Clinical Experience with 90Y-PSMA-617. *J Nucl Med*. 2019;60(6):806-811. doi:10.2967/JNUMED.118.218917
  143. Alberts I, Sachpekidis C, Gourni E, et al. Dynamic patterns of [68Ga]Ga-PSMA-11 uptake in recurrent prostate cancer lesions. *Eur J Nucl Med Mol Imaging*. 2020;47(1):160-167. doi:10.1007/s00259-019-04545-8
  144. Rahbar K, Afshar-Oromieh A, Seifert R, et al. Diagnostic performance of 18F-PSMA-1007 PET/CT in patients with biochemical recurrent prostate cancer. *Eur J Nucl Med Mol Imaging*. 2018;45(12):2055-2061. doi:10.1007/S00259-018-4089-X
  145. Ferreira G, Iravani A, Hofman MS, Hicks RJ. Intra-individual comparison of 68Ga-PSMA-11 and 18F-DCFPyL normal-organ biodistribution. *Cancer Imaging*. 2019;19(1). doi:10.1186/S40644-019-0211-Y
  146. Szabo Z, Mena E, Rowe SP, et al. Initial Evaluation of [18F]DCFPyL for Prostate-Specific Membrane Antigen (PSMA)-Targeted PET Imaging of Prostate Cancer. *Mol Imaging Biol*. 2015;17(4):565-574. doi:10.1007/S11307-015-0850-8
  147. Chatachot K, Shiratori S, Chaiwatanarat T, Khamwan K. Patient dosimetry of 177Lu-PSMA I&T in metastatic prostate cancer treatment: the experience in Thailand. *Ann Nucl Med*. 2021;35(11):1193-1202. doi:10.1007/s12149-021-01659-8

148. Zacherl MJ, Gildehaus FJ, Mittlmeier L, et al. First Clinical Results for PSMA-Targeted  $\alpha$ -Therapy Using  $^{225}\text{Ac}$ -PSMA-I&T in Advanced-mCRPC Patients. *J Nucl Med*. 2021;62(5):669-674. doi:10.2967/JNUMED.120.251017
149. Schottelius M, Wirtz M, Eiber M, Maurer T, Wester HJ. [ $^{111}\text{In}$ ]PSMA-I&T: expanding the spectrum of PSMA-I&T applications towards SPECT and radioguided surgery. *EJNMMI Res*. 2015;5(1):1-5. doi:10.1186/S13550-015-0147-6
150. Frenzel T, Tienken M, Abel M, et al. The impact of [ $^{68}\text{Ga}$ ]PSMA I&T PET/CT on radiotherapy planning in patients with prostate cancer. *Strahlentherapie und Onkol*. 2018;194(7):646-654. doi:10.1007/S00066-018-1291-5
151. Zechmann CM, Afshar-Oromieh A, Armor T, et al. Radiation dosimetry and first therapy results with a  $^{124}\text{I}/^{131}\text{I}$ -labeled small molecule (MIP-1095) targeting PSMA for prostate cancer therapy. *Eur J Nucl Med Mol Imaging*. 2014;41(7):1280-1292. doi:10.1007/s00259-014-2713-y
152. Hillier SM, Kern AM, Maresca KP, et al. 23 I-MIP-1072, a Small-Molecule Inhibitor of Prostate-Specific Membrane Antigen, Is Effective at Monitoring Tumor Response to Taxane Therapy. *J Nucl Med*. 2011;52:1087-1093. doi:10.2967/jnumed.110.086751
153. Walker SM, Lim I, Lindenberg L, Mena E, Choyke PL, Turkbey B. Positron emission tomography (PET) radiotracers for prostate cancer imaging. *Abdom Radiol*. 2020;45(7):2165-2175. doi:10.1007/s00261-020-02427-4
154. Saga T, Nakamoto Y, Ishimori T, et al. Initial evaluation of PET/CT with  $^{18}\text{F}$ -FSU-880 targeting prostate-specific membrane antigen in prostate cancer patients. *Cancer Sci*. 2019;110(2):742-750. doi:10.1111/CAS.13911
155. Zlatopolskiy BD, Endepols H, Krapf P, et al. Discovery of  $^{18}\text{F}$ -JK-PSMA-7, a PET Probe for the Detection of Small PSMA-Positive Lesions. *J Nucl Med*. 2019;60(6):817-823. doi:10.2967/JNUMED.118.218495
156. Osborne J, Akhtar NH, Vallabhajosula S, et al. Tc-99m labeled small-molecule inhibitors of prostate-specific membrane antigen (PSMA): New molecular imaging probes to detect metastatic prostate adenocarcinoma (PC). *J Clin Oncol*. 2012;30(5\_suppl):173-173. doi:10.1200/JCO.2012.30.5\_SUPPL.173
157. Wester HJ, Schottelius M. PSMA-Targeted Radiopharmaceuticals for Imaging and Therapy. *Semin Nucl Med*. 2019;49(4):302-312. doi:10.1053/J.SEMNUCLMED.2019.02.008
158. Choy CJ, Ling X, Geruntho JJ, et al.  $^{177}\text{Lu}$ -Labeled Phosphoramidate-Based PSMA Inhibitors: The Effect of an Albumin Binder on Biodistribution and Therapeutic Efficacy in Prostate Tumor-Bearing Mice. *Theranostics*. 2017;7(7):1928. doi:10.7150/THNO.18719
159. Lütje S, Franssen GM, Herrmann K, et al. In Vitro and In Vivo Characterization of an  $^{18}\text{F}$ -AIF-Labeled PSMA Ligand for Imaging of PSMA-Expressing Xenografts. *J Nucl Med*. 2019;60(7):1017-1022. doi:10.2967/JNUMED.118.218941

160. Malaspina S, Oikonen V, Kuisma A, et al. Kinetic analysis and optimisation of <sup>18</sup>F-rhPSMA-7.3 PET imaging of prostate cancer. *Eur J Nucl Med Mol Imaging*. 2021;48(11):3723-3731. doi:10.1007/S00259-021-05346-8
161. Kelly JM, Amor-Coarasa A, Nikolopoulou A, et al. Dual-Target Binding Ligands with Modulated Pharmacokinetics for Endoradiotherapy of Prostate Cancer. *J Nucl Med*. 2017;58(9):1442-1449. doi:10.2967/JNUMED.116.188722
162. Vahidfar N, Fallahpoor M, Farzanehfar S, Divband G, Ahmadzadehfar H. Historical review of pharmacological development and dosimetry of PSMA-based theranostics for prostate cancer. *J Radioanal Nucl Chem*. 2019;322(2):237-248. doi:10.1007/S10967-019-06800-6
163. Ling X, Latoche JD, Choy CJ, et al. Preclinical Dosimetry, Imaging, and Targeted Radionuclide Therapy Studies of Lu-177-Labeled Albumin-Binding, PSMA-Targeted CTT1403. *Mol Imaging Biol*. 2020;22(2):274-284. doi:10.1007/S11307-019-01404-8
164. Sterzing F, Kratochwil C, Fiedler H, et al. <sup>68</sup>Ga-PSMA-11 PET/CT: a new technique with high potential for the radiotherapeutic management of prostate cancer patients. *Eur J Nucl Med Mol Imaging*. 2016;43(1):34-41. doi:10.1007/S00259-015-3188-1
165. FDA Approves First PSMA-Targeted PET Imaging Drug for Men with Prostate Cancer | FDA. Accessed April 16, 2022. <https://www.fda.gov/news-events/press-announcements/fda-approves-first-psma-targeted-pet-imaging-drug-men-prostate-cancer>
166. Afshar-Oromieh A, Haberkorn U, Eder M, Martin Zechmann C. Prostate Cancer Imaging using PSMA ligands View project Local recurrence of prostate cancer detected by PSMA-PET/CT View project. *Eur J Nucl Med Mol Imaging*. 2012;39(6):1085-1086. doi:10.1007/s00259-012-2069-0
167. Sartor AO, Morris MJ, Messman R, Krause BJ. VISION: An international, prospective, open-label, multicenter, randomized phase III study of <sup>177</sup>Lu-PSMA-617 in the treatment of patients with progressive PSMA-positive metastatic castration-resistant prostate cancer (mCRPC). *J Clin Oncol*. 2020;38(6\_suppl):TPS259-TPS259. doi:10.1200/JCO.2020.38.6\_SUPPL.TPS259
168. Chatal JF, Hoefnagel CA. Radionuclide therapy. *Lancet*. 1999;354(9182):931-935. doi:10.1016/S0140-6736(99)06002-X
169. Thompson S, Kilbourn MR, Scott PJH. Radiochemistry, PET Imaging, and the Internet of Chemical Things. *ACS Cent Sci*. 2016;2(8):497-505. doi:10.1021/acscentsci.6b00178
170. Zimmermann RG. Industrial Constraints in the Selection of Radionuclides and the Development of New Radiopharmaceuticals. *World J Nucl Med*. 2008;7(2):126-136.
171. Hofman MS, Violet J, Hicks RJ, et al. [<sup>177</sup>Lu]-PSMA-617 radionuclide treatment in patients with metastatic castration-resistant prostate cancer (LuPSMA trial): a single-centre, single-arm, phase 2 study. *Lancet Oncol*. 2018;19(6):825-

833. doi:10.1016/S1470-2045(18)30198-0
172. Irvani A, Violet J, Azad A, Hofman MS. Lutetium-177 prostate-specific membrane antigen (PSMA) theranostics: practical nuances and intricacies. *Prostate Cancer Prostatic Dis.* 2020;23(1):38-52. doi:10.1038/s41391-019-0174-x
  173. Emmett L, Willowson K, Violet J, Shin J, Blanksby A, Lee J. Lutetium 177 PSMA radionuclide therapy for men with prostate cancer: a review of the current literature and discussion of practical aspects of therapy. *J Med Radiat Sci.* 2017;64(1):52-60. doi:10.1002/jmrs.227
  174. Gallyamov M, Meyrick D, Barley J, Lenzo N. Renal outcomes of radioligand therapy: experience of 177lutetium—prostate-specific membrane antigen ligand therapy in metastatic castrate-resistant prostate cancer. *Clin Kidney J.* 2020;13(6):1049-1055. doi:10.1093/CKJ/SFZ101
  175. Violet J, Jackson P, Ferdinandus J, et al. Dosimetry of 177Lu-PSMA-617 in Metastatic Castration-Resistant Prostate Cancer: Correlations Between Pretherapeutic Imaging and Whole-Body Tumor Dosimetry with Treatment Outcomes. *J Nucl Med.* 2019;60(4):517-523. doi:10.2967/JNUMED.118.219352
  176. Emmett L, Willowson K, Violet J, Shin J, Blanksby A, Lee J. Lutetium 177 PSMA radionuclide therapy for men with prostate cancer: a review of the current literature and discussion of practical aspects of therapy. *J Med Radiat Sci.* 2017;64(1):52-60. doi:10.1002/JMRS.227
  177. Williams LE, DeNardo GL, Meredith RF. Targeted radionuclide therapy. *Med Phys.* 2008;35(7Part1):3062-3068. doi:10.1118/1.2938520
  178. Pouget JP, Lozza C, Deshayes E, Boudousq V, Navarro-Teulon I. Introduction to Radiobiology of Targeted Radionuclide Therapy. *Front Med.* 2015;2(MAR):12. doi:10.3389/fmed.2015.00012
  179. Paganelli G, Sarnelli A, Severi S, et al. Dosimetry and safety of 177Lu PSMA-617 along with polyglutamate parotid gland protector: preliminary results in metastatic castration-resistant prostate cancer patients. *Eur J Nucl Med Mol Imaging.* 2020;47(13):3008-3017. doi:10.1007/s00259-020-04856-1
  180. Kratochwil C, Fendler WP, Eiber M, et al. EANM procedure guidelines for radionuclide therapy with 177Lu-labelled PSMA-ligands (177Lu-PSMA-RLT). *Eur J Nucl Med Mol Imaging.* 2019;46(12):2536-2544. doi:10.1007/s00259-019-04485-3
  181. Gupta A, Lee MS, Kim JH, Lee DS, Lee JS. Preclinical Voxel-Based Dosimetry in Theranostics: a Review. *Nucl Med Mol Imaging (2010).* 2020;54(2):86-97. doi:10.1007/S13139-020-00640-Z
  182. Gill MR, Falzone N, Du Y, Vallis KA. Targeted radionuclide therapy in combined-modality regimens. *Lancet Oncol.* 2017;18(7):e414-e423. doi:10.1016/S1470-2045(17)30379-0
  183. Wessels BW, Konijnenberg MW, Dale RG, et al. MIRD Pamphlet No. 20: The Effect of Model Assumptions on Kidney Dosimetry and Response—Implications

- for Radionuclide Therapy. *J Nucl Med.* 2008;49(11):1884-1899.  
doi:10.2967/jnumed.108.053173
184. Kratochwil C, Giesel FL, Stefanova M, et al. PSMA-Targeted Radionuclide Therapy of Metastatic Castration-Resistant Prostate Cancer with <sup>177</sup>Lu-Labeled PSMA-617. *J Nucl Med.* 2016;57(8):1170-1176.  
doi:10.2967/JNUMED.115.171397
  185. Filippi L, Chiaravalloti A, Schillaci O, Cianni R, Bagni O. Theranostic approaches in nuclear medicine: current status and future prospects. *Expert Rev Med Devices.* 2020;17(4):331-343. doi:10.1080/17434440.2020.1741348
  186. Rahmim A, Zaidi H. Pet versus spect: Strengths, limitations and challenges. *Nucl Med Commun.* 2008;29(3):193-207. doi:10.1097/MNM.0B013E3282F3A515
  187. Parodi K. Vision 20/20: Positron emission tomography in radiation therapy planning, delivery, and monitoring. *Med Phys.* 2015;42(12):7153-7168.  
doi:10.1118/1.4935869
  188. Lawhn-Heath C, Hope TA, Martinez J, et al. Dosimetry in radionuclide therapy: the clinical role of measuring radiation dose. *Lancet Oncol.* 2022;23(2):e75-e87.  
doi:10.1016/S1470-2045(21)00657-4
  189. Seuntjens J, Strydom W, A KS. *Dosimetric Principles, Quantities and Units. Radiation Oncology Physics: A Handbook for Teachers and Students. Podgorsak EB,.; 2005.*
  190. Fisher DR, Fahey FH. Appropriate Use of Effective Dose in Radiation Protection and Risk Assessment. *Health Phys.* 2017;113(2):102-109.  
doi:10.1097/HP.0000000000000674
  191. Stabin M. Nuclear medicine dosimetry. *Phys Med Biol.* 2006;51(13):R187-R202.  
doi:10.1088/0031-9155/51/13/R12
  192. Capala J, Graves SA, Scott A, et al. Dosimetry for Radiopharmaceutical Therapy: Current Practices and Commercial Resources. *J Nucl Med.* 2021;62(Supplement 3):3S-11S. doi:10.2967/jnumed.121.262749
  193. Grimes J, Celler A. Comparison of internal dose estimates obtained using organ-level, voxel S value, and Monte Carlo techniques. *Med Phys.* 2014;41(9):092501.  
doi:10.1118/1.4892606
  194. Gupta A, Lee MS, Kim JH, et al. Preclinical voxel-based dosimetry through GATE Monte Carlo simulation using PET/CT imaging of mice. *Phys Med Biol.* 2019;64(9):095007. doi:10.1088/1361-6560/ab134b
  195. Divoli A, Chiavassa S, Ferrer L, Barbet J, Flux GD, Bardiès M. Effect of Patient Morphology on Dosimetric Calculations for Internal Irradiation as Assessed by Comparisons of Monte Carlo Versus Conventional Methodologies. *J Nucl Med.* 2009;50(2):316-323. doi:10.2967/jnumed.108.056705
  196. Bolch WE, Bouchet LG, Robertson JS, et al. MIRD pamphlet no. 17: the dosimetry of nonuniform activity distributions—radionuclide S values at the voxel level. *J Nucl Med.* 1999;40:118-368.



197. Howell RW, Wessels BW, Loevinger R, et al. The MIRD Perspective 1999. *J Nucl Med.* 1999;40(1):3S-10S.
198. Akhavanallaf A, Shiri I, Arabi H, Zaidi H. Whole-body voxel-based internal dosimetry using deep learning. *Eur J Nucl Med Mol Imaging.* 2021;48(3):670-682. doi:10.1007/s00259-020-05013-4
199. Watanabe S, Shiga T, Hirata K, et al. Biodistribution and radiation dosimetry of the novel hypoxia PET probe [18F]DiFA and comparison with [18F]FMISO. *EJNMMI Res.* 2019;9(1). doi:10.1186/S13550-019-0525-6
200. Herrmann K, Rahbar K, Eiber M, et al. Dosimetry of <sup>177</sup>Lu-PSMA-617 for the treatment of metastatic castration-resistant prostate cancer: results from the VISION trial sub-study. *J Clin Oncol.* 2022;40(6\_suppl):97-97. doi:10.1200/JCO.2022.40.6\_SUPPL.097
201. McParland BJ, Wall A, Johansson S, Sørensen J. The clinical safety, biodistribution and internal radiation dosimetry of [18F]fluciclovine in healthy adult volunteers. *Eur J Nucl Med Mol Imaging.* 2013;40(8):1256-1264. doi:10.1007/S00259-013-2403-1
202. Carter LM, Crawford TM, Sato T, et al. PARaDIM: A PHITS-Based Monte Carlo Tool for Internal Dosimetry with Tetrahedral Mesh Computational Phantoms. *J Nucl Med.* 2019;60(12):1802-1811. doi:10.2967/jnumed.119.229013
203. Santoro L, Pitalot L, Trauchessec D, et al. Clinical implementation of PLANET® Dose for dosimetric assessment after [177Lu]Lu-DOTA-TATE: comparison with Dosimetry Toolkit® and OLINDA/EXM® V1.0. *EJNMMI Res.* 2021;11(1):1. doi:10.1186/s13550-020-00737-8
204. Lee MS, Kim JH, Paeng JC, et al. Whole-Body Voxel-Based Personalized Dosimetry: The Multiple Voxel S-Value Approach for Heterogeneous Media with Nonuniform Activity Distributions. *J Nucl Med.* 2018;59(7):1133-1139. doi:10.2967/JNUMED.117.201095
205. Besemer AE, Yang YM, Grudzinski JJ, Hall LT, Bednarz BP. Development and Validation of RAPID: A Patient-Specific Monte Carlo Three-Dimensional Internal Dosimetry Platform. *Cancer Biother Radiopharm.* 2018;33(4):155-165. doi:10.1089/CBR.2018.2451
206. Zaidi H, Xu XG. Computational Anthropomorphic Models of the Human Anatomy: The Path to Realistic Monte Carlo Modeling in Radiological Sciences. *Annu Rev Biomed Eng.* 2007;9(1):471-500. doi:10.1146/annurev.bioeng.9.060906.151934
207. Sanders JC, Kuwert T, Hornegger J, Ritt P. Quantitative SPECT/CT Imaging of <sup>177</sup>Lu with In Vivo Validation in Patients Undergoing Peptide Receptor Radionuclide Therapy. *Mol Imaging Biol.* 2015;17(4):585-593. doi:10.1007/s11307-014-0806-4
208. Li T, Zhu L, Lu Z, Song N, Lin KH, Mok GSP. BIGDOSE: software for 3D personalized targeted radionuclide therapy dosimetry. *Quant Imaging Med Surg.* 2020;10(1):160-170. doi:10.21037/qims.2019.10.09

209. Sanchez-Garcia M, Gardin I, Lebtahi R, Dieudonné A. Implementation and validation of collapsed cone superposition for radiopharmaceutical dosimetry of photon emitters. *Phys Med Biol.* 2015;60(20):7861-7876. doi:10.1088/0031-9155/60/20/7861
210. Carlsson Tedgren Å, Plamondon M, Beaulieu L, et al. Validation of a dose-point kernel convolution technique for internal dosimetry. *Phys Med Biol.* 1995;40(3):365. doi:10.1088/0031-9155/40/3/003
211. Simpkin DJ, Mackie TR. EGS4 Monte Carlo determination of the beta dose kernel in water. *Med Phys.* 1990;17(2):179-186. doi:10.1118/1.596565
212. Wang R, Sloboda RS, Carlsson Tedgren Å, et al. Point kernels and superposition methods for scatter dose calculations in brachytherapy. *Phys Med Biol.* 2000;45(2):357. doi:10.1088/0031-9155/45/2/308
213. Hippeläinen E, Tenhunen M, Sohlberg A. Fast voxel-level dosimetry for <sup>177</sup>Lu labelled peptide treatments. *Phys Med Biol.* 2015;60(17):6685. doi:10.1088/0031-9155/60/17/6685
214. Voter AF. INTRODUCTION TO THE KINETIC MONTE CARLO METHOD. In: *Radiation Effects in Solids*. Springer Netherlands; 2007:1-23. doi:10.1007/978-1-4020-5295-8\_1
215. Uusijärvi H, Chouin N, Bernhardt P, Ferrer L, Bardiès M, Forssell-Aronsson E. Comparison of Electron Dose-Point Kernels in Water Generated by the Monte Carlo Codes, PENELOPE, GEANT4, MCNPX, and ETRAN. *Cancer Biother Radiopharm.* 2009;24(4):461-467. doi:10.1089/cbr.2008.0573
216. Champion C, Incerti S, Perrot Y, et al. Dose point kernels in liquid water: An intra-comparison between GEANT4-DNA and a variety of Monte Carlo codes. *Appl Radiat Isot.* 2014;83:137-141. doi:10.1016/J.APRADISO.2013.01.037
217. Jiang H, Paganetti H. Adaptation of GEANT4 to Monte Carlo dose calculations based on CT data. *Med Phys.* 2004;31(10):2811-2818. doi:10.1118/1.1796952
218. Yoriyaz H, Moralles M, De Tarso Dalledone Siqueira P, Da Costa Guimarães C, Belonsi Cintra F, Dos Santos A. Physical models, cross sections, and numerical approximations used in MCNP and GEANT4 Monte Carlo codes for photon and electron absorbed fraction calculation. *Med Phys.* 2009;36(11):5198-5213. doi:10.1118/1.3242304
219. Carrier JF, Archambault L, Beaulieu L, Roy R. Validation of GEANT4, an object-oriented Monte Carlo toolkit, for simulations in medical physics. *Med Phys.* 2004;31(3):484-492. doi:10.1118/1.1644532
220. Li W, Lin L, Bao L, Zhao L, Li G. Monte Carlo simulation of photon migration in multi-component media. *Opt Quantum Electron.* 2015;47(7):1919-1931. doi:10.1007/s11082-014-0058-1
221. Kawrakow I. Accurate condensed history Monte Carlo simulation of electron transport. I. EGSnrc, the new EGS4 version. *Med Phys.* 2000;27(3):485-498. doi:10.1118/1.598917

222. Wulff J, Zink K, Kawrakow I. Efficiency improvements for ion chamber calculations in high energy photon beams. *Med Phys*. 2008;35(4):1328-1336. doi:10.1118/1.2874554
223. Tsougos I, Loudos G, Georgoulas P, Theodorou K, Kappas C. Patient-specific internal radionuclide dosimetry. *Nucl Med Commun*. 2010;31(2):97-106. doi:10.1097/MNM.0B013E328330626F
224. Li T, Ao ECI, Lambert B, Brans B, Vandenberghe S, Mok GSP. Quantitative Imaging for Targeted Radionuclide Therapy Dosimetry - Technical Review. *Theranostics*. 2017;7(18):4551. doi:10.7150/THNO.19782
225. Fraass BA, Smathers J, Deye J. Summary and recommendations of a National Cancer Institute workshop on issues limiting the clinical use of Monte Carlo dose calculation algorithms for megavoltage external beam radiation therapy. *Med Phys*. 2003;30(12):3206-3216. doi:10.1118/1.1626990
226. Peter J, Tornai MP, Jaszczak RJ. Analytical versus voxelized phantom representation for Monte Carlo simulation in radiological imaging. *IEEE Trans Med Imaging*. 2000;19(5):556-564. doi:10.1109/42.870266
227. Siegel, Jeffrey A., Stephen R. Thomas, James B. Stubbs, Michael G. Stabin, Marguerite T. Hays, Kenneth F. Koral JSR et al. MIRD pamphlet no. 16: techniques for quantitative radiopharmaceutical biodistribution data acquisition and analysis for use in human radiation dose estimates. *J Nucl Med*. 1999;40(2):37S-61S.
228. Ferrando O, Chimenz A, Foppiano F, Ciarmiello A. SPECT/CT activity quantification in <sup>99m</sup>Tc-MAA acquisitions. *J Diagnostic Imaging Ther*. 2018;5(1):32-36. doi:10.17229/jdit.2018-0624-034
229. Nichols TE, Qi J, Leahy RM. Continuous Time Dynamic PET Imaging Using List Mode Data. In: *Biennial International Conference on Information Processing in Medical Imaging*. Vol 1613. Springer Verlag; 1999:98-111. doi:10.1007/3-540-48714-X\_8
230. Dewaraja YK, Wilderman SJ, Ljungberg M, Koral KF, Zasadny K, Kaminiski MS. Accurate Dosimetry in <sup>131</sup>I Radionuclide Therapy Using Patient-Specific, 3-Dimensional Methods for SPECT Reconstruction and Absorbed Dose Calculation. *J Nucl Med*. 2005;46(5).
231. Kost SD, Dewaraja YK, Abramson RG, Stabin MG. VIDA: A Voxel-Based Dosimetry Method for Targeted Radionuclide Therapy Using Geant4. *Cancer Biother Radiopharm*. 2015;30(1):16-26. doi:10.1089/CBR.2014.1713
232. Besemer AE, Yang YM, Grudzinski JJ, Hall LT, Bednarz BP. Development and Validation of RAPID: A Patient-Specific Monte Carlo Three-Dimensional Internal Dosimetry Platform. *Cancer Biother Radiopharm*. 2018;33(4):155-165. doi:10.1089/CBR.2018.2451
233. Martinov MP, Opara C, Thomson RM, Lee TY. Fast beta-emitter Monte Carlo simulations and full patient dose calculations of targeted radionuclide therapy: introducing egs\_mird. *Med Phys*. Published online July 15, 2022.

doi:10.1002/mp.15786

234. Thomson RM, Taylor REP, Chamberland MJP, Rogers DWO. User Manual for egs\_brachy. *clrp-code.github.io*. [https://clrp-code.github.io/egs\\_brachy/pdf/egs\\_brachy\\_user\\_manual.pdf](https://clrp-code.github.io/egs_brachy/pdf/egs_brachy_user_manual.pdf)
235. Chamberland MJP, Taylor REP, Rogers DWO, Thomson RM. egs\_brachy: a versatile and fast Monte Carlo code for brachytherapy. *Phys Med Biol*. 2016;61(23):8214. doi:10.1088/0031-9155/61/23/8214
236. Pacilio M, Lanconelli N, Lo Meo S, et al. Differences among Monte Carlo codes in the calculations of voxel values for radionuclide targeted therapy and analysis of their impact on absorbed dose evaluations. *Med Phys*. 2009;36(5):1543-1552. doi:10.1118/1.3103401
237. Cristy M, Eckerman K. Specific absorbed fractions of energy at various ages from internal photon sources. *Oak Ridge Natl Lab, TN*. 1987;Report No.(ORNL/TM-8381):V1-V7.
238. Chibani O, Li XA. Monte Carlo dose calculations in homogeneous media and at interfaces: A comparison between GEPTS, EGSnrc, MCNP, and measurements. *Med Phys*. 2002;29(5):835-847. doi:10.1118/1.1473134
239. Poon E, Verhaegen F. Accuracy of the photon and electron physics in GEANT4 for radiotherapy applications. *Med Phys*. 2005;32(6Part1):1696-1711. doi:10.1118/1.1895796
240. Jabbari N, Hashemi-Malayeri B, Farajollahi AR, Kazemnejad A, Shafaei A, Jabbari S. Comparison of MCNP4C and EGSnrc Monte Carlo codes in depth-dose calculation of low energy clinical electron beams. *J Phys D Appl Phys*. 2007;40(15):4519. doi:10.1088/0022-3727/40/15/023
241. Wang R, Li XA. Monte Carlo dose calculations of beta-emitting sources for intravascular brachytherapy: A comparison between EGS4, EGSnrc, and MCNP. *Med Phys*. 2001;28(2):134-141. doi:10.1118/1.1339880
242. Miksys N, Vigneault E, Martin AG, Beaulieu L, Thomson RM. Large-scale Retrospective Monte Carlo Dosimetric Study for Permanent Implant Prostate Brachytherapy. *Int J Radiat Oncol*. 2017;97(3):606-615. doi:10.1016/J.IJROBP.2016.11.025
243. Vigneault E, Mbodji K, Carignan D, et al. The association of intraprostatic calcifications and dosimetry parameters with biochemical control after permanent prostate implant. *Brachytherapy*. 2019;18(6):787-792. doi:10.1016/J.BRACHY.2019.06.007
244. Scott J. Photon, Electron, Proton and Neutron Interaction Data for Body Tissues: ICRU Report 46. International Commission on Radiation Units and Measurements. Published online 1993.
245. Schneider W, Bortfeld T, Schlegel W. Influence of tissue composition on the results of Monte Carlo simulations for patient dose calculations. *Use Comput Radiat Ther*. Published online 2000:443-445. doi:10.1007/978-3-642-59758-9\_167

246. Rivard MJ, Coursey BM, Dewerd LA, et al. Update of AAPM Task Group No. 43 Report: A revised AAPM protocol for brachytherapy dose calculations. *Wiley Online Libr.* 2004;31(3):633-674. doi:10.1118/1.1646040
247. Akhavanallaf A, Mohammadi R, Shiri I, Salimi Y, Arabi H, Zaidi H. Personalized brachytherapy dose reconstruction using deep learning. *Comput Biol Med.* 2021;136:104755. doi:10.1016/J.COMPBIOMED.2021.104755
248. Chen JZ. Convolution and Superposition Methods. In: *Introduction to Megavoltage X-Ray Dose Computation Algorithms*. CRC Press; 2019:155-220. doi:10.1201/b22208-4
249. Baechler S, Hobbs RF, Prideaux AR, Wahl RL, Sgouros G. Extension of the biological effective dose to the MIRD schema and possible implications in radionuclide therapy dosimetry. *Med Phys.* 2008;35(3):1123-1134. doi:10.1118/1.2836421
250. Dale R, Carabe-Fernandez A. The radiobiology of conventional radiotherapy and its application to radionuclide therapy. *Cancer Biother Radiopharm.* 2005;20(1):47-51. doi:10.1089/CBR.2005.20.47
251. St. James S, Bednarz B, Benedict S, et al. Current Status of Radiopharmaceutical Therapy. *Int J Radiat Oncol.* 2021;109(4):891-901. doi:10.1016/J.IJROBP.2020.08.035
252. Huizing DMV, de Wit-van der Veen BJ, Verheij M, Stokkel MPM. Dosimetry methods and clinical applications in peptide receptor radionuclide therapy for neuroendocrine tumours: a literature review. *EJNMMI Res.* 2018;8(1):1-11. doi:10.1186/S13550-018-0443-Z
253. Chiesa C, Maccauro M, Romito R, et al. Need, feasibility and convenience of dosimetric treatment planning in liver selective internal radiation therapy with 90Y microspheres: the experience of the National Tumor Institute of Milan. *Q J NUCL MED MOL IMAGING.* 2011;55(2):168-197.
254. Wessels BW, Konijnenberg MW, Dale RG, et al. MIRD Pamphlet No. 20: The Effect of Model Assumptions on Kidney Dosimetry and Response—Implications for Radionuclide Therapy. *J Nucl Med.* 2008;49(11):1884-1899. doi:10.2967/JNUMED.108.053173
255. Herrmann K, Lapa C, Wester HJ, et al. Biodistribution and radiation dosimetry for the chemokine receptor CXCR4-targeting probe 68Ga-pentixafor. *J Nucl Med.* 2015;56(3):410-416.

# Appendices

## Appendix A: Copyright Agreement

### Copyright agreement for Chapter 1

SPRINGER NATURE LICENSE  
TERMS AND CONDITIONS

Aug 17, 2022

---

This Agreement between Mr. Chidera Opara ("You") and Springer Nature ("Springer Nature") consists of your license details and the terms and conditions provided by Springer Nature and Copyright Clearance Center.

License Number	5371150011737
License date	Aug 17, 2022
Licensed Content Publisher	Springer Nature
Licensed Content Publication	Modern Pathology
Licensed Content Title	Gleason grading and prognostic factors in carcinoma of the prostate
Licensed Content Author	Peter A Humphrey
Licensed Content Date	Feb 13, 2004
Type of Use	Thesis/Dissertation
Requestor type	academic/university or research institute
Format	electronic
Portion	figures/tables/illustrations
Number of figures/tables/illustrations	1

High-res required	no
Will you be translating?	no
Circulation/distribution	1 - 29
Author of this Springer Nature content	no
Title	Three-dimensional Voxel-level Dose Point Kernel Convolution Code
Institution name	University of Western Ontario
Expected presentation date	Aug 2022
Portions	Figure 1 Gleason grades: standard drawing.
Requestor Location	Mr. Chidera Opara Robarts Research Institute Western University 1151 Richmond St N Rm 1200D Attn Chidera Opara  London, ON N6A 5B7 Canada Attn: Mr. Chidera Opara
Total	0.00 CAD

## Copyright agreement for Chapter 3 and 4



Order Number: 1243874

Order Date: 16 Aug 2022

## Order Details

## 1. Medical physics

Billing Status:

Open

Article: Fast beta-emitter Monte Carlo simulations and full patient dose calculations of targeted radionuclide therapy: introducing egs\_mird

Order License ID	1243874-1	Type of use	Republish in a thesis/dissertation
Order detail status	Completed	Publisher	American Association of Physicists in Medicine [by the American Institute of Physics]
ISSN	2473-4209	Portion	Chapter/article
			0.00 CAD
			Republication Permission

## LICENSED CONTENT

Publication Title	Medical physics	Country	United States of America
Article Title	Fast beta-emitter Monte Carlo simulations and full patient dose calculations of targeted radionuclide therapy: introducing egs_mird	Rightsholder	John Wiley & Sons - Books
		Publication Type	Journal
		URL	<a href="http://scitation.aip.org/content/aapm/journal/medphys">http://scitation.aip.org/content/aapm/journal/medphys</a>



**Author/Editor** American Institute of Physics., American Association of Physicists in Medicine.

**Date** 01/01/1974

**Language** English

## REQUEST DETAILS

<b>Portion Type</b>	Chapter/article	<b>Rights Requested</b>	Main product and any product related to main product
<b>Page range(s)</b>	1-23		
<b>Total number of pages</b>	23	<b>Distribution</b>	Worldwide
<b>Format (select all that apply)</b>	Electronic	<b>Translation</b>	Original language of publication
<b>Who will republish the content?</b>	Academic institution	<b>Copies for the disabled?</b>	No
<b>Duration of Use</b>	Life of current edition	<b>Minor editing privileges?</b>	No
<b>Lifetime Unit Quantity</b>	Up to 499	<b>Incidental promotional use?</b>	No
		<b>Currency</b>	CAD

## NEW WORK DETAILS

<b>Title</b>	Fast beta-emitter Monte Carlo simulations and full patient dose calculations of targeted radionuclide therapy: introducing egs_mird	<b>Institution name</b>	University of Western Ontario
		<b>Expected presentation date</b>	2022-08-31
<b>Instructor name</b>	Ting-Yim Lee, Martin P Martinov, Rowan M Thomson et al		

## ADDITIONAL DETAILS

**The requesting person / organization to appear on the license** Chidera Opara

## REUSE CONTENT DETAILS

<b>Title, description or numeric reference of the portion(s)</b>	Full	<b>Title of the article/chapter the portion is from</b>	Fast beta-emitter Monte Carlo simulations and full patient dose calculations of targeted radionuclide therapy: introducing egs_mird
<b>Editor of portion(s)</b>	Martinov, Martin P.; Opara, Chidera; Thomson, Rowan M.; Lee, Ting-Yim		
<b>Volume of serial or monograph</b>	N/A		

## Appendix B: Dose Point Kernel Input File

```

#-----
:start run control:
  ncase = 3e9
  nbatch = 1
  calculation = First
:stop run control:
#-----
:start media definition:

  # All Transport
  AE = 00.512
  UE = 01.511
  AP = 00.001
  UP = 01.000

  material data file = EGSnrc/egs_home/egs_mird/material.dat
:stop media definition:

#-----
#####
# Phantom definition
#####
:start geometry definition:

: Start geometry:
  library = egs_ndgeometry
  type = EGS_XYZGeometry
  Name = Phantom
  x-planes = -0.45 -0.35 -0.25 -0.15 -0.05 0.05 0.15 0.25 0.35 0.45 # Should be changed
  y-planes = -0.45 -0.35 -0.25 -0.15 -0.05 0.05 0.15 0.25 0.35 0.45 # Should be changed
  z-planes = -0.45 -0.35 -0.25 -0.15 -0.05 0.05 0.15 0.25 0.35 0.45 # Should be changed

  :start media input:
    media = Prostate
  :stop media input:
:stop geometry:
  simulation geometry = Phantom
:stop geometry definition:

#-----
#####
# source definition
#####
:start source definition:
: Start Source:
  library = egs_internal_source
  Name = the_source_1
  geometry = Phantom
  charge = 0
  regions = 364 #should be changed depending on the Phantom configuration
  weights = 1
: Start spectrum:
  type = monoenergetic
  energy = 1.0
:stop spectrum:
:stop source:
: Start Source:
  Name = the_source
  library = egs_radionuclide_source
  base Source = the_source_1
: Start spectrum:
  type = radionuclide
  nuclide = Lu - 177
:stop spectrum:
:stop source:

```

```

simulation Source = the_source
:stop source definition:
#-----
#####
# Scoring options
#####

:start scoring options:
  type          = 3ddose
  file name     = FileName.3ddose

  scoring geometry = Phantom
:stop scoring options:

:start rng definition:
  type          = ranmar
  initial seeds = 28 29
  high resolution = yes
:stop rng definition:

:start MC transport parameter:
  Global ECUT          = 0.512
  Global PCUT          = 0.001
  Global SMAX          = 1e10
  Bound Compton Scattering = On
  Rayleigh Scattering  = On
  Atomic Relaxations   = On
  Photoelectron Angular Sampling = On
  Electron Impact Ionization = On
  Brems Angular Sampling = KM
  Brems Cross Sections = nist
  Pair Angular Sampling = Off
  ESTEPE               = 0.25
  XIMAX                = 0.5
  Skin Depth for BCA   = 3.0
  Boundary Crossing Algorithm = EXACT
  Electron-Step Algorithm = PRESTA-II
  Spin Effects         = On
  Radiative Compton Corrections = Off
  Photon Cross Sections = xcom
  Fluorescent Photon Cutoff = 0.001
:stop MC transport parameter:

```

## Appendix C: egs\_mird Input File for Patient simulation

```

#-----
:start run control:
  ncase      = 1e9
  nbatch     = 1
  nchunk     = 1
:stop run control:
#-----
:start media definition:

  AE = 00.512
  UE = 01.511
  AP = 00.001
  UP = 01.000

  material data file = /EGSnrc/egs_home/egs_mird/material.dat
:stop media definition:
#-----
:start geometry definition:
  :start geometry:
  library      = egs_glib
  type        = egsphant

```

```

        name          = phantom
    egsphant file = /EGSnrc/egs_home/egs_mird/FileName.egsphant
    density file = /EGSnrc/egs_home/egs_mird/material.dat
    :stop geometry:

        simulation geometry = phantom
    :stop geometry definition:
#-----
    :start source definition:
        :start source:
            library      = egs_internal_source
            name         = the_source_location
            geometry     = phantom
            activity file = /EGSnrc/egs_home/egs_mird/ActivityFileName.txt
            charge       = 0 # Input is ignored
        :start spectrum:
            type         = monoenergetic # Input is ignored
            energy       = 1.0 # Input is ignored
        :stop spectrum:
    :stop source:

        :start source:
            name         = the_source
            library      = egs_radionuclide_source
            base source = the_source_location
        :start spectrum:
            type         = radionuclide
            nuclide     = Lu-177
        :stop spectrum:
    :stop source:

        simulation source = the_source
    :stop source definition:
#-----
    :start scoring options:
        type           = 3ddose
        scoring geometry = phantom
        file name      = FileName.3ddose
    :stop scoring options:
#-----
    :start variance reduction:
        score tracklength dose = no
        muen file              = /EGSnrc/egs_home/egs_mird/XCOM_muen_1500keV.muendat
    :stop variance reduction:
#-----
    :start rng definition:
        type           = ranmar
        initial seeds  = 28 29
        high resolution = yes
    :stop rng definition:
#-----
    :start MC transport parameter:
        Global ECUT          = 0.512
        Global PCUT          = 0.001
        Global SMAX          = 1e10
        Bound Compton Scattering = On
        Rayleigh Scattering   = On
        Atomic Relaxations    = On
        Photoelectron Angular Sampling = On
        Electron Impact Ionization = On
        Brems Angular Sampling = KM
        Brems Cross Sections  = nist
        Pair Angular Sampling = Off
        ESTEPE                = 0.25
        XIMAX                 = 0.5
        Skin Depth for BCA    = 3.0
        Boundary Crossing Algorithm = EXACT
        Electron-Step Algorithm = PRESTA-II
        Spin Effects         = On

```

```
Radiative Compton Corrections = Off
Photon Cross Sections         = xcom
Fluorescent Photon Cutoff     = 0.001
:stop MC transport parameter:
#-----
```

## Curriculum Vitae

**Name:** Chidera Opara

**Post-secondary Education and Degrees:** SRM University  
Chennai, India  
2012-2015. B.Sc. Physics

Universidad de Sevilla  
Seville, Spain  
2017-2019 M.Sc. Nuclear Physics

The University of Western Ontario  
London, Ontario, Canada  
2020-2022 M.Sc. Medical Biophysics

### **Publications:**

Martinov MP, **Opara C**, Thomson RM, Lee T-Y. Fast beta-emitter Monte Carlo simulations and full patient dose calculations of targeted radionuclide therapy: introducing egs\_mird. Med Phys. Published online July 15, 2022. doi:10.1002/MP.15786

### **Conferences and Abstracts:**

Accepted Abstract at LHRD - 2021

Title: A Fast Voxel-based 3-D Dose Convolution Method for Personalized Targeted Radionuclide Therapy of Prostate Cancer Patients

London Health Research Day in partnership by Lawson Health Research Institute and the Schulich School of Medicine Dentistry, University of Western Ontario, London, Canada. May 7th - 11th, 2021.

Platform presentation at LHRD - 2021

Title: A Fast Voxel-based 3-D Dose Convolution Method for Personalized Targeted Radionuclide Therapy of Prostate Cancer Patients

London Health Research Day (LHRD - 2021) in partnership by Lawson Health Research Institute and the Schulich School of Medicine Dentistry, University of Western Ontario, London, Canada. May 7th - 11th, 2021.

Accepted Abstract and Platform Presentation at SIF - 2019

Analytical and Monte Carlo Approaches for the radiobiological in vitro Study of Radioresistant Breast Adenocarcinoma (MDA-MB-231) Cancer Cell Line with Clinical Proton Beam.

Authors: G. Petringa , **O. Chidera**, F.P. Cammarata, G. Colelli, G. Cuttone, G. Forte, R. Khanna, L. Minafra, G. Russo and G.A.P. Cirrone

Presented on 27th September, 2019 at Societ`a Italiana di Fisica (SIF) conference, Italy